ELECTRON-ANION EXCHANGE AS A NEW MECHANISM FOR NON-REDOX FLUORIDE-ION BATTERY ELECTRODES

Jacob T. Pawlik

A dissertation submitted to the faculty at the University of North Carolina at Chapel Hill in partial fulfillment of the requirements for the degree of Doctor of Philosophy in the Department of Chemistry.

Chapel Hill
2021

Approved by:

Scott C. Warren

Wei You

James F. Cahoon

Theo Dingemans

Yosuke Kanai

© 2021
Jacob Tyler Pawlik
ALL RIGHTS RESERVED

ABSTRACT

Jacob T. Pawlik: Electron-anion exchange as a new mechanism for non-redox fluoride-ion battery electrodes
(Under the direction of Scott C. Warren)

Typically, the insertion of ions into a crystalline material is accompanied by the oxidation or reduction of atoms in the host lattice. For example, when Li^+ ions enter a $LiCoO_2$ cathode during electrochemical discharge, the oxidation state of Co atoms changes from 4+ to 3+. However, I recently discovered a new insertion phenomenon where anion intercalation into materials called electrides does not perturb the oxidation states of the host atoms. Electrides are ionic materials in which electrons act as the negative charge balance instead of anions, and the "electride electrons" occupy lattice sites separate from atomic nuclei. The chemical nature of electrides allows for exchange of interlayer electrons with small anions, such as F^-, because of their similar size and charge, avoiding the need to oxidize or reduce the electride lattice. I identified an opportunity to use "electron-anion exchange" as a new mechanism for anion charge storage, where electrides offer high charge capacities (> 260 mAh/g) and large voltages (< 4 V) for fluoride-ion batteries. In this dissertation, I describe the suitability of electrides for high energy density fluoride-ion battery electrodes and give experimental evidence for the electron-anion exchange phenomenon. Additionally, I provide a brief history of electrides and fluoride-ion batteries with an explanation of how batteries work and common methods of electrochemical testing.

To my beautiful wife, family, and friends, who
make this life an incredible adventure.

ACKNOWLEDGEMENTS

I would like to thank each and every person that has helped me through graduate school and encouraged me along the way. I would not be where I am today if it wasn't for the love and support that has been so graciously bestowed upon me and the many blessings that God has brought into my life. I thank God every day for all of you.

To my research advisor, Scott Warren, who has trained me to be a scientist, leader, and mentor. Thank you for introducing me to the wonders of materials science and all the amazing things that can be accomplished through scientific research. Your passion for science and mentoring students has made a real impact on my life and the UNC community, and I am now inspired to carry the same passion into my future career.

To the Warren Lab, including Tyler, Adam, Kaci, Dan, Madeline, Jack, Lauren, Jessica, Zack, Matt, Connor, Becca, Duncan, Karen, thank you for challenging me, catching me when I fall, and picking me up when I am weary. I have become a better scientist and person because of each of you, and I will miss you all dearly.

To my wife, JoAnna, who graciously agreed that we move to Chapel Hill in the first place and has been a guiding light throughout my life. Thank you for being there for me in the hard times, the times of celebration, and the in-between. You have truly been a cornerstone to my journey through graduate school, providing me with the love and care I need to approach each day with a joyful heart. I am so excited about the next step in our careers, and all that the future holds for us.

To my family, which by unofficial adoption includes a large number of people, but is narrowed here to those that have impacted me in a very special way. To my parents and grandparents, I cannot express how grateful I am for you bringing foundation to my life and being present for all the important milestones of my journey. Through participating in Battle of the Books in elementary school, getting involved in science through Science Olympiad in high school, and finding my passion for chemistry at Appalachian State, I owe all of my growth as an individual to your unconditional love for me and your relentless dedication towards building a brighter future for me and my wife. To my brother, Jordan, my imagination would not be where it is today if it were not for all of the times we fought Ivan Ooze as Power Rangers in our house or geared up as Spy Kids, ready to take on the world. I love you all so very much.

To my other immediate family: Kim, Tommy, Todd, Krysta, I do not know where I would be today if I had not met you all those years ago in Boone, North Carolina. You have given me hope, encouragement, wonder, and a place to stay (thanks Kim and Tommy), and I cherish all of the memories we have made already and those yet to come. Thank you for being a solid rock in my life and caring for me so deeply.

Last but certainly not least, I thank my friends, who are too numerous to list here but deserve all the praise in the world for supporting me and providing much needed laughter in times of unrest. Thank you, Jake and Jon, for forming the Three Amigops and being lifelong friends. Thank you, Marcus and Travis, for partying like it's 1999 and walking through graduate school with me. Thank you, Monica, Megan, CJ, Ian, Sarah, Candice, for being my wife's friends and hosting really great board game nights. And thank you Chris, for randomly showing up and being a great friend.

TABLE OF CONTENTS

LIST OF TABLES……. xi

LIST OF FIGURES……..... xii

LIST OF ABBREVIATIONS……..……..... xiv

CHAPTER 1: INTRODUCTION…….….. 1

1.1 Motivation…….…….. 1

1.2 Fundamentals of Battery Electrochemistry……..… 3

1.2.1 Description of batteries…….…….. 3

1.2.2 Voltage, current, and charge capacity…….…… 5

1.2.3 Reference electrodes…….…….. 6

1.2.4 Electrode-electrolyte interface…….…... 8

1.2.5 Mechanisms of ion insertion……...….. 10

1.2.6 Potentiometry……...……. 11

1.3 A History of Fluoride-ion Batteries……...……... 13

1.3.1 Early works on fluoride-ion conductors and batteries……...….... 13

1.3.2 The first reversible fluoride-ion battery……...……. 17

1.3.3 Intercalation-based electrodes……...…… 21

1.3.4 Liquid electrolytes for fluoride-ion batteries……..…….. 23

1.4 A Brief History of Electrides……..…….. 26

REFERENCES……..…...… 30

CHAPTER 2: METHODS…….…….. 36

2.1 Computational Methods……...…. 36

2.1.1 Density-functional theory calculations……..…... 36

2.1.2 Calculation of battery electrode characteristics……..….. 38

2.2 Characterization methods……..……..... 41

2.2.1 Powder X-ray diffraction…….…… 41

2.2.2 Electron microscopy…….…..... 41

2.2.4 X-ray photoelectron spectroscopy…….……... 42

2.2.5 Ultraviolet-visible spectroscopy…….…….. 42

2.3 Synthesis of materials…….…….. 43

2.3.1 Custom arc-melting apparatus…….……...….. 43

2.3.2 Synthesis of layered and cubic Y_2C……..…… 45

2.3.3 Synthesis of Y_2CF_2……... 46

2.3.4 Y_2CF_2 + Na or K vapor reactions……. 47

2.3.5 Y_2CF_2 + Li reactions……. 47

2.4 Electrochemical methods…….. 48

2.4.1 Slurry preparation and casting…….. 48

2.4.2 Film casting and drying…… 48

2.4.3 Synthesis of the liquid fluoride-ion electrolyte…..…….…….. 49

2.4.4 Custom 3-electrode electrochemical coin cell…….. 49

2.4.5 Reference and counter electrodes……. 51

2.4.6 Electrochemical testing methods…….. 51

REFERENCES……. 53

CHAPTER 3: FIRST-PRINCIPLES PREDICTION OF ELECTROCHEMICAL ELECTRON-ANION EXCHANGE……..... 55

3.1 Introduction……..…. 55

3.2 Results……..…. 57

3.2.1 Density-functional theory calculations of EAX……..….. 57

3.2.2 Applications to batteries……...……..... 62

3.3 Conclusion……..... 64

REFERENCES…….…… 65

CHAPTER 4: SYNTHESIS AND ELECTRONIC STRUCTURE OF A 3D CRYSTALLINE STACK OF MXENE-LIKE SHEETS……...…….. 67

4.1 Introduction……..……. 67

4.2 Results……..……. 69

4.2.1 Synthesis and crystal structure……..…… 69

4.2.2 Composition and purity……...…….. 74

4.2.3 Electronic structure of Y_2CF_2……..……. 75

4.2.4 Sensitivity to oxygen……...…….. 78

4.3 Conclusion……..…….. 85

REFERENCES…….…… 86

CHAPTER 5: EXPERIMENTAL ELECTRON-ANION EXCHANGE: AN ION EXCHANGE MECHANISM FOR LOW-TEMPERATURE ELECTRIDE SYNTHESIS……..……... 91

5.1 Introduction……..……. 91

5.2 Thermodynamic predictions…….…… 93

5.3 Reaction between Y_2CF_2 and molten Li……..……. 93

5.4 Reaction between Y_2CF_2 and Na or K vapor……..…….…. 97

5.5 Conclusion……..……..…. 98

REFERENCES……..……... 99

CHAPTER 6: ELECTROCHEMICAL FLUORINATION OF ELECTRIDE Y_2C FOR ROOM-TEMPERATURE FLUORIDE-ION BATTERIES…….……. 103

6.1 Introduction…….…… 103

6.2 Results/Discussion…….……. 106

6.2.1 Fluoride-ion electrolyte characterization…….……... 106

6.2.2 Electrode preparation and characterization…….…… 109

6.2.3 Soaking films in the F-electrolyte…….…….. 115

6.2.4 Theoretical voltage profile…….……. 117

6.2.5 Electrochemistry on Y_2CF_2 films……..…….. 118

6.2.6 Electrochemistry on Y_2C films…….…….. 120

6.2.7 Electrochemical cycling of Y_2C films…….……... 123

6.3 Conclusions……..……... 124

REFERENCES…….…….. 126

LIST OF TABLES

Table 3.1: Oxidation states in Y_2C and Y_2CF_2…….…… 60

Table 3.2: Lattice constants and atomic distances in Y_2C and Y_2CF_2……..……. 63

Table 4.1: Final Parameters and R Factors for Y_2CF_2 at 300 K…….... 71

Table 4.2: Interatomic distances in the crystal structure of Y_2CF_2…….... 74

Table 4.3: XPS binding energy data from Y_2CF_2 samples…… 83

Table 6.1: Equivalent circuit fitting of EIS data……..…… 107

LIST OF FIGURES

Figure 1.1: Direction of ion movement in batteries…….. 4

Figure 1.2: Electric double layer structure for a negatively polarized anode surface……..... 8

Figure 1.3: Alignment of electrode Fermi levels with HOMO and LUMO of electrolyte…. 10

Figure 1.4: Theoretical voltage profile from galvanostatic measurements on a two-phase.... 12
electrochemical system

Figure 1.5: Historical progression of electrides…….. 27

Figure 2.1: Arc-melting setup for welding tantalum tubes…….. 44

Figure 2.2: Liquid electrochemical cell for fluoride-ion disk electrode testing…….…. 50

Figure 3.1: Concept of electron-anion exchange……. 56

Figure 3.2: Mechanism of electron−anion exchange…….. 58

Figure 3.3: Electron density in Y_2C with a single F atom …….…. 59

Figure 3.4: Polarization of valence electrons at and near the Fermi level…….. 61

Figure 3.5: Application of electron−anion exchange…….. 63

Figure 4.1: X-ray diffraction of Y_2CF_2…….…... 70

Figure 4.2: Crystal structure of Y_2CF_2……..... 72

Figure 4.3: Comparison of Y_2CF_2 and Y_2CCl_2 structure and binding energy……. 73

Figure 4.4: Optical properties of Y_2CF_2…….. 76

Figure 4.5: XPS of Y_2CF_2 samples…….… 80

Figure 4.6: Band positions of Y_2CF_2 on an absolute scale…….…. 84

Figure 5.1: Electron-anion exchange via chemical defluorination with alkali metal…….. 92
reducing agents (Li, Na, K)

Figure 5.2: Reaction between Y_2CF_2 and molten lithium……... 94

Figure 5.3: XAS on Y_2CF_2-Li products…….…. 96

Figure 5.4: X-ray diffraction pattern of the products from the Y_2CF_2 + K vapor reaction…. 97

Figure 6.1: Y_2C/Y_2CF_2 as high energy density fluoride-ion electrodes…… 104

Figure 6.2: Electrochemical impedance spectroscopy on the F-electrolyte…….. 107

Figure 6.3: Determination of the F-electrolyte electrochemical window……..…. 109

Figure 6.4: XRD of bulk Y_2C and Y_2CF_2……. 110

Figure 6.5: Preparation of electrode films for electrochemical testing……. 111

Figure 6.6: XRD of Y_2CF_2 and Y_2C films…… 113

Figure 6.7: TEM-EDS of a Y_2CF_2 film……. 114

Figure 6.8: Effect of film soaking in F-electrolyte on structure and composition…… 116

Figure 6.9: Expected voltage profile for Y_2C/Y_2CF_2 fluorination/defluorination…… 118

Figure 6.10: Electrochemistry on a Y_2CF_2 film…….. 119

Figure 6.11: Electrochemistry on a Y_2C film…….. 121

Figure 6.12: Elemental analysis of a Y_2C film after electrochemistry…… 122

Figure 6.13: Electrochemical cycling of a Y_2C film……... 124

LIST OF ABBREVIATIONS

ACET	Anion-coupled electron transfer
BTFE	Bis(trifluoroethyl)ether
CB	Conduction band
CP	Chronopotentiometry
CPE	Constant phase element
CV	Cyclic voltammetry
DFT	Density-functional theory
EAX	Electron-anion exchange
EDS	Energy-dispersive X-ray spectroscopy
EXAFS	Extended X-ray absorption fine structure
GS	Ground state
HOMO	Highest occupied molecular orbital
LST/QST	Linear synchronous transit/quadratic synchronous transit
LUMO	Lowest unoccupied molecular orbital
NEB	Nudged elastic band
Np_1F	N,N,N-trimethyl-N-neopentylammonium fluoride
OCV	Open circuit voltage
PCET	Proton-coupled electron transfer
PDOS	Projected density of states
PVDF	Poly(vinylidene) fluoride
SEI	Solid-electrolyte interphase
SEM	Scanning electron microscopy

SHE	Standard hydrogen electrode
TEM	Transmission electron microscopy
TS	Transition state
UV-Vis	Ultraviolet-visible spectroscopy
VB	Valence band
XANES	X-ray absorption near-edge structure
XAS	X-ray absorption spectroscopy
XPS	X-ray photoelectron spectroscopy
XRD	X-ray diffraction

CHAPTER 1: INTRODUCTION

1.1 Motivation

Scientists have known for decades that climate change is set to drastically impact the future of our planet, and the world is finally responding with targeted action. Over 190 states have signed the Paris Agreement with the goal of limiting global warming to < 2°C compared to pre-industrial levels, and many countries have pledged net-zero CO_2 emissions by as early as 2050. Currently, 80% of the world's energy consumption is sourced from burning petroleum, coal, and natural gas, contributing towards 65% of annual greenhouse gas emissions and 10 billion tons of CO_2 each year.[1] One way to cut out a significant portion of CO_2 emissions is to invest in electric vehicles, where 30% of annual CO_2 emissions comes from transportation alone. However, current batteries for electric vehicles are costly and have much lower energy densities than gasoline, complicating their economic and practical viability. Therefore, new technologies beyond lithium-ion batteries need to be discovered to enable a renewable energy future.

A number of next-generation batteries are currently being developed, including Na-ion, Mg-ion, and metal-air batteries, which could offer inexpensive alternatives to Li-ion with similar energy densities.[2,3] However, none have been able to match the performance of lithium-ion batteries given their low capacities and limited cycling. A promising approach is to consider batteries based on fluoride-ion shuttling, where F^- has a similar size to a Li^+ ion and formation of metal fluoride compounds is associated with large formation energies.[4] These factors translate to improved cycling due to improved ion diffusion, high capacities from the dense packing of fluoride in metal fluoride compounds, and large voltages from a strong electrochemical driving

force. Fluoride-ion batteries have been studied since 1976[5], but have largely been underdeveloped due to the low ionic conductivity of fluoride-ion electrolytes and large volume changes of conversion-based metal fluoride electrodes, translating to low capacities and cyclability. While intercalation-type electrodes have been developed that exhibit small volumes changes[6–8], their gravimetric capacities are low (< 30 mAh/g). Furthermore, the batteries often require high temperatures (> 150°C) to operate, non-ideal for practical application. Therefore, new electrode and electrolyte materials with better ionic conductivity, high charge capacities, and small volume changes need to be developed.

In a recent publication, we showed that an exotic class of materials called electrides might be useful as fluoride-ion battery electrodes and offer high capacities and cyclability.[9] Electrides are ionic materials where the counter-anion is simply an electron acting as an anion, occupying unique space within the material lattice separate from atomic nuclei.[10] We call these interlayer electrons "electride-electrons" and predict that the electrons will exchange with anions due to their similar size and charge. A new concept of "electron-anion exchange" is outlined that alters the perception on anion intercalation into materials, where the insertion of an anion into an electride does not involve the oxidation/reduction of atoms in the host lattice. Instead, we predict that electrons exchange with anions with little perturbation to atomic oxidation states. This new mechanism may translate to improved conduction of fluoride in electrides compared to other materials due to the charge compensation and repulsion provided by the interlayer electrons.

In this work, we describe a new class of materials for batteries, called electrides, that could fit the need for high performance fluoride-ion battery electrodes and offer a new redox-less mechanism for anion insertion, called electron-anion exchange. Furthermore, we demonstrate utilization of a recently discovered liquid fluoride-ion electrolyte[11] to conduct room-temperature

electrochemical cycling on our electride materials, displaying the first intercalation-based anode material for fluoride-ion batteries.

1.2 Fundamentals of Battery Electrochemistry

1.2.1 Description of batteries

Batteries utilize electrochemical reactions between a reducing agent at the anode and oxidizing agent at the cathode to produce energy. The transfer of electrons from anode to cathode produces current, which can be used to power electronics. Key to the function of a battery is the electrolyte, which separates the anode and cathode to provide electrochemical control. A gain or loss of electrons from either electrode must be compensated for by ion diffusion to the electrode surface. The electrolyte serves as a medium for ions to diffuse between electrodes and account for charge imbalances. For example, in lithium-ion batteries, Li^+ ions shuttle away from the anode and towards the cathode during discharging, following the direction of electron transfer. Conversely, during charging, Li^+ ions shuttle back to the anode. A common electrochemical reaction in lithium-ion batteries is shown below, where graphite is the anode and a metal oxide is the cathode:

$$Anode: \quad Li_xC \rightarrow xLi^+ + C + xe^-$$

$$Cathode: \quad Li_{1-x}CoO_2 + xLi^+ + xe^- \rightarrow LiCoO_2$$

$$Net\ equation: \quad Li_xC + Li_{1-x}CoO_2 \rightarrow C + LiCoO_2$$

In contrast, in fluoride-ion batteries, F^- ions shuttle from cathode to anode during electrochemical discharging since the charge is opposite to Li^+. Consequently, electrochemical charging involves F^- shuttling back to the cathode. A general expression for a fluoride-ion electrochemical reaction is shown below:

$$Anode: \quad M_A + xF^- \rightarrow M_AF_x + xe^-$$

$$Cathode: \quad M_C F_x + xe^- \rightarrow M_C + xF^-$$

$$Net\ equation: \quad M_A + M_C F_x \rightarrow M_A F_x + M_C$$

Aside from the differences in directionality, fluoride-ion batteries function in the same way as lithium-ion batteries. A graphical depiction of the differences between Li-ion and F-ion mechanisms is shown in Figure 1.1.

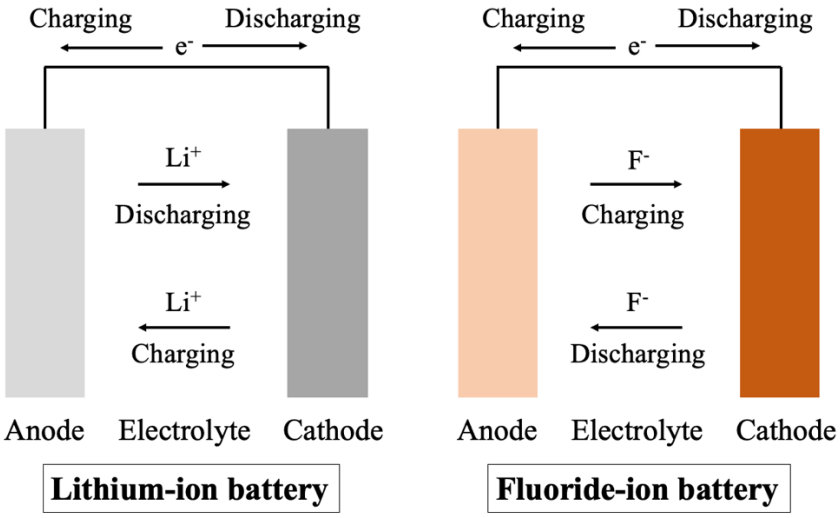


Figure 1.1: Direction of ion movement in batteries. A comparison of ion movement in cation-based (lithium-ion battery) and anion-based (fluoride-ion battery) during electrochemical charging and discharging.

The electrolyte is often a liquid or solid medium which contains a high concentration of the shuttling ion, where concentration is directly correlated to how quickly the ions can diffuse between electrodes. For example, a common liquid Li^+-based electrolyte for lithium-ion batteries is 1 M $LiPF_6$ in a mixture of ethylene carbonate and diethyl carbonate (EC/DEC). The rate of ion diffusion can be expressed as an ionic conductivity, defined as the inverse of the solution resistivity, or resistance of the solution to the flow of ionic current. Therefore, $\sigma = 1/\rho$ where σ is the conductivity ($\Omega^{-1}cm^{-1}$ or S/cm) and ρ is the resistivity ($\Omega \cdot cm$). The electrical conductivity, related to the diffusion rate of electrons, should therefore be negligible for electrolytes.

Otherwise, the anode and cathode would short-circuit. The conductivity is an intrinsic property that is independent of the electrolyte volume, where the resistance across a given distance can be calculated from the resistivity.

1.2.2 Voltage, current, and charge capacity

The chemical energy of a battery can be determined by calculating the change in free energy between the reactants and products, ΔG (kJ/mol). The free energy change is related to the cell voltage through Faraday's constant (F = 96,485 C/mol) and the number of electrons transferred per mol (n):

$$\Delta G = -nF\Delta E$$

If the electrochemical potentials of the individual electrodes are known, the cell voltage can be calculated by simple addition. For example:

$$\Delta E^o{}_{cell} = E^o{}_{oxidation,\ anode} + E^o{}_{reduction,\ cathode}$$

$$E^o{}_{reduction} = -E^o{}_{oxidation}$$

$$Anode: \quad Zn(s) \rightarrow Zn^{2+} + 2e^- \qquad E^o{}_{oxidation} = 0.76\ V$$

$$+ \quad Cathode: \quad Cu^{2+} + 2e^- \rightarrow Cu(s) \qquad E^o{}_{reduction} = 0.34\ V$$

$$Cell: \quad Zn(s) + Cu^{2+} \rightarrow Zn^{2+} + Cu(s) \qquad \Delta E^o{}_{cell} = 1.1\ V$$

If the half-cell potentials are not known, the free energies (G) associated with each component can be used to calculate ΔG:

$$\Delta G = \sum G_{products} - \sum G_{reactants}$$

$$Zn(s) + Cu^{2+} \rightarrow Zn^{2+} + Cu(s)$$

$$\Delta G = \left(G_{solvation,\ Zn^{2+}} + G_{Cu(s)}\right) - \left(G_{Zn(s)} + G_{solvation,\ Cu^{2+}}\right)$$

The cell voltage largely determines the current that can be extracted from the battery, related through Ohm's law V = IR. The units for current are Amperes (A), where 1 A = 1 C/s and 1 C (Coulomb) = 1.6 x 10^{19} electrons. The power output from a battery can be calculated by multiplying the voltage and current: P = V*I and has units of Watts (W), where 1 W = 1 V*A or 1 Joule/s. The current output and resulting power are often limited by the kinetics of the electrochemical reactions and ability for the battery to shuttle ions between the electrodes quickly. For example, most cell phone batteries have a voltage of ~3.8 V at open-circuit (no current load) but can only withstand 2 - 4 W of charging power, amounting to 500 – 1000 mA of current.

The ability of batteries to store charge is referred to as the charge capacity, which directly translates to the battery lifetime. The units for charge capacity can be derived from the number of electrons available to transfer from the anode to cathode:

$$1.6\,x\,10^{19}\,electrons = 1\,C = \ 1\,A * s = \ 2.8\,x\,10^{-4}\,A * h$$

$$3600\,C = 1\,A * h$$

A charge capacity of 1 mAh indicates that a battery may deliver 1 A of current in 1 hour for a total of 3.6 C of charge. However, the charge capacity typically varies with current load, where larger currents limit the actual capacity of the battery due to internal resistance. The current can also be expressed in relation to the charge capacity, called the C-rate, where a 1 C-rate corresponds to the current that would need to be delivered to discharge the battery in 1 hour. Therefore, the 1/10 C-rate for a 1 mAh battery would be 100 μA.

1.2.3 Reference electrodes

Electrode potentials can only be measured in reference to other electrodes since energy is a relative quantity. Therefore, in order to simplify the way electrode potentials are compared, a

universal scale based on a single reference electrode was developed. The scale is based on the standard hydrogen electrode (SHE), which constitutes an electrochemical half-cell with a platinized electrode catalyzing the reduction or oxidation of hydrogen gas bubbling through an acidic solution:

$$2\,H^{+}(aq) + 2\,e^{-} \rightarrow\ H_2\,(g)$$

The absolute electrode potential of the SHE reaction is 4.44 $\pm$ 0.02 V versus vacuum (0 V) at 25°C and standard conditions (1 bar, 1 M acidic solution), and is set to 0 V on the universal reference scale. The SHE electrode was chosen as a universal reference due to its high stability and resilience against shifts in potential.

In an experimental electrochemical cell, the potential difference between the anode and cathode is often different from the theoretical voltage due to unknown electrochemical processes. Therefore, the absolute potential of either electrode can only be determined by incorporating a stable reference electrode, such as the SHE electrode, into the cell. However, the reference electrode must also be compatible such that the cell does not significantly alter the potential of the reference through chemical change. Therefore, there are a number of other reference electrodes that have known electrode potentials versus the SHE scale that can be substituted. For example, in non-aqueous systems, a common reference electrode is the Ag/Ag^{+} electrode, based on the following electrochemical equilibrium:

$$Ag(s) \leftrightarrow Ag^{+} + e^{-}$$

The Ag/Ag^{+} reference electrode is often prepared by suspending a silver wire into a solution containing a 0.1 M solution of $AgNO_3$ and tetrabutylammonium hexafluorophosphate in acetonitrile, resulting in a relatively stable electrode potential at 0.54 V versus SHE. To ensure the reference electrode remains chemically isolated from the rest of the electrochemical cell, the

reference electrolyte is often separated into a glass container with a glass frit. The glass frit allows for a small amount of ion diffusion between the reference electrode and the electrolyte such that the potential difference between the reference and anode or cathode can be measured.

1.2.4 Electrode-electrolyte interface

When electrodes are placed into an electrolyte, an electrode-electrolyte interface develops. Ions from the electrolyte will interact with the electrode surface until an equilibrium is established. Adsorption of ions onto the surface must be accompanied by diffusion of charges to the surface of the electrode, resulting in what is known as the electric double layer (Figure 1.2). The establishment of the electric double layer is what makes a battery electrochemical in nature since the effect of electrostatics must be considered in addition to chemical processes. Where the chemical potential of an electrode can be expressed through the free energy (μ), the electrochemical potential ($\bar{\mu}$) takes into account the local electrostatic potential at the surface (φ) and the ion charge (z):

$$\bar{\mu} = \mu + zF\varphi$$

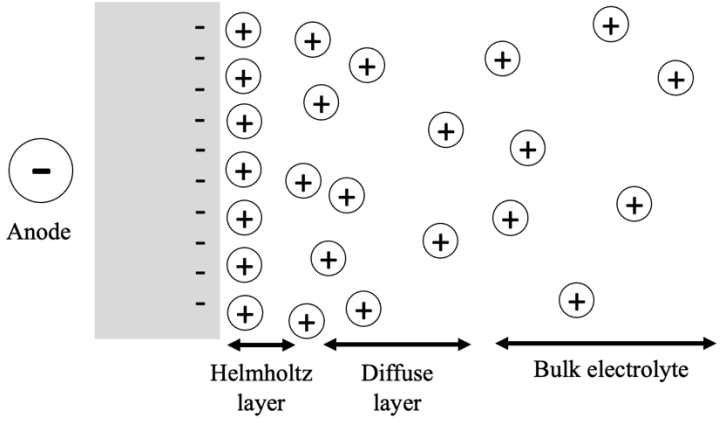


Figure 1.2: Electric double layer structure for a negatively polarized anode surface. Positive ions adsorb at the anode surface to form a dense layer called the Helmholtz layer. The density of ions and local electrostatic potential decreases away from the anode surface.

The inner surface layer of the electric double layer is called the Helmholtz plane and contains the densest packing of adsorbed ions. Here, the electrostatic potential (φ) is the greatest. The density of ions then decreases through the diffuse layer, where ions interact weakly with the polarization field, resulting in a small local electrostatic potential. Past the diffuse layer is the bulk electrolyte where there are little to no effects from the cell polarization.

Another layer that often forms at the electrode-electrolyte interface is a solid-electrolyte interphase, which is composed of decomposition products from reactions between the electrode material and the electrolyte. The stability of the electrolyte against decomposition from the electrodes is related to the energies of the highest occupied molecular orbitals (HOMO) and lowest unoccupied molecular orbitals (LUMO) of molecules within the electrolyte. When the highest HOMO level in the electrolyte is greater in energy than the Fermi level of the cathode, the electrolyte will likely reduce the cathode material. Similarly, when the lowest LUMO level is below the Fermi level of the anode material, the anode will likely reduce molecules in the electrolyte. Therefore, it is desirable for the electrochemical stability window, or separation between HOMO and LUMO levels in the electrolyte, to be wider than the Fermi level difference between the electrodes (Figure 1.3).

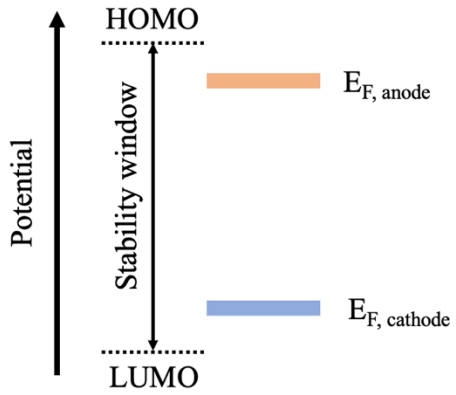


Figure 1.3: Alignment of electrode Fermi levels with HOMO and LUMO of electrolyte. An electrolyte stability window wider than the difference between Fermi energies is desirable to avoid significant electrode decomposition

While the solid-electrolyte interphase is often unavoidable and parasitic towards battery capacity, the SEI can sometimes be beneficial for facilitating charge transport between the electrodes and electrolyte. For example, in lithium-ion batteries with a graphite anode, a Li-rich SEI forms with $LiPF_6$-EC/DEC electrolytes since the HOMO level of the electrolyte is below the Fermi level of the graphite.[12] The SEI only propagates 10 – 20 nm into the graphite anode and remains relatively stable during electrochemical cycling, providing an ion diffusing layer that prevents further decomposition from occurring. However, extended cycling will often cause the electrode to form cracks from volume expansion or contraction, which allows more electrolyte to penetrate the electrode film and form more SEI. The process of electrode cracking and subsequent SEI formation is one of the main culprits for capacity fading in batteries.[13]

1.2.5 Mechanisms of ion insertion

In electrochemical cells where the electrodes are solid materials, there are multiple mechanisms that can be utilized for charge storage. Each mechanism differs in the extent of phase change between the starting and ending structures. The largest volume changes are

associated with the conversion-based mechanism where insertion of ions results in a major phase change with a different crystal structure. An example of a conversion-based electrode in fluoride-ion batteries is CuF_2, which undergoes a phase change from $Fm\bar{3}m$ in Cu metal to $P21/c$ in CuF_2 with a massive 200% volume change.[14] The large volume changes in conversion-based electrodes leads to cracking and capacity fading from electrolyte-mediated degradation, resulting in low battery lifetime. However, conversion-based materials typically have the highest charge capacities due to tight packing of ions.

The smallest volume changes are observed for materials with an intercalation-based mechanism, where ions insert into a rigid material lattice with minor changes in phase. An example of an intercalation-based material for fluoride-ion batteries is La_2CoO_4, where fluoride ions intercalate between layers of the host lattice with a minor 13% volume expansion.[8] The small volume changes translate to enhanced cyclability of the battery since the electrode is less prone to cracking. However, the trade-off is that intercalation-based materials tend to have lower capacities than conversion-based since ions do not pack as densely.

1.2.6 Potentiometry

A potentiostat is an instrument that can apply voltage or current across leads in an electrochemical cell. Potentiometry is useful for characterizing the qualities of batteries such as the voltage, charge capacity, and current density. The simplest measurement with a potentiostat is to determine the voltage between two electrodes without application of current, called the open-circuit potential. The voltage should be close to the theoretical cell potential since there are no effects from cell resistance. The open-circuit potential can often drift initially if the cell has not yet reached a thermodynamic equilibrium, which can be due to active electrode-electrolyte

interface development or unexpected chemical reactions. If drifting continues without stabilization, the cell may be self-discharging and losing charge capacity.

The charging and discharging behavior of a battery can be analyzed using potentiometry by applying either a current or voltage across electrode leads. In galvanostatic mode, a constant current is applied to electrodes in the cell and the voltage output is measured. In potentiostatic mode, a constant voltage is applied and the current is measured, useful for determining the electrochemical reaction kinetics. The magnitude of current applied along with the amount of time passed can be used to calculate the charge capacity in mAh, and the voltage profile can be compared to the theoretical voltage profile of the cell. In general, a plateau in the voltage is observed for every phase change during electrochemical cycling since a change in phase constitutes altering the potential of the electrochemical interface. A typical charge/discharge curve from galvanostatic measurements for a 2-phase system is shown in Figure 1.4 with labels for the charge capacity and cell voltage.

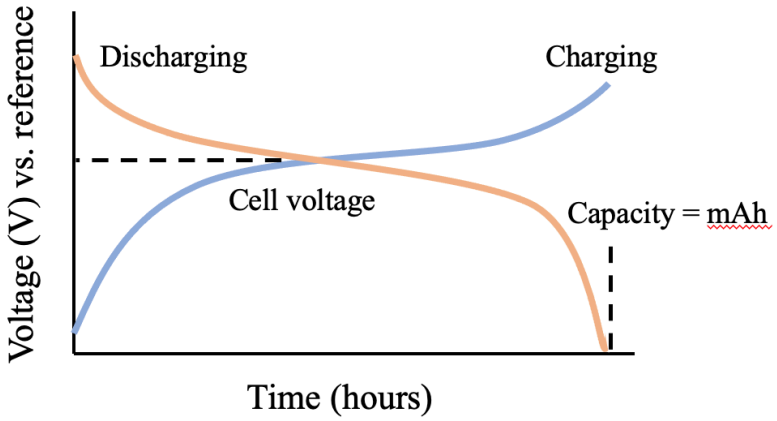


Figure 1.4: Theoretical voltage profile from galvanostatic measurements on a two-phase electrochemical system. The capacity for the charge or discharge process can be calculated by multiplying the amount of time passed by the current applied. The voltage of the cell is the average voltage of the charge and discharge curves

Charging and discharging profiles often deviate from ideal curves due to polarization and resistance in the electrochemical cell. Shifts in the profiles are described as overpotential, where the resistance giving rise to the overpotential can be approximated using Ohm's law V = IR. For example, a 100 μm thick electrode with an area of 1 cm^2 and electrical conductivity of 1 mS/cm under 100 mA of current would exhibit 10 mΩ of resistance and 1 mV of overpotential. The gap between the charging and discharging curves due to overpotential is called the voltage hysteresis, which often undesirable. Moreover, charging and discharging curves often start and end at slightly different potentials due to polarization of the cell. During discharging, the cathode becomes negatively charged while the anode is more positive, shifting the curve towards more negative potentials. The opposite is true for electrochemical charging.

1.3 A History of Fluoride-ion Batteries

1.3.1 Early works on fluoride-ion conductors and batteries

The use of fluoride ions as a charge shuttle in batteries dates back to 1976, when Kennedy and Hunter explored PbF_2 as a solid fluoride-ion electrolyte in a galvanic cell.[5] Prior literature highlighted the moderate ionic conductivity associated with fluorite-type materials, including CaF_2, BaF_2, and PbF_2, which tend to also have a fluoride transport number close to 1, signifying negligible electrical conductivity.[15–17] The ionic conductivity of β-PbF_2 is among the largest among pure fluorite-type materials, with a conductivity of 10^{-5} S/cm at 150°C, sufficient enough for use as a solid electrolyte in fluoride-ion batteries.[18] The following electrochemical reaction was used to generate 0.7 V in a fluoride-ion battery at room temperature:

$$Pb + CuF_2 \rightarrow PbF_2 + Cu \qquad \Delta G = -130\ kJ/mol$$

Due to the low conductivity of CuF_2 (10^{-10} S/cm at 25°C), the cathode was blended with PbF_2 and graphite, improving the conductivity to 10^{-6} S/cm. Unfortunately, the battery was not

reversible and could only be discharged at rates up to 10 μA/cm^2, amounting to a mere 0.01 C of charge. The meager performance was likely due to low utilization of CuF_2 in the cathode and mild conductivity of the β-PbF_2 electrolyte.

Schoonman published work on another fluoride-ion battery in the same year, utilizing a tysonite-type oxide-doped bismuth fluoride, BiO_xF_{3-2x} (x = 0.09 – 0.1), in combination with a AgF-doped β-PbF_2 as the solid electrolyte.[19] Kennedy and Miles had demonstrated an improvement in conductivity of fluorite-type materials by doping with monovalent cations, such as K^+, to increase the concentration of vacancies in the lattice, where fluorite-type materials tend to conduct via vacancies.[20] Using the BiO_xF_{3-2x}/AgF-PbF_2 electrolyte instead of pure β-PbF_2 improved the d-c resistance of the cell by a factor of 10. Furthermore, to overcome conductivity issues with CuF_2, Bi was used as the cathode instead (10^{-4} S/cm at 150 °C). The overall cell reaction and thermodynamic driving force was:

$$3\ Pb + 2\ BiF_3 \rightarrow 3PbF_2 + 2\ Bi \qquad \Delta G = -63\ kJ/mol$$

Similar to the preceding battery, the cell was not reversible, and the charge capacity was still only 0.16 C at 10 μA/cm^2. Voltages of only 0.2 V were obtained due to the lower thermodynamic driving force of the electrochemical reaction. While a significant increase in capacity was expected, the increased thickness in the electrolyte from using slurry casting rather than vacuum deposition likely hampered performance through added resistance.

Danto, et. al. sought to test the consequences of electrode thickness by constructing a similar cell using vacuum deposition instead of slurry casting.[21] AgF and Bi_2O_3 were not used as electrolyte dopants due to the constraints of vacuum deposition, and the cell began in a discharged Bi | PbF_2 | Bi state, where each component was deposited onto a glass substrate with thicknesses < 4 μm. The initial cell was charged to 0.3 V using 0.2 μA over 6 hours, resulting in

Pb | PbF_2 | BiF_3 | Bi. A voltage of 0.2 – 0.3V was generated under a discharge current of 40 $\mu A/cm^2$ at room temperature and 0.04 C of charge was produced, a significant decrease compared to previous galvanic cells. Surprisingly, the authors claimed the cells could be cycled ~10 times with coulombic efficiencies ranging from 70-100%, however no data was shown to support this claim. The ability to reversibly cycle the battery may have been due to the production method, where there was likely improved contact between electrolyte and electrode particles from the production method.

With the observation that aliovalent doping can improve ionic conductivity in fluorite-type materials, Wapenaar and Schoonman investigated the effect of trivalent doping with UF_4 and CeF_3 in $M_{1-x-y}U_xCe_yF_{2+2x+y}$ (M = Ca, Sr, Ba and $0.027 < 2x + y < 0.265$).[22] While doping with monovalent cations improves vacancy-mediated conduction, trivalent doping results in an increased concentration of interstitial fluoride, improving interstitial-mediated conduction. The conductivity was shown to increase super-linearly with dopant concentration, resulting in low activation energies for fluoride transport and moderate conductivity (0.6 eV, 3×10^{-7} S/cm). The ionic conductivity was less than AgF-doped PbF_2 (0.3 eV, 5×10^{-6} S/cm), but this does not preclude the material for use as an electrolyte.[19] Using $Ba_{0.882}U_{0.113}Ce_{0.005}F_{2.231}$ as the solid electrolyte and Pb-$BiO_{0.1}F_{2.8}$ or Pb-BiF_3 as the electrodes allowed for multiple discharge cycles to be completed at room temperature with 0.44 C of charge passed at 10 $\mu A/cm^2$. Additionally, the authors reported data on the ionic conductivity of undoped and doped BiF_3, showing that undoped BiF_3 has a very similar conductivity to $BiO_{0.1}F_{2.8}$, suggesting the undoped form could be used instead of $BiO_{0.1}F_{2.8}$ as the cathode.

While the authors did attempt to employ Ca metal as an anode to increase the theoretical cell voltage to 3.10 V, the formation of resistive CaF_2 leads to irreversible anode passivation.

Therefore, in a future publication, Schoonman and Wolfert attempted to suppress formation of anode passivating CaF_2 layers by alloying the Ca anode with Yb, resulting in anion-excess solid solutions of $Ca_{1-x}Yb_xF_{2+x}$.[23] The presence of Yb^{3+} allows for excess F^- to be stored in interstitial sites of $Ca_{1-x}Yb_xF_{2+x}$. Using the cell geometry $Ca_{1-x}Yb_x$ | $Ca_{0.68}U_{0.02}Ce_{0.30}F_{2.34}$ | $BiO_{0.1}F_{2.8}$, it was shown that the resistance associated with anode passivation was reduced by a factor of 10^3 for an $x = 0.13$, and voltages of 2.4 – 2.6 V could be obtained. While passivation by CaF_2 inhibits cycling of the battery, the charge capacity reached 0.4 - 2.3 C and cell resistance was improved to ~10^5 Ω. The resistance was further improved by employing $Ba_{0.55}La_{0.45}F_{2.45}$ as an electrolyte, which has a lower enthalpic barrier for fluoride transport (0.6 eV). Current densities were improved to 55 μA/cm^2 from 3.8 μA/cm^2 with the $Ca_{0.68}U_{0.02}Ce_{0.30}F_{2.34}$ electrolyte.

In subsequent decades, a period of fluoride-ion electrolyte discovery overshadowed testing of new fluoride-ion batteries, likely due to the bottleneck of low fluoride-ion electrolyte conductivity. A review by Hagenmuller, et. al. in 1981 highlighted the best fluoride-ion conductors known at the time and their mechanisms of conduction.[24] Of greatest promise were doped forms of PbF_2, where introduction of highly polarizable cation dopants, such as Bi^{3+}, Th^{4+} or Sn^{2+}, allowed for conductivities as high as 10^{-2} S/cm at room temperature, such as in $PbSnF_4$. Many studies followed that elucidated the mechanism by which highly polarizable cations dominate conductivity enhancement over other cations previously used (K^+, Ag^+). The concept was extended to the SnF_2-doped BaF_2 system, where $BaSnF_4$ exhibits similar room-temperature conductivities of 10^{-3} S/cm.[25] Another promising electrolyte that would not be employed in an electrochemical cell until 2011 was Ba-doped LaF_3, which has an activation barrier of 0.48 eV and room-temperature conductivity of 10^{-5} S/cm.[26] Compositions with the highest conductivity are $La_{0.95}Ba_{0.05}F_{2.95}$ or $La_{0.9}Ba_{0.1}F_{2.9}$, both having similar barriers for fluoride transport.[27]

1.3.2 The first reversible fluoride-ion battery

Fluoride-ion batteries were revived in 2011 by Reddy and Fichtner, who gave evidence for the first reversible fluoride-ion battery at 160ºC with moderate charge capacity.[4] The authors chose to re-investigate $La_{0.9}Ba_{0.1}F_{2.9}$ as a fluoride-ion electrolyte, finding that the ionic conductivity matched previous studies (2.0 x 10^{-4} S/cm at 160ºC) (Figure 1.1). While the ionic conductivity was low, the electrolyte had a large electrochemical window (> 3 V), allowing for the use of Ce metal as the anode and BiF_3 as the cathode. All cells were discharged at similar current densities to previous studies, 10 μA/cm^2, and exhibited voltages of 2.0 – 2.8 V. The largest discharge capacity was observed for the CuF_2-based cell, amounting to 4.6 C (322 mAh/g), a large improvement since Schoonman, 1976 (0.44 C). Nevertheless, cycling with the CuF_2 was not possible. Electrochemical cycling of the BiF_3-based cell was demonstrated, delivering 42% of the theoretical capacity in the first cycle (1.8 C, 126 mAh/g) and reaching 58 mAh/g after 38 cycles. This work would spark many future studies on improving the integration of moderately conducting solid-state electrolytes with electrode materials to improve cycling. Of primary interest was reducing the thickness of the electrolyte, whose large impedance is a likely culprit for significant capacity fading.

The ionic conductivity of mixed metal fluorides is highly dependent on the method of electrolyte preparation. Traditionally, fluoride-ion conductors were prepared by high temperature ceramic sintering or solution-based syntheses. However, in 2001, Kumar and Sekhon showed that using a mechanical milling synthesis procedure for making $Pb_{1-x}Sn_xF_2$ improved the ionic conductivity due to better overlap between grains.[28] Sobolev repeated this observation for the fluorite-type CaF_2-LaF_3 binary system, showing that $Ca_{0.8}La_{0.2}F_{2.2}$ with 10-30 nm grain sizes has similar ionic conductivity to single crystals in the high-temperature range (> 200ºC).[29]

Mechanochemical synthesis became a promising method for improved electrolyte conductivity and allowed for simplified fabrication of electrodes.

Interestingly, when Reddy and Fichtner utilized mechanochemical synthesis to produce their tysonite-type $La_{0.9}Ba_{0.1}F_{2.9}$ electrolyte, they observed a decrease in conductivity when compared to single crystals.[4] Given that the mechanism of fluoride-ion transport is vacancy-mediated in fluorite-type fluorides and interstitial-mediated in tysonite-type fluorides, Rongeat, et. al. sought to compare the effect of ball-milling synthesis on the conductivity of $Ba_{1-x}La_xF_{2+x}$ (fluorite-type) versus $La_{1-x}Ba_xF_{3-x}$ (tysonite-type) systems.[30,31] The authors found that conduction in $Ba_{1-x}La_xF_{2+x}$ is improved after ball-milling by the addition of vacancy migration pathways through grain boundaries and reduced in $La_{1-x}Ba_xF_{3-x}$ since interstitial conduction is blocked by grain boundaries. While mechanochemical synthesis is a promising technique for preparing fluorite-type electrolytes, it does not translate to tysonite-type electrolytes due to differences in the conduction mechanism.

A number of works were then published on alternative methods for producing low impedance tysonite-type electrolytes, with a particular focus on $La_{1-x}Ba_xF_{3-x}$. In 2015, Zhang, et. al.[32] proposed a sol-gel synthesis of $La_{1-x}Ba_xF_{3-x}$ by spin-coating solutions of La- and Ba-acetates in trifluoroacetic acid onto stainless-steel substrates then annealing in a furnace at 300-400^{o}C, resulting in thin electrolyte layers (5-6 μm). While the ionic conductivity of the resulting $La_{0.9}Ba_{0.1}F_{2.9}$ film at 170^{o}C (8.8×10^{-5} S/cm) was 5x lower than bulk (5×10^{-4} S/cm), the resistance was improved by a factor of 50 due to the reduced thickness. The drop in ionic conductivity was attributed to the porous structure of the film, which increased the grain boundary resistance. A future study[33] showed that annealing at higher temperatures (< 450^{o}C)

improved the conductivity to 1.6 x 10^{-4} S/cm due to an increased density of the electrolyte particles.

An alternative method for wet chemical synthesis of thin-film $La_{1-x}Ba_xF_{3-x}$ electrolytes was proposed by Bhatia, et. al.[34] in 2017 which involved co-precipitation from $La(NO_3)_3{\cdot}6H_2O$ and $Ba(NO_3)_2$ in a solution of water and NH_4F. The resulting powder was pressed into a pellet and sintered at 800°C for 20 hours. A high ionic conductivity of 1.8 x 10^{-5} S/cm at 25°C was observed for nanoparticle films of $La_{0.95}Ba_{0.05}F_{2.95}$, very similar to the conductivity of a single crystal. When used in a similar cell to the 2011 study, with Ce as the anode and BiF_3 as the cathode, an OCV of 2.5 V and initial capacity of 245 mAh/g was observed, 80% of the theoretical capacity. In the second cycle, the capacity faded to only 203 mAh/g, although after 8 cycles, the performance was similar to the 2011 battery. Regardless, a 0.25 V increase in voltage and improved capacity indicated that using wet-chemical thin film preparation of $La_{1-x}Ba_xF_{3-x}$ is a promising strategy for improving cell performance for tysonite-type electrolytes.

In attempts to improve the charge capacity through electrode design, Thieu, et. al. revisited CuF_2 as a cathode material due to its high theoretical capacity of 527 mAh/g and conversion potential of 3.55 V, leading to high specific energy (1874 Wh/kg).[14] In the 2011 study by Reddy and Fichtner, the authors were not able to show reversibility of a CuF_2 cathode.[4] The authors investigated a thin 675 μm stack of La | $La_{0.9}Ba_{0.1}F_{2.9}$ | CuF_2, where La was used as the anode due to the moderate ionic conductivity of LaF_3. The CuF_2/La cells displayed voltages of $\leq$ 2.9 V under a 4 mA/g load and initial discharge capacities of 360 mAh/g, 68% of the theoretical capacity of CuF_2. Discharge in the second cycle resulted in a capacity of 205 mAh/g, a 43% loss, and after 10 cycles the capacity was still moderate at 168 mAh/g. Capacity fading was attributed to gradual diffusion of Cu into the electrolyte, resulting in electrolyte degradation

due to increased electrical conductivity. The improvement in cycling behavior was a result of using ball-milling to prepare the CuF_2 cathode, which allowed for better overlap between CuF_2 and electrolyte particles.

Interest in using fast fluoride-ion conductors such as $PbSnF_4$ and $BaSnF_4$ for room-temperature fluoride-ion batteries revived in 2018 despite the small electrochemical window for electrolyte stability (~ 0.5 V). Mohammad, et. al. employed Zn or Sn as an anode and BiF_3 as the cathode with $BaSnF_4$ as the electrolyte, generating voltages of 0.3 - 0.4 V.[35] When cycled at 150ºC, the initial discharge capacity was 275 mAh/g and decreased to 150 mAh/g after 10 cycles at 20 μA/cm^2, similar to previous studies with $La_{0.9}Ba_{0.1}F_{2.9}$ as the electrolyte. At room-temperature, the initial capacity was 125 mAh/g, decreasing to 10 mAh/g after 10 cycles. Although the energy density was small (37 Wh/kg), the room-temperature capacity and cycling ability improved drastically since Schoonman's cell in 1976 (Pb | $Ba_{0.882}U_{0.113}Ce_{0.005}F_{2.231}$ | BiF_3).[19]

Mohammad, et. al. sought to combine the benefits of $La_{0.9}Ba_{0.1}F_{2.9}$ and $BaSnF_4$ into an interlayer electrolyte that could accommodate electropositive metals (La, Ce) for high voltages and provide moderate ionic conductivities.[36] A thin 45 μm layer of $La_{0.9}Ba_{0.1}F_{2.9}$ was pressed into a thick layer of $BaSnF_4$, increasing the conductivity of the electrolyte by one order of magnitude compared to $La_{0.9}Ba_{0.1}F_{2.9}$ alone (8.9 x 10^{-6} S/cm). The interlayer electrolyte allowed for use of Ce metal as the anode and BiF_3 as the cathode, providing an open-circuit potential of 2.6 V. Unfortunately, the first discharge capacity was only 23 mAh/g at a current density of 10 μA/cm^2, and there was large voltage hysteresis (1.6 V). The capacity faded to 5 mAh/g over five cycles, likely due to the low ionic conductivity of $La_{0.9}Ba_{0.1}F_{2.9}$ at room temperature. Despite exploration

of hundreds of solid-state fluoride-ion electrolytes and electrode fabrication methods, solid-state fluoride-ion batteries are far from reaching the performance of modern Li-ion batteries.

1.3.3 Intercalation-based electrodes

Most fluoride-ion batteries that have been studied incorporate metal fluorides with a conversion-type insertion mechanism as electrodes. While metal fluoride electrodes certainly provide high theoretical charge capacities, their large volume changes result in significant capacity fading during cycling. A more promising mechanism for enabling highly reversible fluoride-ion batteries is intercalation, wherein ions insert into a host lattice that does not significantly change in shape or volume.[37] The usefulness of intercalation-based electrodes in Li-ion batteries has certainly been displayed, where $LiCoO_2$ cathodes undergo small volume changes of ~10% upon Li^+ insertion and can withstand hundreds of charge/discharge cycles.[38] However, there are very few intercalation-based fluoride-ion electrodes known with high capacity. Here we outline a few candidates that have been studied as intercalation-based electrodes.

Among the first intercalation-based structure types to be studied as fluoride-ion electrodes were perovskites, specifically the Ruddleson-Popper phases composed of $A_{x+1}B_xX_{3x+1}$ (A, B = cation; X = anion) with a layered structure. Previous literature had outlined successful topochemical fluorination of $BaFeO_{2.5}$ into fluorine intercalation compounds $BaFeO_{3-y}F_x$ (x = 0.25 – 0.75), inspiring Clemens, et. al. to attempt electrochemical fluorination of the material.[39] Constructing a $BaFeO_{2.5}$ | $La_{0.9}Ba_{0.1}F_{2.9}$ | CeF_3 cell, the $BaFeO_{2.5}$ was able to be charged to $BaFeO_{2.5}F_{0.5}$ at 10 μA/cm^2 and 150^{o}C, amounting to 100% of the theoretical capacity (55 mAh/g). However, the cell was not able to be discharged. Use of MgF_2 as the anode allowed for multiple cycles at 3 V, but at the cost of only 5 mAh/g of capacity. This initial study on

perovskite electrodes highlights the trade-off that exists for intercalation-based compounds: improved cyclability comes at the expense of lower charge capacity.

The authors also investigated another Ruddleson-Popper phase reported to have been chemically fluorinated with F_2 at elevated temperatures, $LaSrMnO_4$.[7] The predicted $LaSrMnO_4F_{1.7}$ intercalation compound has a theoretical gravimetric capacity of 132 mAh/g and high electrochemical potential (2 V vs. Pb/PbF_2), 0.6 V higher than CuF_2, which has been used in high-voltage fluoride-ion batteries. Using a PbF_2 anode, which has a moderate fluoride-ion conductivity, and $La_{0.9}Ba_{0.1}F_{2.9}$ electrolyte at 170ºC, the $LaSrMnO_4$ material was able to be fluorinated to $LaSrMnO_4F_{1.3\text{-}1.5}$ at 1.5 V vs. Pb/PbF_2. At these extreme potentials, the carbon additive undergoes fluorination, contributing towards irreversible charge capacity, suggesting the need for alternative conductive additives such as carbon nanotubes. Despite the high fluorine loading into $LaSrMnO_4$, only 25 mAh/g could be extracted (~ 25% fluorine) due to large overpotentials in the cell set-up, and reversibility was near impossible because of the parasitic carbon fluorination. Forced discharging of the $LaSrMnO_4F_{1.3\text{-}1.5}$ material did result in complete defluorination of the lattice, indicating that the material may indeed reversibly incorporate fluoride ions. The study of the cyclability of intercalation-based electrodes is inherently hindered by testing against conversion-based electrodes[40], which have a detrimental effect on reversibility. Development of both anodes and cathodes with intercalation-based mechanisms is therefore needed.

In a subsequent publication, Nowroozi, et. al. hypothesized that a milder electrochemical potential than the Mn^{3+} to Mn^{5+} couple might be accessed by Co^{2+}/Co^{3+}, with intentions of avoiding the carbon decomposition issue.[8] The perovskite material La_2CoO_4, which had not been investigated as a fluorine intercalation compound previously, was able to be electrochemically

charged to $La_2CoO_4F_{1.2}$ at 0.8 V vs. Pb/PbF_2 and ~100 mAh/g, avoiding the effects of carbon fluorination at higher potentials (~ 1.5 V). With a capacity cut-off of 65 mAh/g, a PbF_2 | $La_{0.9}Ba_{0.1}F_{2.9}$ | La_2CoO_4 at 170ºC showed the highest reversibility of any fluoride-ion battery studied previously. The capacity faded to 15 mAh/g over 20 cycles, a drop of only ~50% compared to the first discharge (35 mAh/g), and an improvement compared to the 25% capacity drop over 20 cycles observed with conversion-based BiF_3 cathodes. Another material investigated, $LaNiO_{4+d}$, exhibited even longer cyclability with over 220 cycles completed at 30 mAh/g and Coulombic efficiencies as high as 95-99%. Intercalation-based electrodes have promise for fluoride-ion batteries with good reversibility, however materials with higher capacity for storing fluoride need to be discovered.

1.3.4 Liquid electrolytes for fluoride-ion batteries

The development of liquid fluoride-ion electrolytes for batteries is motivated by the need for better ionic conductivity in the electrolyte and a wider electrochemical stability window. However, many fluoride-ion solutions with organic-based solvents contain significant amounts of HF_2^- or have low F^- ion transference numbers, indicating F^- is strongly bound to solvating cations.[41] Moreover, F^- can act as a strong nucleophile and degrade electrode electrolyte components. Nevertheless, multiple liquid fluoride-ion electrolytes have shown promise for improving the room-temperature performance of fluoride-ion batteries.

One of the first liquid fluoride-ion electrolytes developed with adequate properties was an ionic liquid composed of 0.1 M tetramethylammonium fluoride dissolved in 1-methyl-1-propylpiperidinium bis(trifluoromethanesulfonyl)imide, which has an ionic conductivity of ~ 1 x 10^{-3} S/cm at room temperature and is stable to 200ºC.[42] The first Ag/Ag^+ reference electrode was incorporated into a fluoride-ion cell, allowing for an accurate measurement of the

electrochemical stability window to be -3.5 – 3 V vs. Ag/Ag^+, a significantly larger window than preceding solid electrolytes. Use of a PbF_2 cathode and polyaniline (PANI) anode in a coin cell displayed an initial discharge capacity of 103 mAh/g at ~ 1 V, fading to only 96 mAh/g in the second cycle. However, no subsequent cycling was performed, and little evidence was given for phase transformations in the electrodes.

Okazaki, et. al. investigated another ionic-liquid-based fluoride-ion electrolyte with high ionic conductivity, 0.35 M 1-methyl-1-propylpiperidinium fluoride in N,N,N-trimethyl-N-propylammonium bis(trifluoromethanesulfonyl)amide (TMPA-TFSA), and provided a more detailed picture of the structural changes and cyclability of PbF_2 and Bi electrodes.[43] While the battery only produced ~0.5 V, reversible formation of Pb and BiF_3 was observed over at least 5 cycles and a first discharge capacity of 0.15 mAh was produced at 20 $\mu A/cm^2$.

Konishi, et.al. explored an alternate approach to fluoride-ion charge storage by utilizing a dissolution-deposition mechanism, where a metal fluoride electrode reversibly deposits onto an electrode surface.[44] In this strategy, an electrode such as BiF_3 partially dissolves into the electrolyte upon contact, then application of a discharge current drives the deposition of Bi^0 and dissolution of BiF_3 into Bi^{3+} and F^-. The reverse process occurs during charging. Therefore, an electrolyte that dissolves metal fluorides easily is required. Konishi sought to enhance the dissolution of CsF into tetraglyme by using an "anion acceptor", such as fluorobis(2,4,6-trimethylphenyl)borane (FBTM-PhB), to improve F^- solvation in the organic solvent. The solubility of F^- was improved to 0.5 M, ideal for use as a fluoride-ion electrolyte. While the ionic conductivity was not evaluated, the electrolyte exhibited a moderate electrochemical window of -2.2 to -0.3 V, measured using a Ag/Ag^+ reference electrode in a Pt symmetrical cell. The "reserve-type" half-cell using BiF_3 as the electrode showed a first discharge capacity of 300

mAh/g at 1/40 C, fading completely after 10 cycles. However, the electrolyte has never been employed in a full battery.

A remarkable breakthrough in liquid fluoride-ion electrolyte development came with work by Davis, et. al. demonstrating a room-temperature electrolyte with high F^- solubility and a large electrochemical stability window.[11] Inspired by the relatively high solubility of tetraalkylammonium fluoride salts in organic solvents, neopentyl-substituted alkylammonium salts were investigated due to their resilience against β-hydrogen elimination to HF_2^-. A screening of potential solvents highlighted the usefulness of partially fluorinated ethers for F^- solvation, where solutions of N,N,N-trimethyl-N-neopentylammonium fluoride (Np_1Me_3NF) in bis(trifluoroethyl)ether (BTFE) reached concentrations of 2 M and conductivities of 2.5 mS/cm at room temperature. Moreover, the electrochemical stability window was large at -2.5 – 0.5 V vs. Ag/Ag^+.

Similar to the electrolyte used for a reserve-type fluoride shuttle battery, though, metal fluoride dissolution was significant. Therefore, the authors employed perfluorooctyltriethoxysilane (FOTS) or LaF_3 as an artificial SEI between the electrode and electrolyte, which eliminated the dissolution issue. Using core-shell nanostructures LaF_3-Cu particles as the cathode material, a charge capacity of 40 mAh/g could be retained over 7 cycles, indicating good reversibility but low charge storage. A Ce anode with a surface FOTS layer was also able to be cycled reversibly. Although some engineering is required for incorporating metal fluorides into the Np_1Me_3NF/BTFE electrolyte, there are clear advantages to the ionic conductivity and electrochemical stability window that could enable high-voltage, high-capacity fluoride-ion batteries.

1.4 A Brief History of Electrides[1]

The classic concept of an ionic solid is a crystal made of oppositely charged ions, like NaCl, but in electrides, the negative ‘‘ion’’ is just an electron that lacks an atomic nucleus. While traditional ionic solids are hard, brittle, and electrically insulating, electrides can be soft, malleable, and among the most conductive materials known. To explain the unusual properties of electrides, we outline the development of their principles, learned through a century of research. The concepts that explain the properties of electrides originate from the history of solvated electrons (Figure 1.5a) and color centers.[10] In the 1900s, Kraus[45] introduced the idea of anionic electrons in his explanation of the dissolution of metals in liquid ammonia, ‘‘The negative ion constitutes a new species of anion, an electron, surrounded by an envelope of solvent molecules.’’[46] Mounting evidence corroborated the idea of an anionic electron solvated in fluid. Then, researchers explored many of the same ideas in solids. Mott and de Boer rationalized color centers—crystal defects that cause transparent crystals like NaCl to absorb visible light—to be point defects in the crystal consisting of trapped anionic electrons or cationic holes.[47,48] The most famous of these is the F-center, in which an electron fills an anion vacancy.

[1] Reproduced from Ref. 73 with permission from The Royal Society of Chemistry.

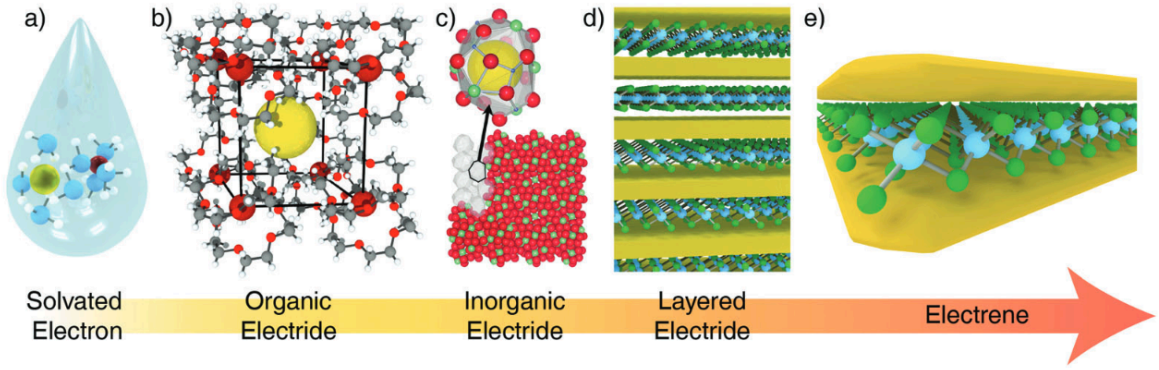


Figure 1.5: Historical progression of electrides. The progression of anionic electrons from (a) solvated electrons to (b) organic electrides[49] to (c) inorganic electrides[50] to (d) layered electrides to (e) electrenes.

Because an F-center is a defect and not a periodic component of the crystal, the concentration of anionic electrons in a solid with F-centers is usually low. In the early 1980s, however, Dye demonstrated that the compound, $Cs^{+}(18\text{-crown-}6)_2(e^{-})$, had anionic electrons at a concentration equal to that of Cs metal.[51–54] The unpaired, anionic electrons reside in periodic spherical cavities between the complexed cations (Figure 1.5b). He called this type of solid an ‘‘electride.’’ Despite the successful synthesis of an electride, Dye’s organic electrides decomposed at room temperature and prompted many to believe that electrides are unstable compounds. A breakthrough came in 2003, when Matsuishi succeeded in synthesizing a thermally stable electride, in which an inorganic lattice hosts the anionic electrons (Figure 1.5c).[55] Through high-temperature treatment with calcium metal, Matsuishi replaced the oxygen anions in mayenite, $[Ca_{24}Al_{28}O_{64}]^{4+}(2O_2^{-})$, with electrons to form an electride, $[Ca_{24}Al_{28}O_{64}]^{4+}(4e^{-})$. The synthesis of large single crystals of $[Ca_{24}Al_{28}O_{64}]^{4+}(4e^{-})$ allowed measurements of intrinsic properties like electrical mobility[56,57] and demonstrated that electrides can be stable materials.[58]

While research on the properties of thermally stable, inorganic electrides gained momentum, Dye came to an important generalization about the structure of electrides: the electron density distribution resembles the available void space.[59] In the organic electrides, the void space is determined by the location of the van der Waals surfaces of the organic molecules.[10] In the inorganic electrides, the void space is determined by the atomic crystal lattice. By engineering the crystal lattice, almost any geometry of void space, and therefore almost any geometry of anionic electron density, is possible. Thus, by 2015, 0D, 1D, and 2D electron density distributions were demonstrated.[55,60–62]

In the 1950s and 1960s, researchers synthesized layered crystals (Ba_2N, Sr_2N and Ca_2N)[63] that possess a 2D void space[60,64] (Figure 1.5d). The layered structures had surprisingly large interlayer distances (e.g. 3.85 Å in Ca_2N). To account for the large interlayer distance in Ca_2N, Keve et al. speculated that ‘‘excess electrons [are] situated in the large gaps between layers’’.[60] This speculation was not widely accepted at first. For example, Brice et al. suggested that Sr_2N was, in fact, Sr_2NH.[65] But neutron diffraction experiments later ruled out the presence of H (e.g. as a hydride) in Sr_2N[66] and Ca_2N.[67] Brese et al. proposed another hypothesis that Sr_2N could have oxidation states of +1.5 (Sr) and -3 (N) rather than +2 (Sr), -3 (N), and -1 (an anionic electron). In 2000, careful electronic structure calculations showed that electrons existed between layers of atoms,[68] which agreed with X-ray and ultraviolet photoemission spectroscopy.[69] Because of the layered lattice, the anionic electrons are confined to a 2D void space.

The confinement of the anionic electrons into a 2D plane profoundly affects how the electrons behave. Density functional theory (DFT) calculations indicate that the anionic electrons partially delocalize into a 2D electron gas.[61,70] Experimental evidence supports this description. Low magnetic susceptibility, consistent with weak Pauli paramagnetism, indicates that the

anionic electrons are paired.[66,67] The strongest evidence of the 2D electron gas confined between planes of atoms is the observation of metallic conduction with high in-plane electrical mobility and low out-of-plane mobility.[61] In a groundbreaking work, Hosono and coworkers performed electrical and photoemission experiments on single crystals of layered electrides and demonstrated, in addition to high in-plane electrical mobility, strong anisotropy in the magnetoresistance and work function, which further support the designation as a 2D electron gas.[61]

Zhao et al. suggested controlling not just the void space, but the morphology of the entire crystal.[71] They used DFT calculations to predict that a single layer of Ca_2N—just three atoms thick—can exist and, astonishingly, still has an electron gas on both sides of the layer. Seizing on this opportunity and drawing on research ideas from the community exploring 2D materials, we experimentally synthesized 2D Ca_2N by exfoliating the layered Ca_2N crystal into 2D flakes. This is the first demonstration of an electride as a 2D material, which we refer to as an ‘‘electrene’’ (Figure 1.5e).[72] By thinning the crystal down to a monolayer, we expect that we can interact with the 2D electron gas in ways—chemically, electronically, optically, etc. —that are not possible with a bulk material or any other known system.

REFERENCES

(1) Intergovernmental Panel on Climate Change. *Climate change 2014 mitigation of climate change*; Cambridge University Press: Cambridge, 2014.

(2) Grey, C. P.; Hall, D. S. Prospects for lithium-ion batteries and beyond-a 2030 vision. *Nat. Commun.* **2020**, *11* (1), 6279.

(3) Thackeray, M. M.; Wolverton, C.; Isaacs, E. D. Electrical energy storage for transportation—approaching the limits of, and going beyond, lithium-ion batteries. *Energy Environ. Sci.* **2012**, *5* (7), 7854.

(4) Anji Reddy, M.; Fichtner, M. Batteries based on fluoride shuttle. *J. Mater. Chem.* **2011**, *21* (43), 17059.

(5) Kennedy, J. H. Thin-Film Galvanic Cell Pb/PbF_2/PbF_2, CuF_2/Cu. *J. Electrochem. Soc.* **1976**, *123* (1), 10.

(6) Nowroozi, M. A.; Wissel, K.; Donzelli, M.; Hosseinpourkahvaz, N.; Plana-Ruiz, S.; Kolb, U.; Schoch, R.; Bauer, M.; Malik, A. M.; Rohrer, J.; et al. High cycle life all-solid-state fluoride ion battery with La_2NiO_{4+d} high voltage cathode. *Commun. Mater.* **2020**, *1* (1), 27.

(7) Nowroozi, M. A.; Wissel, K.; Rohrer, J.; Munnangi, A. R.; Clemens, O. $LaSrMnO_4$: reversible electrochemical intercalation of fluoride ions in the context of fluoride ion batteries. *Chem. Mater.* **2017**, *29* (8), 3441–3453.

(8) Nowroozi, M. A.; Ivlev, S.; Rohrer, J.; Clemens, O. La_2CoO_4: a new intercalation based cathode material for fluoride ion batteries with improved cycling stability. *J. Mater. Chem. A* **2018**.

(9) Druffel, D. L.; Pawlik, J. T.; Sundberg, J. D.; McRae, L. M.; Lanetti, M. G.; Warren, S. C. First-Principles Prediction of Electrochemical Electron-Anion Exchange: Ion Insertion without Redox. *J. Phys. Chem. Lett.* **2020**, 9210–9214.

(10) Dye, J. L. Electrides: ionic salts with electrons as the anions. *Science* **1990**, *247* (4943), 663–668.

(11) Davis, V. K.; Bates, C. M.; Omichi, K.; Savoie, B. M.; Momčilović, N.; Xu, Q.; Wolf, W. J.; Webb, M. A.; Billings, K. J.; Chou, N. H.; et al. Room-temperature cycling of metal fluoride electrodes: Liquid electrolytes for high-energy fluoride ion cells. *Science* **2018**, *362* (6419), 1144–1148.

(12) Zeng, Z.; Liang, W.-I.; Liao, H.-G.; Xin, H. L.; Chu, Y.-H.; Zheng, H. Visualization of electrode-electrolyte interfaces in $LiPF_6$/EC/DEC electrolyte for lithium ion batteries via in situ TEM. *Nano Lett.* **2014**, *14* (4), 1745–1750.

(13) An, S. J.; Li, J.; Daniel, C.; Mohanty, D.; Nagpure, S.; Wood, D. L. The state of understanding of the lithium-ion-battery graphite solid electrolyte interphase (SEI) and its relationship to formation cycling. *Carbon N. Y.* **2016**, *105*, 52–76.

(14) Thieu, D. T.; Fawey, M. H.; Bhatia, H.; Diemant, T.; Chakravadhanula, V. S. K.; Behm, R. J.; Kübel, C.; Fichtner, M. CuF_2 as reversible cathode for fluoride ion batteries. *Adv. Funct. Mater.* **2017**, *27* (31), 1701051.

(15) Ure, R. W. Ionic conductivity of calcium fluoride crystals. *J. Chem. Phys.* **1957**, *26* (6), 1363–1373.

(16) Barsis, E.; Taylor, A. F^- vacancy conductivity in baf_2 crystals. *J. Chem. Phys.* **1968**, *48* (10), 4357–4361.

(17) Tubandt, C. Über Elektrizitätsleitung in festen kristallisierten Verbindungen. Zweite Mitteilung. Überführung und Wanderung der Ionen in einheitlichen festen Elektrolyten. *Z. anorg. allg. Chem.* **1921**, *115* (1), 105–126.

(18) Kennedy, J. H.; Miles, R.; Hunter, J. Solid electrolyte properties and crystal forms of lead fluoride. *J. Electrochem. Soc.* **1973**, *120* (11), 1441.

(19) Schoonman, J. A Solid-State Galvanic Cell with Fluoride-Conducting Electrolytes. *J. Electrochem. Soc.* **1976**, *123* (12), 1772.

(20) Kennedy, J. H. Ionic Conductivity of Doped Beta-Lead Fluoride. *J. Electrochem. Soc.* **1976**, *123* (1), 47.

(21) Danto, Y.; Poujade, G.; Pistré, J. D.; Lucat, C.; Salardenne, J. A Pb|PbF2|BiF_3|Bi thin solid film reversible galvanic cell. *Thin Solid Films* **1978**, *55* (3), 347–354.

(22) Wapenaar, K. E. D. The Ionic Conductivity of Fluorite-Structured Solid Solutions of Composition: MF_2:UF_4:CeF_3 (M = Ca, Sr, Ba). *J. Electrochem. Soc.* **1979**, *126* (4), 667.

(23) Schoonman, J. Alloy-Anodes in Fluoride Solid-State Batteries. *J. Electrochem. Soc.* **1981**, *128* (7), 1522.

(24) Hagenmuller, P.; Reau, J.; Lucat, C.; Matar, S.; Villeneuve, G. Ionic conductivity of fluorite-type fluorides. *Solid State Ionics* **1981**, *3-4*, 341–345.

(25) Denes, G.; Birchall, T.; Sayer, M.; Bell, M. BaSnF4 — A new fluoride ionic conductor with the α-$PbSnF_4$ structure. *Solid State Ionics* **1984**, *13* (3), 213–219.

(26) Schoonman, J.; Oversluizen, G.; Wapenaar, K. Solid electrolyte properties of LaF_3. *Solid State Ionics* **1980**, *1* (3-4), 211–221.

(27) Roos, A.; Vandepol, F.; Keim, R.; Schoonman, J. Ionic conductivity in tysonite-type solid solutions $La_{1-x}Ba_xF_{3-x}$. *Solid State Ionics* **1984**, *13* (3), 191–203.

(28) Kumar, M.; Sekhon, S. S. Mixed fluoride ion conductors prepared by a mechanical milling technique: effect of grain size and strain on the ionic conductivity. *J. Phys. D, Appl. Phys.* **2001**, *34* (19), 2995–3002.

(29) Sobolev, B. P.; Sviridov, I. A.; Fadeeva, V. I.; Sul'yanov, S. N.; Sorokin, N. I.; Zhmurova, Z. I.; Herrero, P.; Landa-Canovas, A.; Rojas, R. M. Mechanochemical synthesis of nonstoichiometric fluorite $Ca_{1-x}La_xF_{2+x}$ nanocrystals from CaF_2 and LaF_3 single crystals. *Crystallogr. Rep.* **2005**, *50* (3), 478–485.

(30) Rongeat, C.; Reddy, M. A.; Witter, R.; Fichtner, M. Nanostructured Fluorite-Type Fluorides As Electrolytes for Fluoride Ion Batteries. *J. Phys. Chem. C* **2013**, *117* (10), 4943–4950.

(31) Rongeat, C.; Anji Reddy, M.; Diemant, T.; Behm, R. J.; Fichtner, M. Development of new anode composite materials for fluoride ion batteries. *J. Mater. Chem. A* **2014**, *2* (48), 20861–20872.

(32) Zhang, L.; Anji Reddy, M.; Fichtner, M. Development of tysonite-type fluoride conducting thin film electrolytes for fluoride ion batteries. *Solid State Ionics* **2015**, *272*, 39–44.

(33) Zhang, L.; Anji Reddy, M.; Gao, P.; Fichtner, M. Development of dense solid state thin-film electrolyte for fluoride ion batteries. *J. Alloys Compd.* **2016**, *684*, 733–738.

(34) Bhatia, H.; Thieu, D. T.; Pohl, A. H.; Chakravadhanula, V. S. K.; Fawey, M. H.; Kübel, C.; Fichtner, M. Conductivity Optimization of Tysonite-type $La_{1-x}Ba_xF_{3-x}$ Solid Electrolytes for Advanced Fluoride Ion Battery. *ACS Appl. Mater. Interfaces* **2017**, *9* (28), 23707–23715.

(35) Mohammad, I.; Witter, R.; Fichtner, M.; Anji Reddy, M. Room-Temperature, Rechargeable Solid-State Fluoride-Ion Batteries. *ACS Appl. Energy Mater.* **2018**, *1* (9), 4766–4775.

(36) Mohammad, I.; Witter, R.; Fichtner, M.; Reddy, M. A. Introducing Interlayer Electrolytes: Toward Room-Temperature High-Potential Solid-State Rechargeable Fluoride Ion Batteries. *ACS Appl. Energy Mater.* **2019**, *2* (2), 1553–1562.

(37) Hannah, D. C.; Sai Gautam, G.; Canepa, P.; Ceder, G. On the balance of intercalation and conversion reactions in battery cathodes. *Adv. Energy Mater.* **2018**, *8* (20), 1800379.

(38) Lyu, Y.; Wu, X.; Wang, K.; Feng, Z.; Cheng, T.; Liu, Y.; Wang, M.; Chen, R.; Xu, L.; Zhou, J.; et al. An overview on the advances of $LiCoO_2$ cathodes for lithium-ion batteries. *Adv. Energy Mater.* **2020**, 2000982.

(39) Clemens, O.; Rongeat, C.; Reddy, M. A.; Giehr, A.; Fichtner, M.; Hahn, H. Electrochemical fluorination of perovskite type $BaFeO_{2.5}$. *Dalton Trans.* **2014**, *43* (42), 15771–15778.

(40) Nowroozi, M. A.; Clemens, O. Insights on the Behavior of Conversion-Based Anode Materials for Fluoride Ion Batteries by Testing against an Intercalation-Based Reference Cathode. *ACS Appl. Energy Mater.* **2018**, *1* (11), 6626–6637.

(41) Davis, V. K.; Munoz, S.; Kim, J.; Bates, C. M.; Momčilović, N.; Billings, K. J.; Miller, T. F.; Grubbs, R. H.; Jones, S. C. Fluoride-ion solvation in non-aqueous electrolyte solutions. *Mater. Chem. Front.* **2019**, *3* (12), 2721–2727.

(42) Gschwind, F.; Zao-Karger, Z.; Fichtner, M. A fluoride-doped PEG matrix as an electrolyte for anion transportation in a room-temperature fluoride ion battery. *J. Mater. Chem. A* **2014**, *2* (5), 1214–1218.

(43) Okazaki, K.; Uchimoto, Y.; Abe, T.; Ogumi, Z. Charge–discharge behavior of bismuth in a liquid electrolyte for rechargeable batteries based on a fluoride shuttle. *ACS Energy Lett.* **2017**, *2* (6), 1460–1464.

(44) Konishi, H.; Minato, T.; Abe, T.; Ogumi, Z. Electrochemical Performance of a Bismuth Fluoride Electrode in a Reserve-Type Fluoride Shuttle Battery. *J. Electrochem. Soc.* **2017**, *164* (14), A3702–A3708.

(45) Kraus, C. A. Solutions of metals in non-metallic solvents; i. general properties of solutions of metals in liquid ammonia. *J. Am. Chem. Soc.* **1907**, *29* (11), 1557–1571.

(46) Kraus, C. A. SOLUTION OF METALS IN NON-METALLIC SOLVENTS; II. ON THE FORMATION OF COMPOUNDS BETWEEN METALS AND AMMONIA. *J. Am. Chem. Soc.* **1908**, *30* (5), 653–668.

(47) Boer, J. H. de; Verwey, E. J. W. Semi-conductors with partially and with completely filled$_3$ *d* -lattice bands. *Proc. Phys. Soc.* **1937**, *49* (4S), 59–71.

(48) Mott, N. F.; Peierls, R. Discussion of the paper by de Boer and Verwey. *Proc. Phys. Soc.* **1937**, *49* (4S), 72–73.

(49) Dye, J. L. Electrides: From 1D Heisenberg Chains to 2D Pseudo-Metals. *Inorg. Chem.* **1997**, *36* (18), 3816–3826.

(50) Toda, Y.; Hirayama, H.; Kuganathan, N.; Torrisi, A.; Sushko, P. V.; Hosono, H. Activation and splitting of carbon dioxide on the surface of an inorganic electride material. *Nat. Commun.* **2013**, *4*, 2378.

(51) Dye, J. L. Recent developments in the synthesis of alkalides and electrides. *J. Phys. Chem.* **1984**, *88* (17), 3842–3846.

(52) Issa, D.; Ellaboudy, A.; Janakiraman, R.; Dye, J. L. Magnetic susceptibilities and electron paramagnetic resonance spectra of a ceside and an electride. *J. Phys. Chem.* **1984**, *88* (17), 3847–3851.

(53) Huang, R. H.; Faber, M. K.; Moeggenborg, K. J.; Ward, D. L.; Dye, J. L. Structure of K^+(cryptand[2.2.2]) electride and evidence for trapped electron pairs. *Nature* **1988**, *331* (6157), 599–601.

(54) Issa, D.; Dye, J. Thermodynamics of formation of Na^+(cryptand[2.2.1]). Na^+ from the metal and complexant. *Inorganica Chimica Acta.* **1989**, *160* (1), 111-113.

(55) Matsuishi, S.; Toda, Y.; Miyakawa, M.; Hayashi, K.; Kamiya, T.; Hirano, M.; Tanaka, I.; Hosono, H. High-density electron anions in a nanoporous single crystal: $[Ca_{24}Al_{28}O_{64}]^{4+}(4e^-)$. *Science* **2003**, *301* (5633), 626–629.

(56) Miyakawa, M.; Kim, S. W.; Hirano, M.; Kohama, Y.; Kawaji, H.; Atake, T.; Ikegami, H.; Kono, K.; Hosono, H. Superconductivity in an inorganic electride $12CaO_x{\cdot}7Al_2O_3{:}e^-$. *J. Am. Chem. Soc.* **2007**, *129* (23), 7270–7271.

(57) Toda, Y.; Yanagi, H.; Ikenaga, E.; Kim, J. J.; Kobata, M.; Ueda, S.; Kamiya, T.; Hirano, M.; Kobayashi, K.; Hosono, H. Work Function of a Room-Temperature, Stable Electride $[Ca_{24}Al_{28}O_{64}]^{4+}(e^-)_4$. *Adv. Mater. Weinheim* **2007**, *19* (21), 3564–3569.

(58) Kim, S. W.; Shimoyama, T.; Hosono, H. Solvated electrons in high-temperature melts and glasses of the room-temperature stable electride $[Ca_{24}Al_{28}O_{64}]^{4+}{\cdot}4e^-$. *Science* **2011**, *333* (6038), 71–74.

(59) Dye, J. L.; Wagner, M. J.; Overney, G.; Huang, R. H.; Nagy, T. F.; Tománek, D. Cavities and channels in electrides. *J. Am. Chem. Soc.* **1996**, *118* (31), 7329–7336.

(60) Keve, E. T.; Skapski, A. C. Ca_2N: a nitride with a layer structure. *Chem. Commun. (London)* **1966**, No. 22, 829.

(61) Lee, K.; Kim, S. W.; Toda, Y.; Matsuishi, S.; Hosono, H. Dicalcium nitride as a two-dimensional electride with an anionic electron layer. *Nature* **2013**, *494* (7437), 336–340.

(62) Zhang, Y.; Xiao, Z.; Kamiya, T.; Hosono, H. Electron Confinement in Channel Spaces for One-Dimensional Electride. *J. Phys. Chem. Lett.* **2015**, *6* (24), 4966–4971.

(63) Ariya, S. M.; Prokofyeva, E. A.; Matveeva, I. I. Investigation of metallic nitrides: II. the subnitrides of strontium and barium. *Journal of general chemistry of the USSR* **1955**, *25*, 634.

(64) Gaudé, J.; L'Haridon, P.; Laurent, Y.; Lang, J. The strontium-nitrogen system. III. structural study of Sr_2N. *Bull. Soc. fr. Mineral. Crustallogr.* **1972**, No. 95, 56–60.

(65) Brice, J. F.; Motte, J. P.; Aubry, J. On the “abnormal” nitrides of the alkaline earth metals Ca_2N, Sr_2N and SrN. *Revue de Chimie Minerale* **1975**, *12*, 105.

(66) Brese, N. E.; O' ' 'keeffe, M. Synthesis, Crystal Structure, and Physical Properties of Sr_2N. *Journal of Solid State Chemistry* **1990**, *87*, 134–140.

(67) Gregory, D. H.; Bowman, A.; Baker, C. F.; Weston, D. P. Dicalcium nitride, Ca_2N—a 2D “excess electron” compound; synthetic routes and crystal chemistry. *J. Mater. Chem.* **2000**, *10* (7), 1635–1641.

(68) Fang, C. M.; de Wijs, G. A.; de Groot, R. A.; Hintzen, H. T.; de With, G. Bulk and Surface Electronic Structure of the Layered Sub-Nitrides Ca_2N and Sr_2N. *Chem. Mater.* **2000**, *12* (7), 1847–1852.

(69) Steinbrenner, U.; Adler, P.; Hölle, W.; Simon, A. Electronic structure and chemical bonding in alkaline earth metal subnitrides: photoemission studies and band structure calculations. *Journal of Physics and Chemistry of Solids* **1998**, *59* (9), 1527–1536.

(70) Walsh, A.; Scanlon, D. O. Electron excess in alkaline earth sub-nitrides: 2D electron gas or 3D electride? *J. Mater. Chem. C* **2013**, *1* (22), 3525.

(71) Zhao, S.; Li, Z.; Yang, J. Obtaining two-dimensional electron gas in free space without resorting to electron doping: an electride based design. *J. Am. Chem. Soc.* **2014**, *136* (38), 13313–13318.

(72) Druffel, D. L.; Kuntz, K. L.; Woomer, A. H.; Alcorn, F. M.; Hu, J.; Donley, C. L.; Warren, S. C. Experimental demonstration of an electride as a 2D material. *J. Am. Chem. Soc.* **2016**, *138* (49), 16089–16094.

(73) Druffel, D. L.; Woomer, A. H.; Kuntz, K. L.; Pawlik, J. T.; Warren, S. C. Electrons on the surface of 2D materials: from layered electrides to 2D electrenes. *J. Mater. Chem. C*, **2017**, *5*, 11196

CHAPTER 2: METHODS

2.1 Computational Methods

2.1.1 Density-functional theory calculations

Density functional theory (DFT) calculations were performed using the CASTEP code[1] with plane-wave basis set approximations[2]. To describe core electrons, ultrasoft pseudopotentials were used with a cut-off energy of 500 eV. For this cut-off energy, calculations were convergent with $dE_{tot}/dlnE_{cut}$ less than 0.01 meV/atom. Geometry optimizations of all structures were first performed. A GGA PBE functional[3] was used for the exchange-correlation contribution to total energy, and Tkatchenko and Scheffler's correction[4] was used to account for long-range dispersion forces for all calculations except where noted. A Monkhorst-Pack grid[5] of 16×16×8 k-points was used, and structures were optimized using a BFGS algorithm with a convergence tolerance of 5.0×10^{-7} eV/atom for energy, 0.01 eV/Å for max force, 0.02 GPa for max stress, and 5.0×10^{-4} Å for max displacement.

For calculations of the activation barrier for F^- diffusion in Y_2CF_2, we used a 3x3x2 supercell with a single fluorine atom removed and an anionic electron occupying its tetrahedral F^- site ($Y_2CF_{1.94}(e^-)_{0.06}$). Periodic images were separated by 10.8 Å to minimize self-interactions. The positions of the atoms in the starting and ending structures were geometry optimized with the lattice fixed using the parameters described above but with a MP grid of 5×5×4 k-points. The transition state was identified using the complete linear synchronous transit/quadratic synchronous transit (LST/QST) method[6] and confirmed using the nudged elastic band (NEB) method[7] with a convergence tolerance of 1.0×10^{-5} eV/atom for energy, 0.05 eV/ Å for max

force, 0.04 GPa for max stress, and 7.5×10^{-5} Å for max displacement. Projected density of states and band-decomposed charge densities were calculated with the $Y_2CF_{1.94}(e^-)_{0.06}$ structures determined from NEB analysis using VASP[8] with PAW[9] PBE potentials and a DFT-D3[10] van der Waals correction. Calculations used an energy cut-off of both 500 eV and 600 eV in both spin-polarized and non-spin-polarized forms. Non-spin-polarized calculations were performed with a Monkhorst-Pack mesh density of 0.020 2π/Å, while spin-polarized calculations used a density of 0.025 2π/Å. All calculations used a Gaussian smearing with a width of 60 meV. The calculation used 576 bands and 713 electrons.

Calculations were converged to 1.0×10^{-7} eV/atom for energy. No residual spin density was found using spin-polarized calculations and all results were identical to non-spin polarized calculations. Projected density of states (PDOS) was performed using radii determined from Bader charge densities in $[Y_2C]^{2+}(e^-)_2$ and Y_2CF_2. The C, Y, and F radii used throughout all calculations were 1.632, 1.553, and 1.515 Å, respectively. In the case of Y_2CF_2, these radii led to oxidation states in C, Y, and F of -2.06, +1.91, and -0.88. This analysis revealed oxidation states of Y, C, and F for the $Y_2CF_{1.94}(e^-)_{0.06}$ structures. In the case of $[Y_2C]^{2+}(e^-)_2$, these radii led to oxidation states in C and Y of -2.10, +1.95, from which an electride electron density of 1.80 electrons per Y_2C was calculated. These oxidation states are identical to values reported previously.[11,12] The isosurfaces were plotted with an electron density of 0.0036 e^- per $Å^3$. To examine the electron density at compositions close to $[Y_2C]^{2+}(e^-)_2$, we used the same methods to calculate oxidation states and electron distributions using 3x3x2 supercells with a single F atom. As in the compositions close to Y_2CF_2, the oxidation states and electron distributions of the composition close to $[Y_2C]^{2+}(e^-)_2$ do not change throughout the process of electron-anion exchange.

The "thin-slab approach"[13] was used to calculate the ionization potential of bulk Y_2CF_2. For the calculations of ionization potential, a denser k-point mesh (32 × 32 × 16) was used. To prevent self-interactions between periodic images, a 12 Å vacuum space was included in the z-direction. The band gap and density of states were calculated using the HSE06 functional[14] with norm-conserving pseudopotentials[15], a cutoff energy of 850 eV, and a k-point mesh of 32 × 32 × 16. The fixed composition USPEX calculation was carried out via four serial geometry optimizations of each candidate structure. The geometry optimizations utilized the GGA PBE functional with increasing quality, where the fourth and final optimizations were converged to 5 × 10^{-5} eV/atom using a cutoff energy of 440 eV. For accurate comparison of candidate stabilities, geometry optimizations were followed by a single, higher-quality energy calculation converged to 5 × 10^{-6} eV/atom deemed sufficient to isolate reasonable Y_2CF_2 structure types. The search identified the minimum-energy structure from among ~400 candidates tested across eight generations.

2.1.2 Calculation of battery electrode characteristics

To calculate the maximum gravimetric capacity and maximum volumetric capacity, we used the following equations, where n is the number of electrons, F is Faraday's constant, MW is the molecular weight of the unintercalated host lattice, N is Avogadro's number, and V_{unit} is the volume of the host lattice unit cell:

$$max\ gravimetric\ capacity = \frac{nF}{(3600)\ MW}$$

$$max\ volumetric\ capacity = \frac{nF}{(3600)\ N\ V_{unit}}$$

Below, we write a series of chemical equations that combine to give the potential of electron insertion into Y_2CF_2 versus Li/Li^+.

$$Y_2CF_2 + 2\ Li \rightarrow [Y_2C]^{2+}(e^-)_2 + 2\ LiF \qquad \Delta G_{rxn}$$

$$2\ LiF \rightarrow 2\ {Li^+}_{solvated} + 2\ {F^-}_{solvated} \qquad \Delta G_{solv}$$

$$+ \quad 2\ {Li^+}_{solvated} + 2\ e^- \rightarrow 2\ Li \qquad E_{red}^{Li^+}$$

$$Y_2CF_2 + 2\ e^- \rightarrow [Y_2C]^{2+}(e^-)_2 + 2\ {F^-}_{solvated} \qquad E_{red}^{Y_2CF_2}$$

In a hypothetical cell with lithium, the voltage of the cell, ΔE, is the difference in potential of electron insertion into Y_2CF_2, $E_{red}^{Y_2CF_2}$, and the oxidation potential of lithium metal, $E_{ox}^{Li^+}$ (1). Through equation (2), we can relate the Gibbs free energy, ΔG, of the reduction reaction, to the voltage of the cell. The Gibbs free energy of the reaction is the sum of the Gibbs free energy of a solid-state reaction of Y_2CF_2 and lithium metal, ΔG_{rxn}, and the Gibbs free energy of the solvation of solid LiF, ΔG_{solv} (3). Substituting terms and rearranging the equation yields an equality (4) that allows us to estimate the potential of electron insertion into Y_2CF_2 vs. Li/Li^+ from values of ΔG_{rxn} and ΔG_{solv}.

$$\Delta E = E_{red}^{Y_2CF_2} - E_{ox}^{Li^+} \qquad (1)$$

$$E_{red}^{Y_2CF_2} - E_{ox}^{Li^+} = {E^{Y_2CF_2}}_{vs.\ Li/Li^+}$$

$$\Delta G = -nF(\Delta E) \qquad (2)$$

$$\Delta G = \Delta G_{rxn} + \Delta G_{solv} \qquad (3)$$

$${E^{Y_2CF_2}}_{vs.\ Li/Li^+} = \frac{\Delta G_{rxn} + \Delta G_{solv}}{-nF} \qquad (4)$$

We approximated ΔG_{rxn} by neglecting the change in entropy of the solid reaction and calculating the enthalpy using DFT, affording a value of -209.3 kJ/mol. To estimate ΔG_{solv},

we used an experimental value of the energy of solvation of LiF (21.13 kJ/mol) in the ionic liquid, 1-butyl-3-methylimidazolium trifluoromethanesulfonate ([C4C1im][OTf]).[16] It is worthwhile to understand the sources of error and relative accuracy of this estimate. We performed four DFT calculations, each of which may contain an error of 1-2 kJ/mol, adding an error of ~4 kJ/mol. We neglected the change in the entropy of the solids. The sum of these terms at 300 K, each with a value of around 10 kJ/mol, likely gives an error of ~2 kJ/mol. Rather than [C4C1im][OTf], our experiments employed a different solvent, an ionic liquid consisting of N,N,N-trimethyl-N-neopentylammonium fluoride and bis(2,2,2-trifluoroethyl) ether, which has a higher free energy of solvation for F^-.[17] The error associated with this term could be as large as 20 kJ/mol. Together these errors, ~26 kJ/mol, suggest a liberal estimate of 14% error. Therefore, the potential of electron insertion into Y_2CF_2 is +0.97 ± 0.13 V vs. Li/Li^+.

We calculated the cell voltage for a battery using $[Y_2C]^{2+}(e^-)_2/Y_2CF_2$ as the anode and Cu/CuF_2 as the cathode using the equation:

$$[Y_2C]^{2+}(e^-)_2 + CuF_2 \rightarrow Y_2CF_2 + Cu$$

The enthalpy of Cu was calculated using GGA while the enthalpy of CuF_2 was calculating GGA + U (U = 4.0 eV) so the ΔG was corrected according to the procedure developed by Jain et al.[18] Following the procedure described above, we calculated the reduction potential of CuF_2 to be ~3.7 V vs. Li/Li^+ consistent with reported results.[17]

2.2 Characterization methods

2.2.1 Powder X-ray diffraction

A Rigaku SmartLab automated multi-purpose X-ray diffractometer with high flux PhotonMax photon source and HyPix-3000 high energy resolution 2D hybrid pixel array detector (HPAD) was utilized for all powder X-ray diffraction experiments. A Cu Kα X-ray source was utilized with a wavelength of 1.54 Å, and the Cu Kβ lines were filtered out with nickel foil.

Samples were analyzed in a Bragg-Brentano geometry on a quartz slide with a 20 mm x 20 mm square indented by 0.2 mm to contain a thin layer of the powdered materials. Air-sensitive samples were encapsulated with 1 Mil Kapton tape with an added 20 mm x 20 mm 1 Mil Kapton film as a barrier between the sample and tape. While Kapton displays significant X-ray attenuation at low angles ($2\Theta < 25^{o}$), the diffraction background can be fitted well at angles $2\Theta > 25^{o}$. Diffraction patterns were subjected to Rietveld refinement using the Rigaku PDXL software.

2.2.2 Electron microscopy

Samples were imaged using a Hitachi S-4700 cold cathode field emission SEM at an accelerating voltage of 2 kV with an Oxford energy-dispersive X-ray spectroscopy (EDS) detector. An accelerating voltage of 20 kV was used for EDS measurements. Samples were loaded onto the SEM sample holders in the glovebox and transported to the instrument under inert atmosphere; however, the samples were exposed to air for a few seconds during the transfer into the air lock of the instrument.

Transmission electron microscopy (TEM) and energy dispersive X-ray spectroscopy (EDS) were performed using a Thermo Scientific Talos F200X electron microscope with an accelerating voltage of 200 kV. Electrode film samples were first scraped into a vial and washed

with acetonitrile 3x to remove excess F-electrolyte salt. Once most of the acetonitrile was decanted, the powder was suspended in diethyl carbonate by bath sonication for 1 hr, resulting in a light gray solution. Diethyl carbonate was used because of its ability to decouple the PVDF binder from the active material particles, suspend Y_2C particles sufficiently, and dry from TEM grids fairly quickly under vacuum (BP = 125°C). 3 μL of the suspension was pipetted onto a 300 mesh Cu TEM grid, containing a lacey carbon to capture film particles, then dried under vacuum in a glovebox antechamber for 30 minutes. Grids were then loaded onto the TEM grid holder and transported to the instrument in a sealed plastic bag under argon to minimize air exposure. The holder was quickly transferred into the instrument and analysis subsequently conducted.

2.2.4 X-ray photoelectron spectroscopy

Samples were characterized by X-ray photoemission spectroscopy (XPS) using a Kratos Axis Ultra Delay-Line Detector spectrometer with a monochromatic Al K α source. For these measurements, the powder was pressed into indium substrates in an argon-filled glovebox, then encapsulated in a sealed glass holder and loaded under inert gas into the XPS vacuum chamber. High resolution XPS data were collected at a pass energy of 20 eV, and a charge neutralizer was used for charge compensation. All data were corrected to the C 1s peak at 284.6 eV.

2.2.5 Ultraviolet-visible spectroscopy

UV-vis spectroscopy was performed in a transmission geometry through thin (~ 0.5 mm thick) discs made of mixtures of Y_2CF_2 and KBr. The Y_2CF_2 powder was diluted with spectroscopic grade KBr, ground finely in a ball mill until homogeneous, and then pressed into discs using a hydraulic press. The background due to scattering from KBr was subtracted by pressing films of KBr of varying thicknesses to estimate its effective attenuation as a function of thickness and subtracting a weighted fraction from the acquired spectra. The spectra were

collected using a Cary 5000 UV-vis spectrometer with the DRA-2500 internal integrating sphere accessory. The reflection spectra of Y_2CF_2 particles from 400 - 850 nm were obtained using a Craic UV-vis-NIR microspectrophotometer with a polychromatic Xe source and an EC Epiplan Neofluar LD objective with an N.A. of 0.55. The aperture size was 14.7 × 14.7 μm except where noted.

2.3 Synthesis of materials

2.3.1 Custom arc-melting apparatus

An electric arc-melter was used to synthesize Y_2C materials and seal reagents in inert metal containers. The apparatus was purchased from Centorr Vacuum Industries and is a Single Arc Furnace (5SA Series) with 300 A DC power supply and water-cooled power cables to actively cool the system. A gas input line and vacuum output allow the chamber to be evacuated and purged with argon to ensure inert atmosphere for welding. All welding was performed under positive pressure of argon (2 psig) to ensure adequate shielding of the electric arc and protection of starting materials from air.

A variety of copper hearths can be inserted into the arc-welding chamber to accommodate multiple welding geometries. For direct melting of reagents, a hearth with a bowl-shaped bottom was selected. In order to seal reagents in inert metal ampules, however, a custom hearth was designed to hold metal tubes with 1 cm diameter. A depiction of this custom hearth is shown below in Figure 2.1.

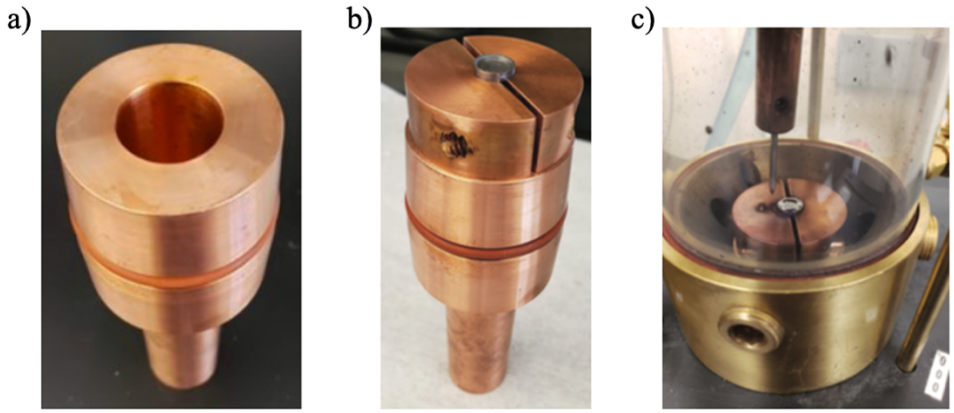


Figure 2.1: Arc-melting setup for welding tantalum tubes. a) Copper hearth with hollowed center for holding the b) Copper clamp, held together with brass screws, which grips a 5 cm tantalum tube with tantalum cap. c) The custom copper hearth with clamped tantalum tube and cap ready for sealing by arc melting

The custom hearth is comprised of a hollowed cylinder within a solid, machined copper holder to which a copper clamp is inserted. The clamp is used to suspend metal tubes of lengths 5-10 cm that contain metal caps hammered into them, thereby allowing for electric arc sealing of the cap to tube interface. The metal tubes used in this work are made from tantalum metal (99.95% Ta seamless tubing, 1 cm OD, Eagle Alloys) and cut to 5 cm lengths. The caps were made of the same Ta. A low amperage (~50 A) and fast melting of the Ta cap/tube interface in a circular motion is required to prevent over-heating, which can result in destruction of the interface and collapse of the Ta cap. Furthermore, the tubing should be suspended by the copper clamp such that there is ~0.5 cm of tubing exposed, maximizing the cooling of the sealed interface. Proper sealing of ½ tubes was verified by addition of a low surface tension solvent, such as acetone, to observe whether there was leakage. Metal tubes were then sealed in quartz tubing under 1 atm argon with a hydrogen-oxygen torch to prevent oxidation of the metal at high temperatures.

2.3.2 Synthesis of layered and cubic Y_2C

The synthesis of layered ($R\bar{3}m$) Y_2C has been well-reported in the literature.[11,19] A large yttrium chunk (99.9%, Sigma-Aldrich, 262994-5G) was melted into a button via arc melting at 100 Amps under argon flow, then flipped and re-melted. Pre-melting the yttrium is a necessary precaution because of the material's propensity for ablating in the arc-melting chamber, thereby altering the available mass of yttrium for the reaction. Given the small molecular weight of carbon and narrow stoichiometric range for layered ($R\bar{3}m$) Y_2C formation, the accuracy in the mass of reagents is critical.

The yttrium button was weighed again in the glovebox, then a carbon pellet with a mass corresponding to a stoichiometry of $Y_2C_{0.95}$ was pressed from graphite flakes (Sigma-Aldrich, ~100 mesh flakes, 99.9%, 808091-2.5KG) in a 6-mm pellet die. A deficiency of carbon is necessary for favoring the layered ($R\bar{3}m$) phase of Y_2C over the cubic ($Fm\bar{3}m$) phase (REF). The yttrium button and carbon pellet were carefully placed into the well of a water-cooled arc-melting copper hearth and melted under 100 Amps of current. The reaction between yttrium and carbon is indicated by an increased brightness of the arc due to a violent release of heat from the exothermic reaction. Once melted throughout, the pellet was flipped and melted again for 10 iterations to ensure homogeneity of the product. The final appearance of the product was a silvery button with high reflectance and increased hardness. The button could be crushed in a die with a chisel, then hand ground using a mortar and pestle. The ground powder was dark gray in color. To reduce particle size, the powder was subjected to 15 min of ball-milling in a SPEX 8000D Mixer/Mill with a stainless-steel ball in a ~2 mL stainless steel container. The cubic $Fm\bar{3}m$ phase of Y_2C can be produced via the same methodology, except with a carbon excess to

$Y_2C_{0.95}$. The excess carbon allows carbon occupation in interlayer sites to become favorable, thereby resulting in a disordered rock-salt structure.

2.3.3 Synthesis of Y_2CF_2

The synthesis of Y_2CF_2 is well described by Druffel, et. al.[12] Y_2CF_2 was synthesized by the solid-state reaction of YF_3 (Sigma-Aldrich, granules, < 0.2% oxygen, 769525-25G) with Y metal (Alfa Aesar, ~40 mesh powder, 99.6%, 44147-06) and graphite (Sigma-Aldrich, ~100 mesh flakes, 99.9%, 808091-2.5KG). The reagents were ground into a fine powder in a stoichiometric ratio and pressed into a pellet under ~0.56 GPa of pressure using a hydraulic press. The pellet was welded inside an ampoule made of tantalum metal using a custom hearth under ~50 A of current and Ar flow. The tantalum ampoule was then sealed in a fused quartz tube under ~1 atm Ar and placed in a Lindberg Blue M tube furnace. The vessel was subjected to 1240ºC over 3 days, and was cooled to room temperature over a total of 20 hrs. The quartz tube deforms around the tantalum tube and turns opaque since the glass transition temperature of quartz (~1200ºC) is comparable to the reaction temperature. The ampoule was then opened in an argon-filled glovebox and the metal tube opened with a pipe cutter. The pellet consisted of vibrant green crystals with high reflectance, turning a dark red color when the pellet was ground in a mortar and pestle. Druffel, et. al. attributed this color change to the disruption of reflective surfaces, which have peak reflectance at 540 nm (green), revealing a red color originating from absorption at the band gap (775 nm). All materials were stored in a glovebox with an argon atmosphere (oxygen < 0.01 ppm), and all synthetic steps were carried out under an argon atmosphere. The particle size of Y_2CF_2 powder was reduced in the same manner as employed for the Y_2C powder described above.

2.3.4 Y_2CF_2 + Na or K vapor reactions

Ground Y_2CF_2 powder (~150 mg) was encapsulated in a tantalum pocket and sealed under vacuum in a fused quartz tube with Na or K metal (300 – 400 mg) on the other end of the tube, separated by quartz wool. An excess of 5-10x Na or K was used to ensure ample reagent. Sealed quartz tubes were subjected to temperatures of 200 – 300°C in a tube furnace, where the vapor pressure of Na and K are > 10^{-2} mbar, allowing for slow reaction of the alkali metal vapor with the Y_2CF_2 powder. Vaporization of each metal was verified by the darkening of the quartz tube over the course of the reaction, a result of the reaction between Na or K with the SiO_2 quartz. Quartz tubes were then opened in an argon-filled glovebox and the powder analyzed by X-ray diffraction.

2.3.5 Y_2CF_2 + Li reactions

Lithium granules (50-100 mg, Sigma Aldrich, 499811-25G) were melted in a Ta boat produced from Ta foil (~500 mg) at a setting of 350°C on a hot plate in an argon-filled glovebox. Tantalum foil was utilized due to its low reactivity and absence of stable alloys with lithium metal. Once softened, the lithium pellets were mechanically kneaded into a uniform globule, which had a high surface tension on the Ta surface.

Y_2CF_2 powder was slowly incorporated into the molten Li by folding the powder into the globule with a stainless-steel spatula. Initially, the powder did not mix well with the molten Li. However, after ~10 minutes of stirring, the surface tension quickly dropped, and a pool of silvery lithium with a solid floating on the surface was produced. The liquid pool was blended for an additional 30 minutes to ensure thorough incorporation of the Y_2CF_2 powder. Once finished stirring, the lithium mixture was left to cool to a solid, then cut into desired shapes for subsequent characterization. The product appeared as a solid silvery matrix with a white-coated

surface layer. A 20 x 20 mm square of the foil was cut and placed onto a glass slide under Kapton tape for X-ray diffraction measurements. The lithium product was scraped off the surface carefully with a fine blade for X-ray absorption measurements. All materials were handled in an argon glovebox.

2.4 Electrochemical methods

2.4.1 Slurry preparation and casting

The preparation of electrodes of Y_2C or Y_2CF_2 largely mirrors procedures used for Li-ion materials.[20] Each ball-milled active material was blended with Super P carbon black (99%, Alfa Aesar, H30253-14) in a mortar then transferred slowly into a solution of poly(vinylidene fluoride) (avg. 180,000 g/mol by GPC, Sigma-Aldrich, 427152-100G) in propylene carbonate (99.7%, anhydrous, Sigma-Aldrich, 310328-100ML) such that the mass ratio of active material/binder/Super P was 80/10/10 wt% and the slurry solution contained 40 wt% solids in liquid. Traditionally, N-methylpyrrolidone (NMP) is used as the dispersing solvent in Li-ion electrode slurries. However, the highly reactive electride Y_2C is unstable in NMP, so a solvent with similar properties, propylene carbonate, was used instead. The masses used were 100 mg of active material, 12 mg of Super P, 12 mg of PVDF, and 170 uL propylene carbonate. After ~10 minutes of blending the slurry mechanically in the mortar, the thick, black ink was cast onto tantalum foil, as described below.

2.4.2 Film casting and drying

Slurries were cast onto 3 cm x 7 cm tantalum foil strips (0.25 mm, > 99.9%, Sigma-Aldrich, 262897-100CM2), held onto a glovebox bed with 4 Mil-thick pieces of Scotch tape, until the slurry covered most of the available area. A glass pipet was used to doctor blade the slurry uniformly across the Ta substrate, then the foil was taken up from the glovebox floor and

placed in the vacuum antechamber to dry at 120°C overnight. The temperature in the chamber was slowly ramped to 120°C over 2 hours to ensure slow evaporation of the propylene carbonate. Long heating times are required to ensure complete solvent removal and homogeneous distribution of particles in the film matrix.[21] Once the film was dry, 19 mm disks of the films were cut using a compact precision disk cutter (MTI Corp., MSK-T-07) and used soon after preparation.

2.4.3 Synthesis of the liquid fluoride-ion electrolyte

The synthesis of the fluoride-ion electrolyte salt, N,N,N-trimethylammonium-N-neopentylammonium fluoride (Np_1Me_3F) is described by Davis, et. al.[17] and is largely followed in this procedure. The first step was to make neopentyltrimethylammonium iodide, then perform a series of ion exchange reactions from I^- to OH^- then F^-. First, potassium carbonate was added to a 1 L Erlenmeyer flask containing a solution of methyl iodide and neopentylamine under magnetic stirring in 100% ethanol for 24 hours at room temperature. The resulting white solid was filtered out after washing with dichloromethane and drying under vacuum, then recrystallized from isopropanol. The solid was confirmed to be neopentyltrimethylammonium iodide by ^1H NMR. Silver oxide was added to a solution of the neopentyltrimethylammonium iodide in DI water, then filtered and added directly to an HF solution such that all of the HF was utilized. The solution was dried under vacuum to remove the water, then washed with isopropanol and dried to produce a white solid, confirmed to be N,N,N-trimethylammonium-N-neopentylammonium fluoride by ^1H NMR.

2.4.4 Custom 3-electrode electrochemical coin cell

An electrochemical cell was designed to allow for 3-electrode half-cell testing of 19 mm electrode disks with ease of assembly and cleaning, aspects that are not present with traditional

coin cells. The cell was designed such that electrode disks are compressed against two faces of a hollowed Teflon block with a vice grip, and a port on the top of the block allows for addition of the liquid electrolyte and the reference electrode (Figure 2.2). To fabricate the cell, a ½" OD cylindrical hole was drilled through the square face of a 1½" width x 1½" height x 1" depth piece of Teflon, then a ¼" hole was drilled through the top rectangular face of the cell as the top port. Each square face contained a 1/32" deep ring cut into the Teflon with an outer diameter of 3/4" and inner diameter of 5/8" to allow for insertion of an o-ring as a junction between the Teflon cell and electrode films. Since Viton reacts and swells within the F-electrolyte, chemically resistant Kalrez o-rings were used instead (Dash number 016, McMaster, 9568K22). 19 mm disk electrodes were compressed onto the o-rings using 1" x 1¼" x 1 mm highly conductive copper plates, where ¼" of the edge was bent by 90° to allow for clipping of the electrical wiring, and a hand-held vice grip. Once the electrodes were fastened to the Teflon cell, F-electrolyte could be added through the top port then reference electrode placed within.

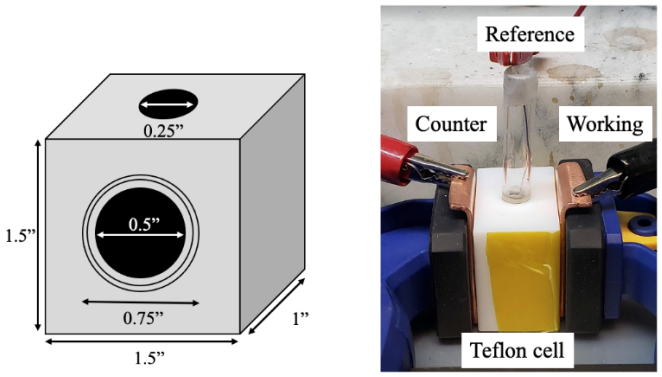


Figure 2.2: Liquid electrochemical cell for fluoride-ion disk electrode testing. Custom Teflon 3-port 19 mm disk electrode electrochemical cell where disks are compressed onto the sides of a Teflon base with Kalrez o-rings by copper plates and a vice grip. The electrolyte and a reference electrode can be inserted through the top 0.25" diameter port and wiring attached to the copper plates.

2.4.5 Reference and counter electrodes

An 81 mm long, 6 mm diameter glass tube with a 2.6 mm CoralPor frit attached to a 3 mm tapered neck via PTFE heat shrink tubing was used as a Ag/Ag^{+}-based reference electrode compartment (Bio-logic, A-012171). The reference electrolyte was composed of 0.01 M silver trifluoromethanesulfonate (> 99%, Sigma-Aldrich, 176435-25G) in 1-methyl-1-propylpyrrolidinium bis(trifluoromethanesulfonyl)imide (> 98%, TCI Chemicals, M2098) with a silver wire (0.5 mm, 99.9%, Sigma-Aldrich, 327026-4G) suspended in the ionic liquid via parafilm. The Ag-based ionic liquid is sensitive to ambient light, so must be wrapped in Al foil when not in use. After addition of ionic liquid to the glass compartment, reference electrodes were left to sit overnight so that the glass frit became properly wetted. The counter electrode was a 19 mm disk of platinum foil (0.025 mm thickness, 99.9%, Sigma-Aldrich, 267244-350MG), cut using a compact precision disk cutter (MTI Corp., MSK-T-07).

2.4.6 Electrochemical testing methods

All electrochemistry was carried out in an argon-filled glovebox with a Bio-logic SP-150 Potentiostat. Electrically shielded cables were fed through a glovebox port to allow for connection of electrochemical cells in the glovebox to the potentiostat outside of the box. Once electrochemical cells were assembled and attached to the external circuit, the potentiostat was programmed to track the open circuit potential to capture voltage drift. Drifting over time indicates that the cell has not reached an equilibrium and may need to sit until it is stable. If the cell continues to drift, it may indicate that the reference electrode is leaking or the surface of electrodes is changing significantly. Once the fluctuation in open circuit potential was $\pm$ 50 mV, galvanostatic charging or discharging was employed. Charge and discharge cycles were performed by applying +150 μA or -150 μA of current, respectively, to the working electrode

and measuring the voltage output over time. After the electrochemical sequence was complete, the electrolyte was carefully removed from the cell and electrodes washed with BTFE to remove excess F-electrolyte salt. Thereafter, electrodes were either placed directly onto quartz slides for XRD analysis or the film scraped off into a vial for TEM or XPS measurements.

The conductivity of the fluoride-ion electrolyte was evaluated by performing electrochemical impedance spectroscopy on a Pt | Np_1F/BTFE | Ta cell without a reference electrode. An oscillating potential of $\pm$ 10 mV was applied to the Ta working electrode and the current output was measured from frequencies of 100 kHz to 1 Hz. Nyquist plots of the impedance were analyzed using the Bio-logic software with the circuit fitting tool.

REFERENCES

(1) Clark, S. J.; Segall, M. D.; Pickard, C. J.; Hasnip, P. J.; Probert, M. I. J.; Refson, K.; Payne, M. C. First principles methods using CASTEP. *Z. Kristallogr. Cryst. Mater.* **2005**, *220* (5/6).

(2) Vanderbilt, D. Soft self-consistent pseudopotentials in a generalized eigenvalue formalism. *Phys. Rev. B* **1990**, *41* (11), 7892–7895.

(3) Perdew, J. P.; Ruzsinszky, A.; Csonka, G. I.; Vydrov, O. A.; Scuseria, G. E.; Constantin, L. A.; Zhou, X.; Burke, K. Restoring the density-gradient expansion for exchange in solids and surfaces. *Phys. Rev. Lett.* **2008**, *100* (13), 136406.

(4) Tkatchenko, A.; Scheffler, M. Accurate molecular van der Waals interactions from ground-state electron density and free-atom reference data. *Phys. Rev. Lett.* **2009**, *102* (7), 073005.

(5) Monkhorst, H. J.; Pack, J. D. Special points for Brillouin-zone integrations. *Phys. Rev. B* **1976**, *13* (12), 5188–5192.

(6) Govind, N.; Petersen, M.; Fitzgerald, G.; King-Smith, D.; Andzelm, J. A generalized synchronous transit method for transition state location. *Comp. Mater. Sci.* **2003**, *28* (2), 250–258.

(7) Classical and Quantum Dynamics in Condensed Phase Simulations https://www.worldscientific.com/worldscibooks/10.1142/3816 (accessed Mar 21, 2021).

(8) Kresse, G.; Hafner, J. *Ab initio* molecular dynamics for liquid metals. *Phys. Rev. B* **1993**, *47* (1), 558–561.

(9) Kresse, G.; Joubert, D. From ultrasoft pseudopotentials to the projector augmented-wave method. *Phys. Rev. B* **1999**, *59* (3), 1758–1775.

(10) Grimme, S.; Antony, J.; Ehrlich, S.; Krieg, H. A consistent and accurate ab initio parametrization of density functional dispersion correction (DFT-D) for the 94 elements H-Pu. *J. Chem. Phys.* **2010**, *132* (15), 154104.

(11) Zhang, X.; Xiao, Z.; Lei, H.; Toda, Y.; Matsuishi, S.; Kamiya, T.; Ueda, S.; Hosono, H. Two-Dimensional Transition-Metal Electride Y_2C. *Chem. Mater.* **2014**, *26* (22), 6638–6643.

(12) Druffel, D. L.; Lanetti, M. G.; Sundberg, J. D.; Pawlik, J. T.; Stark, M. S.; Donley, C. L.; McRae, L. M.; Scott, K. M.; Warren, S. C. Synthesis and Electronic Structure of a 3D Crystalline Stack of MXene-Like Sheets. *Chem. Mater.* **2019**, *31* (23), 9788–9796.

(13) Fall, C. J.; Binggeli, N.; Baldereschi, A. Deriving accurate work functions from thin-slab calculations. *J. Phys.: Condens. Matter* **1999**, *11* (13), 2689–2696.

(14) Heyd, J.; Scuseria, G. E. Assessment and validation of a screened Coulomb hybrid density functional. *J. Chem. Phys.* **2004**, *120* (16), 7274–7280.

(15) Hamann, D. R.; Schlüter, M.; Chiang, C. Norm-Conserving Pseudopotentials. *Phys. Rev. Lett.* **1979**, *43* (20), 1494–1497.

(16) Kuzmina, O.; Bordes, E.; Schmauck, J.; Hunt, P. A.; Hallett, J. P.; Welton, T. Solubility of alkali metal halides in the ionic liquid [C4C1im][OTf]. *Phys. Chem. Chem. Phys.* **2016**, *18* (24), 16161–16168.

(17) Davis, V. K.; Bates, C. M.; Omichi, K.; Savoie, B. M.; Momčilović, N.; Xu, Q.; Wolf, W. J.; Webb, M. A.; Billings, K. J.; Chou, N. H.; et al. Room-temperature cycling of metal fluoride electrodes: Liquid electrolytes for high-energy fluoride ion cells. *Science* **2018**, *362* (6419), 1144–1148.

(18) Jain, A.; Hautier, G.; Ong, S. P.; Moore, C. J.; Fischer, C. C.; Persson, K. A.; Ceder, G. Formation enthalpies by mixing GGA and GGAcalculations. *Phys. Rev. B* **2011**, *84* (4), 045115.

(19) Otani, S.; Hirata, K.; Adachi, Y.; Ohashi, N. Floating zone growth and magnetic properties of Y_2C two-dimensional electride. *J. Cryst. Growth* **2016**, *454*, 15–18.

(20) Kraytsberg, A.; Ein-Eli, Y. Conveying Advanced Li-ion Battery Materials into Practice The Impact of Electrode Slurry Preparation Skills. *Adv. Energy Mater.* **2016**, *6* (21), 1600655.

(21) Baunach, M.; Jaiser, S.; Schmelzle, S.; Nirschl, H.; Scharfer, P.; Schabel, W. Delamination behavior of lithium-ion battery anodes: Influence of drying temperature during electrode processing. *Drying Technology* **2016**, *34* (4), 462–473.

CHAPTER 3: FIRST-PRINCIPLES PREDICTION OF ELECTRONCHEMICAL ELECTRON-ANION EXCHANGE[1]

Daniel L. Druffel,[†,*] Jacob T. Pawlik,[†,*] Jack D. Sundberg,[†] Lauren M. McRae,[†] Matthew G. Lanetti,[†] and Scott C. Warren[†,‡]

† Department of Chemistry, University of North Carolina at Chapel Hill, Chapel Hill, North Carolina 27599, United States

‡ Department of Applied Physical Sciences, University of North Carolina at Chapel Hill, Chapel Hill, North Carolina 27599, United States

* These authors contributed equally to this work

3.1 Introduction

An elementary concept of chemistry is that the gain or loss of electrons in a material must be accompanied by the reduction or oxidation of its atoms. Here, we describe an exception to this concept. Some crystalline solids, called electrides, contain lattice sites occupied by a bare electron.[2,3] These electrons are called "anionic electrons " because they have a charge and size similar to those of simple anions. The striking parallel between anionic electrons and anions was demonstrated when electrides were reacted with metal halides, producing crystals in which the halide replaced the electride electron with minimal change to the crystal lattice.[4] Despite these findings, the reversible insertion or removal of anions is little explored, perhaps because anion

[1] Reproduced with permission from (Druffel, D. L.; Pawlik, J. T.; Sundberg, J. D.; McRae, L. M.; Lanetti, M. G.; Warren, S. C. First-Principles Prediction of Electrochemical Electron-Anion Exchange: Ion Insertion without Redox. J. Phys. Chem. Lett. 2020, 9210–9214. https://doi.org/10.1021/acs.jpclett.0c02266) Copyright 2020 American Chemical Society.

movement typically involves high activation energies. In the following, however, we demonstrate using first-principles methods that anions and electrons can be exchanged at room temperature reversibly under electrochemical control (Figure 3.1a,b), where the electrode material gains and loses electrons without oxidation or reduction of its atoms.

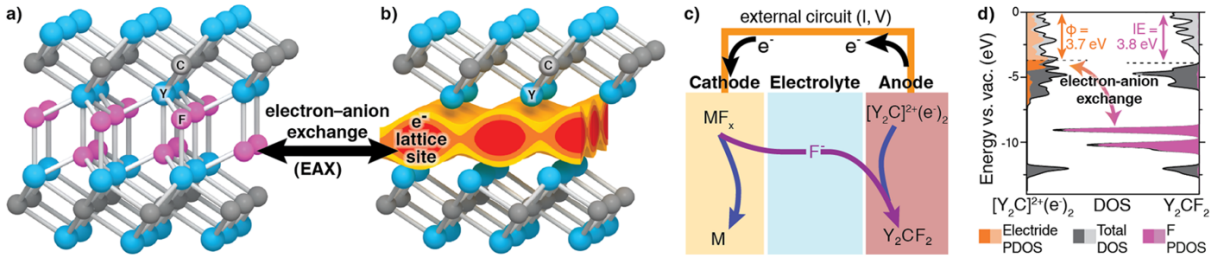


Figure 3.1: Concept of electron-anion exchange. The reversible conversion of (a) Y_2CF_2 to (b) $[Y_2C]^{2+}(e^-)_2$ under an applied bias where yellow, orange, and red show isosurfaces of the anionic electrons at the Fermi level. (c) Battery configuration incorporating $[Y_2C]^{2+}(e^-)_2$ as an anode, a F^- electrolyte, and a cathode (e.g., a metal fluoride). (d) Effect of electron-anion exchange on the partial density of states in the Y_2C system, where IE is the ionization energy and Φ is the work function.

A natural application of electron−anion exchange (EAX) is in batteries (Figure 3.1c). While rapid progress in batteries that shuttle cations between electrodes has led to their widespread use[5], batteries that shuttle anions remain largely unexplored. Despite previous efforts[6,7], one deficiency in the science of intercalating anions is the absence of reversible high-capacity electrodes. Here, we show that EAX could enable a broad class of high-capacity electrodes for anion shuttle batteries.

In a general sense, exchanging an anion, such as fluoride, for an electride electron stabilizes the material system because the energetic electride electron shifts onto a lower-lying band comprised of fluorine p-orbitals (Figure 3.1d). This provides a favorable driving force for a

reaction with a fluoride of a less electropositive metal (e.g., Cu) that could act as a cathode in a F−battery. For example, the large free energy of the reaction $[Y_2C]^{2+}(e^-)_2 + CuF_2 \rightarrow Y_2CF_2 + Cu$ suggests a possible cell voltage of 2.8 V. To provide a fundamental grounding for EAX, we present computational results that address the oxidation states of the atoms, the mechanism of anion diffusion, and the structural changes that result.

3.2 Results

3.2.1 Density-functional theory calculations of EAX

We began by examining the electrides $[Ca_2N]^+e^-$ and $[Sr_2N]^+e^-$, which have positively charged layers of atoms that alternate with negatively charged layers of electrons. We found that fluoride intercalation and chloride intercalation were not reversible at room temperature because the corresponding halides are wide band gap insulators with poor ionic mobility. We sought out an isostructural electride, $[Y_2C]^{2+}(e^-)_2$, because our calculations and experiments indicated that the corresponding fluoride, Y_2CF_2, has a small band gap and high electronic mobility. We expected F^- to intercalate reversibly into the $[Y_2C]^{2+}(e^-)_2$ lattice as the e^- moves into an external circuit according to the half-reaction:

$$[Y_2C]^{2+}(e^-)_2 + 2F^- \rightarrow [Y_2C]^{2+}(F^-)_2 + 2e^-$$

For EAX to occur at room temperature, the anionic electron and F^- need to diffuse rapidly through the crystal. To assess F^- movement in the Y_2C system, we modeled a supercell of Y_2CF_2 and removed a fluorine atom, naturally introducing an anionic electron in its place (Figure 3.2b). Using density functional theory (DFT) and the nudged elastic band (NEB) method, we calculated a remarkably low activation barrier for electron−fluoride exchange (and thus F−diffusion) in Y_2CF_2 of only 196 meV (Figure 3.2a which is even lower than the barrier for Li^+ diffusion in both $LiCoO_2$ (~300 meV)[8] and graphite (~260 meV).[9] Our calculations reveal that

the lowest-energy pathway for F−diffusion in Y_2CF_2 is hopping of F−directly between tetrahedral sites (Figure 3.2b-d), a distance of only 2.44 Å. Because the entire two-dimensional (2D) network of sites can be accessed by hopping exclusively through tetrahedral sites, we expect that this is the dominant mechanism of F−diffusion in the layered Y_2C system and that F−diffusion is rapid at room temperature.

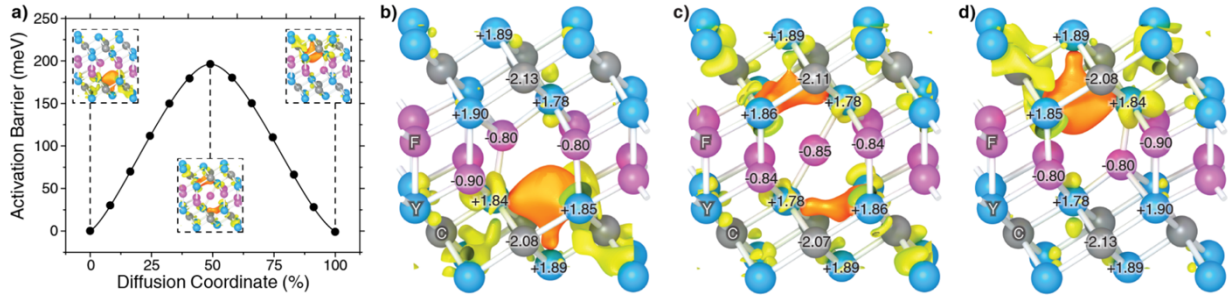


Figure 3.2: Mechanism of electron−anion exchange. (a) Activation barrier for the diffusion of F^- in Y_2CF_2 calculated using the NEB method. (b) Electron density isosurfaces near the Fermi level. The ground state of Y_2CF_2 with one F vacancy showing a F^- (purple) and an anionic electron (orange) at tetrahedral sites prior to exchange. The oxidation states are overlaid on the individual atoms, including Y (blue) and carbon (gray). (c) Transition state during electron−anion exchange. (d) Ground state after the exchange. All e^- densities are plotted at a value of 0.0036 $e^-/Å^3$

To understand the extent of redox chemistry in electrochemical electron-anion exchange, we calculated the oxidation states of the atoms in the host lattice (Table 3.1, Figure 3.3). We find that the oxidation states of Y (1.91+) and C (2.06−) in Y_2CF_2 are nearly identical to those in $[Y_2C]^{2+}(e^-)_2$ (1.95+ and 2.10−, respectively)[10] and also agree with our experimental X-ray photoelectron spectroscopy measurements on Y_2CF_2 that identify a 2+ oxidation state for Y.[11] Thus, in contrast to traditional ion insertion chemistry, in which the oxidation state of a transition

metal changes, the net result of EAX is that the atoms in the host lattice are neither reduced nor oxidized.

Table 3.1: Oxidation states in Y_2C and Y_2CF_2. Charges on the consituent atoms in the Y_2C system for $[Y_2C]^{2+}(e^-)_2$ taken from literature, Y_2CF_2 calculated using Bader charge analysis, Y_2CF_2 calculated using WS-LDOS charge analysis, and F−deficient Y_2CF_2 in its ground-state (GS) and its transition state (TS, with F^- halfway between tetrahedral sites) calculated using PDOS charge analysis. The oxidation states for the F^- deficient Y_2CF_2 are reported as an average and with the atoms nearest to the electron-anion exchange ("proximal").

Atoms	Charges						
	$[Y_2C]^{2+}(e^-)_2$ PDOS	Y_2CF_2 Bader	Y_2CF_2 PDOS	$Y_2CF_{1.94}(e^-)_{0.06}$ GS PDOS		$Y_2CF_{1.94}(e^-)_{0.06}$ TS PDOS	
				Average	Proximal	Average	Proximal
Y	+1.94	+1.91	+1.95	+1.87	+1.77	+1.89	+1.79
C	-2.04	-2.14	-2.10	-2.11	-2.07	-2.12	-2.07
e/F	-0.91	-0.85	-0.88	-0.88	-0.80	-0.88	-0.85

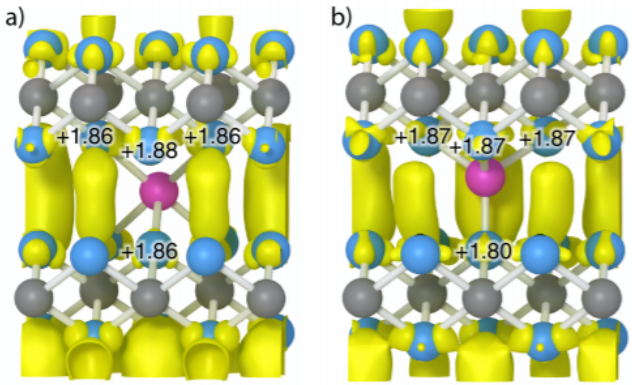


Figure 3.3: Electron density in Y_2C with a single F atom. Electron density isosurfaces at the Fermi level (± 0.1 eV vs. E_f) for a single F atom in a 5×5×1 supercell of Y_2C. a) Ground state of F in Y_2C, showing F in an octahedral coordination geometry. b) Transition state of F in Y_2C, showing F in a tetrahedral coordination geometry. The largest change in oxidation state of the surrounding Y atoms is 0.086. Isosurfaces are plotted with an electron density of 0.015 $e^-/Å^3$.

Though we determined that EAX results in no reduction or oxidation overall, the fundamental question of whether the elemental step of anion hopping involves transient redox processes in the host lattice remains. To answer this question, we calculated the electron density as the F^- hops along the NEB path, exchanging sites with an anionic electron (Figure 3.3b-d). We find that the position of the anionic electron differs subtly from the position of the F^- site (Figure 3.3b,d), but the electron density in that site still integrates to 0.8 e^- (Table 3.1). At the transition state, with F^- halfway between sites, the anionic electron simultaneously occupies both its initial site and its final site (Figure 3.3c). This behavior demonstrates an exciting result: while the anionic electron behaves in many ways like a traditional anion, it can still tunnel in a way common to electrons.

We also note that even as the oxidation states remain unchanged (Table 3.1), the valence electrons of nearby atoms polarize slightly (Figure 3.4). These plots show the change in electron density between the ground state and transition state with red (blue) showing areas that gain (lose) electron density. Individual atoms that surround the moving fluoride gain electron density on one side of the atom but lose electron density on the other, thus leading to a small polarization of the surrounding environment with negligible changes in oxidation state. In addition, bond lengths in the immediate vicinity of the fluoride change by < 0.03 Å, which further highlights how the electron transfer process that occurs in EAX is fundamentally different from ordinary redox processes, which can induce large changes in bond length.

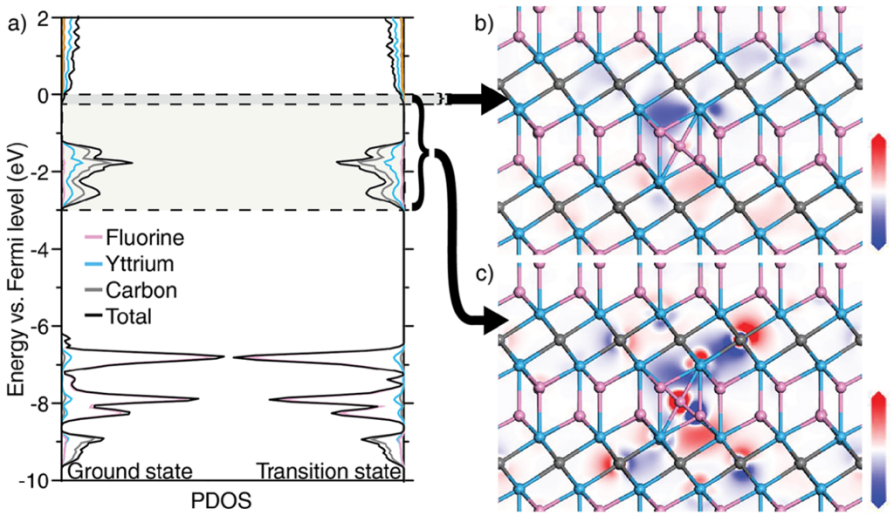


Figure 3.4: Polarization of valence electrons at and near the Fermi level. (a) Partial density of states for the ground and transition states during electron−anion exchange in Y_2CF_2. (b) Electron density deformation plots projected onto a 2D slice along the (110) direction cutting through the anionic electron and hopping F^-. These show the difference in electron density between the transition state and ground state for (b) the highest filled bands that comprise the anionic electron and (c) the valence bands comprised of the anionic electron, Y, C, and F orbitals, within 2.5 eV of the Fermi level. The scale bars for panels b and c are, from blue to red, 0.01 to 0.01 and −0.035 to 0.035 $e^-/Å^3$, respectively.

More broadly, the observations about EAX highlight similarities to the concept of proton-coupled electron transfer (PCET)[12] in which the movement of a proton is coupled to the movement of an electron. Here, our calculations show that anion movement occurs simultaneously with electron movement. We therefore introduce the term anion-coupled electron transfer (ACET) to describe the fundamental step of EAX. In the ACET observed in (Figure 3.2), the transfer of an electron without reduction or oxidation of atoms indicates that the reorganization energy may be small or negligible.

Typically, intercalation is accompanied by significant volume expansion of the host lattice. For example, the insertion of lithium into graphite increases the number of atoms by 17% and leads to an expansion in the c lattice constant of 10%.[13] However, recently, we synthesized Y_2CF_2 and determined its crystal structure,[11] which we find to be remarkably similar to that of $[Y_2C]^{2+}(e^-)_2$.[10,14] Complete fluorination (Y_2CF_2) increases the number of atoms in $[Y_2C]^{2+}(e^-)_2$ by 66% yet results in an expansion in the c lattice constant by only 5.2% (Table 3.2). Moreover, in the Y_2C system, the a and b lattice constants and intralayer atomic distances all change by <1.1% (Table 3.2). We anticipate that the crystal structure may change its stacking sequence upon EAX, just as the stacking sequence changes in $LiCoO_2$ and graphite upon Li^+ intercalation, but without disrupting local bonding. Importantly, EAX and a lack of redox chemistry facilitate the minimal changes in both volume and the local bonding of the host lattice.

Table 3.2: Lattice constants and atomic distances in Y_2C and Y_2CF_2. Atomic distances in $[Y_2C]^{2+}(e^-)_2$[15] and Y_2CF_2[11] with distances in angstroms and volumes (V) in cubic angstroms as determined experimentally.

	$[Y_2C]^{2+}(e^-)_2$	Y_2CF_2	difference (%)
a	3.62483	3.6651	1.1
c	17.964	18.8907	5.2
Y–Y	2.493	2.510	0.7
Y–C	3.423	3.431	0.2
V	204.413	219.761	7.5

3.2.2 Applications to batteries

Finally, we discuss a natural application of this new mechanism, electrochemical energy storage. We calculated the potential at which electrons insert into Y_2CF_2 to be +0.97 V versus Li/Li^+ (Figure 3.5a), which suggests that $[Y_2C]^{2+}(e^-)_2/Y_2CF_2$ could serve as an anode in a F^- battery. The maximum gravimetric capacity of Y_2CF_2 is a remarkable 282 mAh/g (Figure 3.5b),

comparable to that of $LiCoO_2$ (274 mAh/g).[16] The high capacity is achieved despite using the heavy Y atoms because two F−ions insert into each unit cell of $[Y_2C]^{2+}(e^-)_2$. Therefore, the gravimetric capacity can be improved by using lighter elements, for example, by alloying Y with Sc.[17] Upon replacement of Y with Sc entirely as in Sc_2CF_2, the density can reach 526 mAh/g, > 70% more than that of $LiCoO_2$. Sc_2CF_2 also offers a high maximum volumetric capacity reaching 1634 mAh/cm^3 (Figure 3.5b). Calculations on the Sc_2CF_2 system reveal a small F−diffusion barrier (~500 meV) and useful electron insertion potential (+1.1 V vs Li/Li^+), suggesting that electrochemical electron-anion exchange can enable champion anodes for F−batteries.

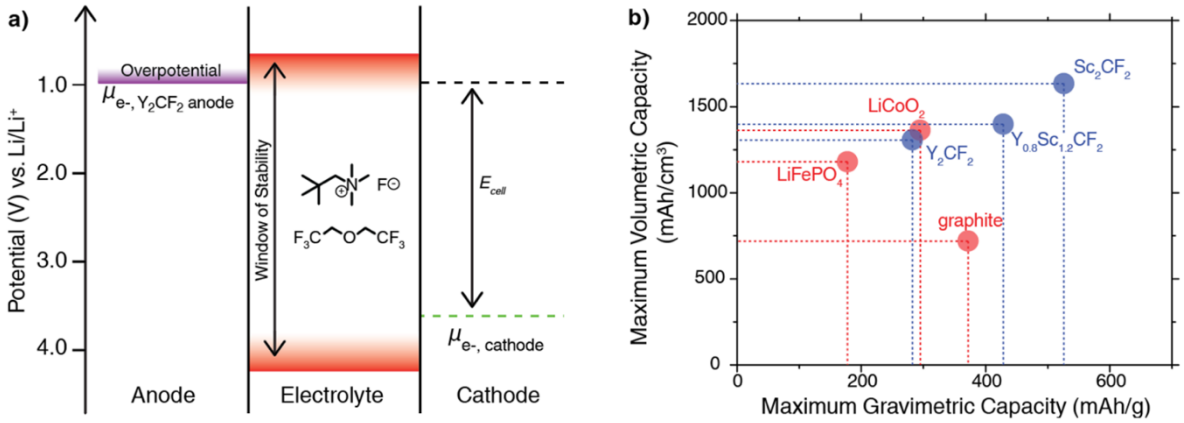


Figure 3.5: Application of electron−anion exchange. (a) Potential diagram of a F−battery utilizing a Y_2CF_2 anode, a NpF_1/BTFE liquid electrolyte, and a cathode (e.g., CuF_2). (b) Comparison of capacities for common Li-ion intercalation electrodes to those of electrodes that use electron−anion exchange.

We are exploring this electrochemistry experimentally in a half-cell configuration with electrodes made of Y_2CF_2 or Y_2C using N,N,N-trimethyl-N-neopentylammonium fluoride

(NpF_1) dissolved in blends of bis(2,2,2-trifluoroethyl)ether and tetraethylene glycol dimethyl ether.[18] Our experiments will be reported in a separate publication.

3.3 Conclusion

We have demonstrated a fundamentally distinct mechanism of electrochemically controlled ion insertion in which an electron reversibly inserts into a lattice without redox chemistry. Our calculations show that this occurs with minimal changes to the structure or oxidation states of the atoms. We suggest that electrochemical electron-anion exchange can address a deficiency in the science and technology of intercalation, the absence of high-capacity electrodes that reversibly intercalate anions at room temperature. We expect that this mechanism will find use in other applications, as well, for example, in information processing, catalysis, and energy conversion.

REFERENCES

(1) Druffel, D. L.; Pawlik, J. T.; Sundberg, J. D.; McRae, L. M.; Lanetti, M. G.; Warren, S. C. First-Principles Prediction of Electrochemical Electron-Anion Exchange: Ion Insertion without Redox. *J. Phys. Chem. Lett.* **2020**, 9210–9214.

(2) Keve, E. T.; Skapski, A. C. Ca_2N: a nitride with a layer structure. *Chem. Commun. (London)* **1966**, No. 22, 829.

(3) Matsuishi, S.; Toda, Y.; Miyakawa, M.; Hayashi, K.; Kamiya, T.; Hirano, M.; Tanaka, I.; Hosono, H. High-density electron anions in a nanoporous single crystal: $[Ca_{24}Al_{28}O_{64}]^{4+}(4e^-)$. *Science* **2003**, *301* (5633), 626–629.

(4) Bowman, A.; Mason, P. V.; Gregory, D. H. Heteroanionic intercalation into positively charged inorganic hosts: the first nitride mixed halides. *Chem. Commun.* **2001**, No. 17, 1650–1651.

(5) Dusastre, V. *Materials for Sustainable Energy: A Collection of Peer-Reviewed Research and Review Articles from Nature Publishing Group*; Co-Published with Macmillan Publishers Ltd, UK, 2010.

(6) Nowroozi, M. A.; Wissel, K.; Rohrer, J.; Munnangi, A. R.; Clemens, O. $LaSrMnO_4$: reversible electrochemical intercalation of fluoride ions in the context of fluoride ion batteries. *Chem. Mater.* **2017**, *29* (8), 3441–3453.

(7) Mohammad, I.; Witter, R.; Fichtner, M.; Anji Reddy, M. Room-Temperature, Rechargeable Solid-State Fluoride-Ion Batteries. *ACS Appl. Energy Mater.* **2018**, *1* (9), 4766–4775.

(8) Okubo, M.; Tanaka, Y.; Zhou, H.; Kudo, T.; Honma, I. Determination of activation energy for Li ion diffusion in electrodes. *J. Phys. Chem. B* **2009**, *113* (9), 2840–2847.

(9) Toyoura, K.; Koyama, Y.; Kuwabara, A.; Oba, F.; Tanaka, I. First-principles approach to chemical diffusion of lithium atoms in a graphite intercalation compound. *Phys. Rev. B* **2008**, *78* (21), 214303.

(10) Zhang, X.; Xiao, Z.; Lei, H.; Toda, Y.; Matsuishi, S.; Kamiya, T.; Ueda, S.; Hosono, H. Two-Dimensional Transition-Metal Electride Y_2C. *Chem. Mater.* **2014**, *26* (22), 6638–6643.

(11) Druffel, D. L.; Lanetti, M. G.; Sundberg, J. D.; Pawlik, J. T.; Stark, M. S.; Donley, C. L.; McRae, L. M.; Scott, K. M.; Warren, S. C. Synthesis and Electronic Structure of a 3D Crystalline Stack of MXene-Like Sheets. *Chem. Mater.* **2019**, *31* (23), 9788–9796.

(12) Huynh, M. H. V.; Meyer, T. J. Proton-coupled electron transfer. *Chem. Rev.* **2007**, *107* (11), 5004–5064.

(13) Schweidler, S.; de Biasi, L.; Schiele, A.; Hartmann, P.; Brezesinski, T.; Janek, J. Volume Changes of Graphite Anodes Revisited: A Combined *Operando* X-ray Diffraction and *In Situ* Pressure Analysis Study. *J. Phys. Chem. C* **2018**, *122* (16), 8829–8835.

(14) Atoji, M.; Kikuchi, M. Crystal structures of cubic and trigonal yttrium hypocarbides; A dimorphically interphased single-crystal study. *J. Chem. Phys.* **1969**, *51* (9), 3863–3872.

(15) Maehlen, J. P.; Yartys, V. A.; Hauback, B. C. Structural studies of deuterides of yttrium carbide. *Journal of Alloys and Compounds* **2003**, *351*, 151–157.

(16) Orman, H. J.; Wiseman, P. J. Cobalt(III) lithium oxide, CoLiO2: structure refinement by powder neutron diffraction. *Acta Crystallogr. C Cryst. Struct. Commun.* **1984**, *40* (1), 12–14.

(17) Park, J.; Hwang, J.-Y.; Lee, K. H.; Kim, S.-G.; Lee, K.; Kim, S. W. Tuning the Spin-Alignment of Interstitial Electrons in Two-Dimensional Y_2C Electride via Chemical Pressure. *J. Am. Chem. Soc.* **2017**, *139* (48), 17277–17280.

(18) Davis, V. K.; Bates, C. M.; Omichi, K.; Savoie, B. M.; Momčilović, N.; Xu, Q.; Wolf, W. J.; Webb, M. A.; Billings, K. J.; Chou, N. H.; et al. Room-temperature cycling of metal fluoride electrodes: Liquid electrolytes for high-energy fluoride ion cells. *Science* **2018**, *362* (6419), 1144–1148.

CHAPTER 4: SYNTHESIS AND ELECTRONIC STRUCTURE OF A 3D CRYSTALLINE STACK OF MXENE-LIKE SHEETS[1]

Daniel L. Druffel,† Matthew G. Lanetti,† Jack D. Sundberg,† Jacob T. Pawlik,† Madeline S. Stark,† Carrie L. Donley,‡ Lauren M. McRae,† Katie M. Scott,† and Scott C. Warren*,†,¶

† Department of Chemistry, University of North Carolina at Chapel Hill, Chapel Hill, North Carolina 27599, United States

‡ Chapel Hill Analytical and Nanofabrication Laboratory (CHANL), University of North Carolina at Chapel Hill, Chapel Hill, North Carolina 27599, United States

¶ Department of Applied Physical Sciences, University of North Carolina at Chapel Hill, Chapel Hill, North Carolina 27599, United States

4.1 Introduction

Research into layered and 2D metal carbides such as MXenes has rapidly grown[2] due to their remarkable properties and applications in electronic,[3,4] sensing,[5,6] and energy storage devices.[7,8] Despite the interest in MXenes in the past decade, MXenes are often highly disordered, which can complicate their study and use. For example, nearly all MXenes have a random mixture of surface terminations (−O, −OH, −F). In addition, restacked 3D films of MXenes have turbostratic disorder[9] and often contain ions, solvent, and other species in between their layers.[10] The presence of multiple surface terminations on MXene sheets and disorder in

[1] Reproduced with permission from (Druffel, D. L.; Lanetti, M. G.; Sundberg, J. D.; Pawlik, J. T.; Stark, M. S.; Donley, C. L.; McRae, L. M.; Scott, K. M.; Warren, S. C. Synthesis and Electronic Structure of a 3D Crystalline Stack of MXene-Like Sheets. Chem. Mater. 2019, 31 (23), 9788–9796. https://doi.org/10.1021/acs.chemmater.9b03722) Copyright 2019 American Chemical Society.

their restacking owes to their usual synthesis, in which HF etches a MAX phase (M = metal; A = Al, Ga, Si, In; and X = C, N) with aqueous HF.[11] Indeed, the only reported MXene with a single surface moiety (−Cl) and without oxygen was prepared through etching a MAX phase in $ZnCl_2$ melts at elevated temperatures.[12]

Given the general interest in MXenes, it is remarkable that no pure (i.e., no −O, −OH) transition metal carbide fluoride has been reported. Of the transition metals, only Ti,[12] Y,[13-17] Sc,[13,18-21] Zr,[13,22,23] and W[24] have been studied as pure metal carbide halides and none as fluorides, leaving a large void in our knowledge of ternary phase diagrams. Our efforts in this work are to synthesize the first transition metal carbide fluoride and to highlight a largely unexplored class of compositions that may find utility in optoelectronics.

Here we report Y_2CF_2, a layered crystal with a unit cell isostructural to a 2D MXene, in which layers are capped only by fluoride anions. Relatively strong electrostatic interactions bind the layers together into a 3D crystal. Therefore, we consider Y_2CF_2 as a pure 3D crystalline stack of MXene-like sheets. Instead of the etching approach, we describe an alternative synthetic method. We directly synthesize the 3D crystal through a high-temperature solid-state reaction in the absence of air and water. The synthesis affords the 3D crystal in high yield and purity and ensures that only fluoride ions terminate the layers. This allows us to identify several useful properties of Y_2CF_2: an indirect band gap of 1.6 eV, a direct band gap of 1.9 eV, and a small ionization potential of 3.8 eV. In addition, the crystals have modest charge transport properties, with an electron effective mass of 2.0 m_e and a hole effective mass of 4.0 m_e. This realization of a 3D crystalline stack of MXene-like sheets will enable a comparison to their 2D MXene counterparts to better understand the influence of disorder and surfaces on their optoelectronic properties.

4.2 Results

4.2.1 Synthesis and crystal structure

We combined yttrium, carbon, and fluorine in a stoichiometry of Y_2CF_2 at 1240°C in sealed tantalum ampules according to the following reaction:

$$4\,Y + 3\,C + 2\,YF_3 \rightarrow 3\,Y_2CF_2$$

The product is a pellet of beautiful green crystals (Figure 4.1a) that easily grinds into a powder (Figure 4.1b). Unfortunately, the synthesized crystals were too small and intergrown to perform single-crystal XRD measurements. Therefore, we combined two independent approaches to determine the crystal structure. First, we performed powder XRD experiments of the product and obtained a diffraction pattern (Figure 4.1c), which indexed as a trigonal crystal structure with space group $P\bar{3}m1 - D_{3d}$. Then, we refined the pattern by the Rietveld method[25] (Table 4.1). The analysis confirms that the trigonal space group $P\bar{3}m1$ is a good fit, with lattice constants a = 3.6651(3) Å and c = 6.29697(7) Å at room temperature (Figure 4.1c, Table 4.1). To show unambiguously that Y_2CF_2 is a layered structure, we also performed a measurement beginning at lower angles to capture reflections from the {00l} set of planes, including that from the (001) plane at 14.05°.

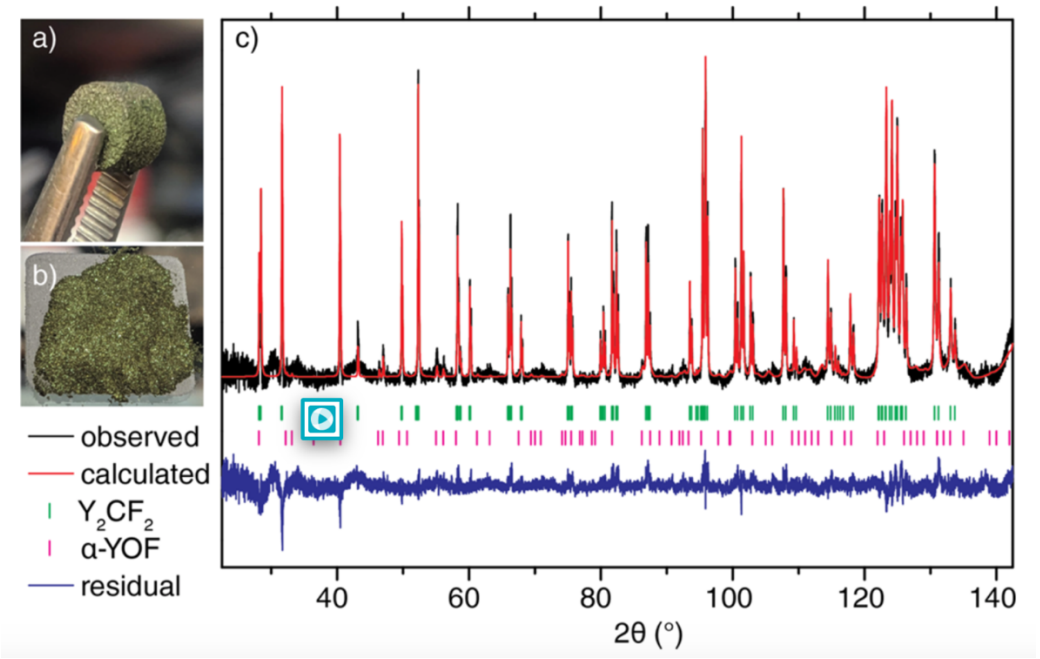


Figure 4.1: X-ray diffraction of Y_2CF_2. (a) Photograph of a pellet of Y_2CF_2 as synthesized. (b) Photograph of Y_2CF_2 ground in a mortar and pestle into a powder. (c) Observed, calculated, and residual profiles for Y_2CF_2 at 300 K measured on a Rigaku Smartlab diffractometer with a Cu K α source, λ = 1.5406 Å. The pattern was refined to two phases, a Y_2CF_2 phase and an α -YOF phase (space group $P4/nmm$, a = 3.922 (2) Å, c = 5.409 (4) Å), which made up less than 4% by mole of the sample. Vertical tick marks indicate calculated reflection positions. The broad maxima in the background are due to diffuse scattering from the quartz ampule.

Table 4.1: Final Parameters and R Factors for Y_2CF_2 at 300 K.*

atom	site	symmetry	*X*	*Y*	*Z*	*B* (Å²)	*N*	Occupancy
Y	2d	3*m*	13	23	0.21450(10)	0.526(12)	2	1.00(1)
C	1a	$\bar{3}m$	0	0	0	0.1(4)	1	0.93(3)
F	2d	3*m*	13	23	0.0.6031(5)	0.555(11)	2	1.00(6)

* Space group $P\bar{3}m1$. a = 3.6651 (3) Å, c = 6.29697 (7) Å. Volume = 73.2536 Å^3, density = 4.394 g cm^{-3}. Rietveld analysis standard agreement indices are the residual factor R_p = 2.5%, the weighted residual factor R_{wp} = 4.97%, and the goodness of fit factor S = 1.96. U, V, W (deg^2): 0.000, − 0.021, 0.00.

Independently, we used an evolutionary search algorithm, USPEX,[26] to explore computationally the stability of crystal structures for the composition Y_2CF_2. The algorithm computes the enthalpy of hundreds of candidate crystal structures and uses similarities in bond distances, coordination, symmetry, and a number of other identifiers to find the most stable phase for a given composition. Using the algorithm, we found that the $P\bar{3}m1$ structure is the most enthalpically favorable phase for the composition Y_2CF_2, in agreement with our diffraction experiments. The closest metastable phase is 46 meV/atom higher in energy than that of the $P\bar{3}m1$ structure. We then performed a geometry optimization calculation on the $P\bar{3}m1$ structure using the PBEsol[27] functional, which yielded lattice constants very close to the experimental values (1.6% shorter in a and 0.8% shorter in c, Figure 4.2b).

We also note that many yttrium compounds are isostructural to gadolinium and holmium compounds (e.g., YOCl, YCl_3, YF_3) because of the similarity in the crystallographic ionic radius of Y (104 pm)[28] to that of Gd and Y (108 and 104 pm, respectively).[28] In support of our indexing, we found known gadolinium and holmium compounds (Gd_2CF_2[29] and Ho_2CF_2[30]) isostructural to Y_2CF_2 with similar lattice constants.

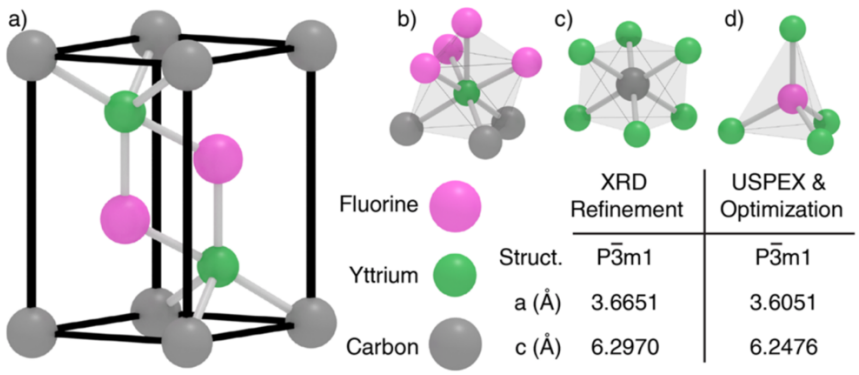


Figure 4.2: Crystal structure of Y_2CF_2. (a) Crystal structure, (b − d) bonding polyhedra, and lattice constants for Y_2CF_2. The crystal structure and lattice constants were obtained independently from two methods: (1) experimental synthesis and Rietveld refinement of X-ray diffraction data and (2) USPEX, a DFT-based search algorithm to find the most stable crystal structure for a given composition. After using USPEX to identify the structure, the structure was optimized using the PBEsol functional as described in the Methods.

The crystal structure of Y_2CF_2 (Figure 4.2a) is similar to that of MXenes. Six Y cations octahedrally coordinate each carbon atom, and the octahedra (Figure 4.2c) form into a two-dimensional layer, just like the 2D Ti_2C (−O, −OH, −F) MXene.[31] However, in the Y_2CF_2 structure, each Y cation also coordinates to four F anions, forming face-capped octahedra (Figure 4.2b). Thus, in Y_2CF_2, double layers of fluoride ions bind adjacent metal−carbide layers forming a crystalline 3D stack of MXene-like sheets.

Naturally, we became interested in the interlayer bonding of Y_2CF_2, which is distinct from the 2D nature of MXenes. Each F coordinates to four Y with four nearly symmetric distances (Figure 4.3c), three to the Y in the adjacent layer (2.408 Å) and one to the Y in the opposite layer at an only slightly elongated distance (2.447 Å) (Table 4.2). This suggests that the interlayer bonding is relatively strong and highly ionic in nature.

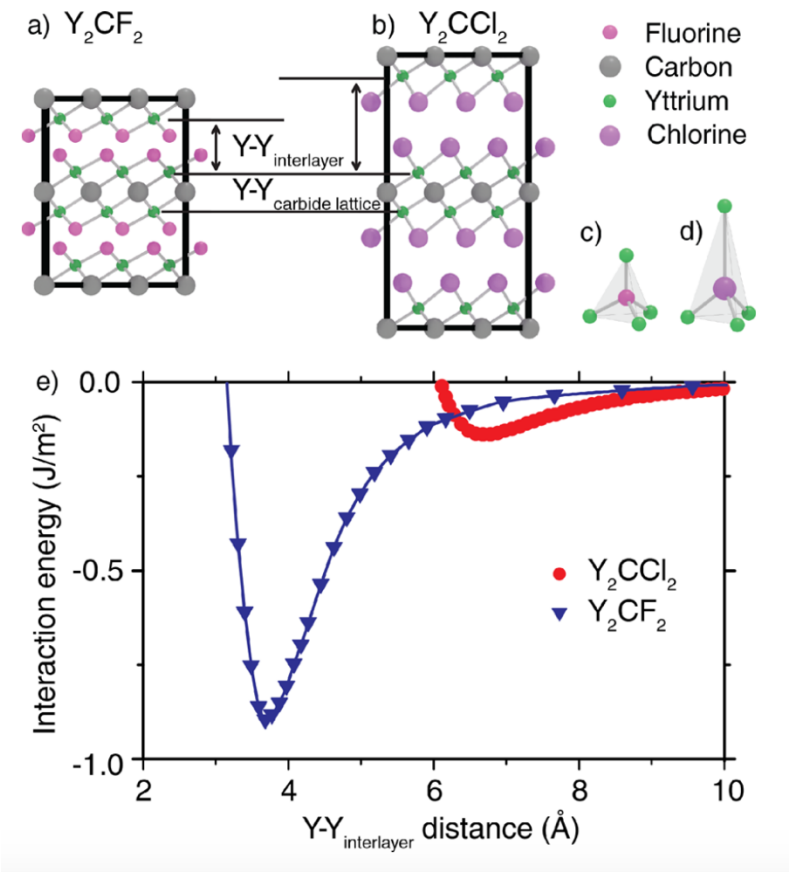


Figure 4.3: Comparison of Y_2CF_2 and Y_2CCl_2 structure and binding energy. Comparison of the crystal structure of (a) Y_2CF_2 to (b) Y_2CCl_2 showing the unit cells along the [100] axis, the tetrahedral bonding polyhedron for yttrium and fluorine in (c) Y_2CF_2 and the same polyhedron drawn for (d) Y_2CCl_2 with the elongated Y−Cl distance in the z -direction, and (e) the interlayer binding energy for Y_2CF_2 (blue) and Y_2CCl_2 (red) calculated using the PBEsol functional.

Table 4.2: Interatomic distances in the crystal structure of Y_2CF_2, determined by the refinement of powder X-ray diffraction data

atom	interatomic distances (Å)
Y–Y	3.4315(2), 3.6651(3), 4.1720(1)
Y–F	2.4077(3), 2.4470(1)
F–F	2.4827(7)
Y–C	2.5104(6)
F–C	3.2747(6)

This electrostatic interlayer bonding contrasts with that of other known layered metal carbide halides. For example, in Y_2CCl_2,[13] which shares the same crystal structure (Figure 4.3b), Cl coordinates only to three Y, all in the adjacent layer (2.755 Å). The distance to the Y in the opposite layer is nearly double (4.770 Å), far too long for any Y−Cl bonding interaction (Figure 4.3d). Instead, the primary interlayer interactions in Y_2CCl_2 are weak van der Waals forces.

Using the PBEsol functional, we calculated the binding energy- the energy difference between the equilibrium bulk separation and the state in which the planes are separated by an infinite distance, as approximated by a 15 Å-thick vacuum gap (Figure 4.3e). The binding energy for Y_2CF_2 is 0.90 J/m^2, over 6× that of Y_2CCl_2 (0.14 J/m^2) and 3× that of graphite (0.34 J/m^2).[32] Electrostatic interactions between the F anion and the Y cation likely account for the greater binding energy. This leads us to conclude that Y_2CF_2 is an ionic crystal in the out-of-plane direction. Still, the binding energy of Y_2CF_2 is less than that of other layered crystals that have been exfoliated successfully into 2D flakes, for example, Ca_2N (1.11 J/m^2).[33] These calculations suggest that it may be possible to exfoliate Y_2CF_2 into 2D flakes, although with somewhat greater difficulty than van der Waals crystals like Y_2CCl_2 or graphite.

4.2.2 Composition and purity

We sought to confirm the composition of our sample, as some metal carbides can sustain a variety of nonstoichiometric compositions. We used EDS to quantify the amount of yttrium and fluorine and measured a ratio of 1:0.98 ± 0.05 Y:F in agreement with the stoichiometry of Y_2CF_2. These results also agree with the refinement from powder X-ray measurements, which yielded an occupancy of 1.00 ± 0.01 and 1.00 ± 0.06 for yttrium and fluorine, respectively, in each of their 2d sites (Table 4.1). Unfortunately, our EDS instrument does not quantify carbon reliably because the signal is obscured by electronic noise. Therefore, we quantified carbon by

refining the occupancy of the carbon site during the Rietveld refinement, which revealed that only 93 ± 3% are occupied. We conclude that the composition Y_2CF_2 represents the synthesized phase, though the real structure has carbon vacancies, $Y_2C_{0.93}F_2$.

4.2.3 Electronic structure of Y_2CF_2

To investigate the effect of interlayer ionic bonding on the electronic structure of stacked MXene-like sheets, we examined the material's optoelectronic properties using both experiment and computation. First, we performed transmission measurements to quantify the absorption coefficient (Figure 4.4a). We observe a gradual increase in absorption beginning at ∼775 nm (1.6 eV), which we attribute to the band gap. The absorption increases and plateaus from 400 to 550 nm at a magnitude of 3.4×10^4 cm^{-1}. The absorption coefficient has local maxima at 340 nm and again at 240 nm, though the local maximum at 240 nm is obscured by the attenuation of our quartz substrate. Our computational model shows a gradual increase in absorption beginning at 700 nm (1.7 eV; Figure 4.4b), in excellent agreement with our experimental measurements. The absorption coefficient plateaus from 375 to 450 nm at a magnitude of 3.4×10^4 cm^{-1}, nearly identical to our experiment. Finally, the model predicts peaks at 300 and 210 nm, red-shifted only 40 nm from our experimental data.

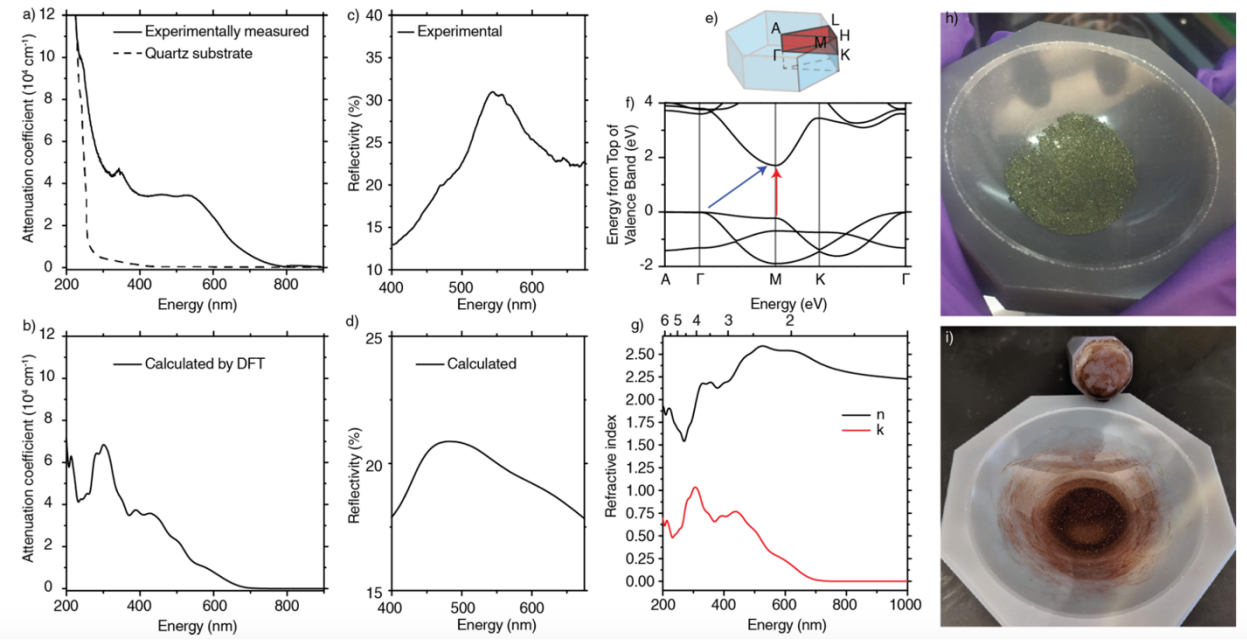


Figure 4.4: Optical properties of Y_2CF_2. Attenuation coefficient (a) measured experimentally, which does not include the contribution from the quartz substrate; however, at wavelengths shorter than 250 nm the signal was dominated and obscured by that of the quartz. (b) Attenuation coefficient calculated by DFT. Reflectivity (c) measured experimentally and (d) calculated by DFT. (e) First Brillouin zone for Y_2CF_2 Γ with the irreducible Brillouin zone highlighted in red and (f) electronic band structure where the M − Γ vector runs along (010), while the Γ − A vector runs along (001). (g) Optical constants, n and k, calculated by DFT. Photograph of (h) green Y_2CF_2 before grinding and (i) red Y_2CF_2 after grinding.

Next, we performed specular-reflectance measurements on single facets of individual Y_2CF_2 crystals using a microspectrophotometer. To obtain a representative spectrum, we averaged the spectra from individual crystallites together (Figure 4.4c). The representative spectrum has a peak at 540 nm, corresponding to yellow-green light. To compare with our model of the electronic structure, we calculated the reflectivity for the bulk Y_2CF_2 (Figure 4.4d), which shows a single broad peak at 500 nm, again red-shifted only 40 nm from experiment. We do note

that the intensity of the reflection in the experiment is roughly 50% larger than that in the computation. While the computation provides qualitative information, it does not consider all of the complexity of the real system (e.g., chemical differences at the surface, an interface with a changing dielectric, or the convolution of reflection and absorption events). Therefore, we attribute the difference in magnitude to these factors. Despite this difference, the model reproduces the major features of the experiment well.

We calculated the electronic band structure for the first Brillouin zone of Y_2CF_2, shown in Figure 4.4e,f. In agreement with our experimental measurements, we calculate that Y_2CF_2 is a semiconductor with an indirect gap of 1.7 eV (from Γ − M) and a direct gap of 1.9 eV (M − M; Figure 4.4f). From the band structure, we can understand that the low absorption coefficient at 700 nm (Figure 4.4a,b) is due to the indirect nature of the transitions and the low density of states in the conduction band. Moreover, we gain information about the band dispersion. The bottom of the conduction band has a parabolic band dispersion, which should correspond to a modest effective mass (2.0 m_e) for electrons in the conduction band. In contrast, the valence band is relatively flat giving rise to a higher hole effective mass (4.0 m_e). Interestingly, the band has almost no dispersion along the path Γ – A (Figure 4.4f) indicating very limited overlap of orbitals in the z -direction. This is likely due to the strong localization of electrons around the nucleus of the fluorine atoms, which separate layers of yttrium and carbon atoms. Therefore, the ionic bonding between MXene-like sheets effectively insulates the sheets from one another electronically, which will give rise to highly anisotropic optoelectronic properties.

Because of the excellent agreement between theory and experiment, we present the optical constants (Figure 4.4g), n and k, calculated using the HSE06 functional with confidence that the energy dependence of the optical constants and that the magnitude of k represent the

synthesized Y_2CF_2. Due to the difference in magnitude between experiment and calculation, there is more uncertainty in the magnitude of n.

The electronic structure also explains an observation about the perceived color of Y_2CF_2. When we ground the green crystals (Figure 4.4g) in a glovebox in the absence of air or water, the material transforms into a red powder (Figure 4.4i). By examining the electronic structure, we conclude that the initially perceived green color is due to specular reflection of green light from flat crystalline surfaces, as evidenced by the peak in reflection at 540 nm in Figure 4.4c. By grinding the crystals into small particles, we destroy the flat surfaces and the specular reflection of green light. Once ground, absorption originating from the band gap at 775 nm dominates the apparent color of the material. To test this hypothesis, we ball milled the crystals to a fine powder with a particle size qualitatively determined as less than 5 μm. We confirmed, via powder XRD, that the crystal structure is preserved after ball milling. Then we measured the reflectance of the finely ground sample using a microspectrophotometer. We found that the peak at 540 nm, observed for the green crystals, was not present in the ball-milled sample.

4.2.4 Sensitivity to oxygen

This understanding of Y_2CF_2's electronic structure also led us to explore its sensitivity to oxygen and water. We removed samples of crystalline Y_2CF_2 from the glovebox, exposing the crystals to air and water for one month. After two weeks, the once-green crystals appeared red. Examining the crystals in the microspectrophotometer in reflectance mode, we found that the peak at 540 nm corresponding to the green color was not present. Instead, we observe rainbow striping and periodic oscillating signals in the reflectance spectra, which are indicative of thin film optical interference. The formation of a thin film on the surface of many semiconductors is

commonly caused by a slow reaction with air or water, which forms a thin oxide coating.[34] Therefore, we suspected that Y_2CF_2 in air develops a thin film of an oxide or related species.

To test whether the Y_2CF_2 crystals react with oxygen or water, we performed X-ray photoemission spectroscopy (XPS) on crystals exposed to air for one week and on crystals kept in the glovebox. We examined the yttrium 3d, carbon 1s, fluorine 1s, and carbon 1s core electron binding energies (Table 4.3). For the sample exposed to air for 1 week, we observed a single peak at a binding energy of 684.8 eV (Figure 4.5a) corresponding to the F 1s core binding energy, in agreement with the binding energy of fluoride.[35] However, the Y:F ratio measured through XPS quantitative analysis is 1:0.5, suggesting a deficiency of fluorine at the surface. In the Y 3d spectrum we observe a doublet with a binding energy of 157.7 eV (Figure 4.5c). The position of this peak matches that of yttrium carbonate ($Y_2(CO_3)_3$)[36] and is too high to be the expected Y^{2+} oxidation state (~156 eV).[37] In addition, the spectrum of the carbon 1s core (Figure 4.5b) reveals two distinct peaks, one centered at 284.6 eV, which is adventitious carbon, and one centered at 289.4 eV, which matches that of a carbonate (Figure 4.5b).[38] Moreover, through quantitative XPS analysis, we measure the ratio of Y:O to be 1:2.1, which can only be explained by a carbonate, not Y_2O_3 or YOF. Therefore, the data suggest the surface of the sample exposed to air has oxidized, at least partially, to yttrium carbonate.

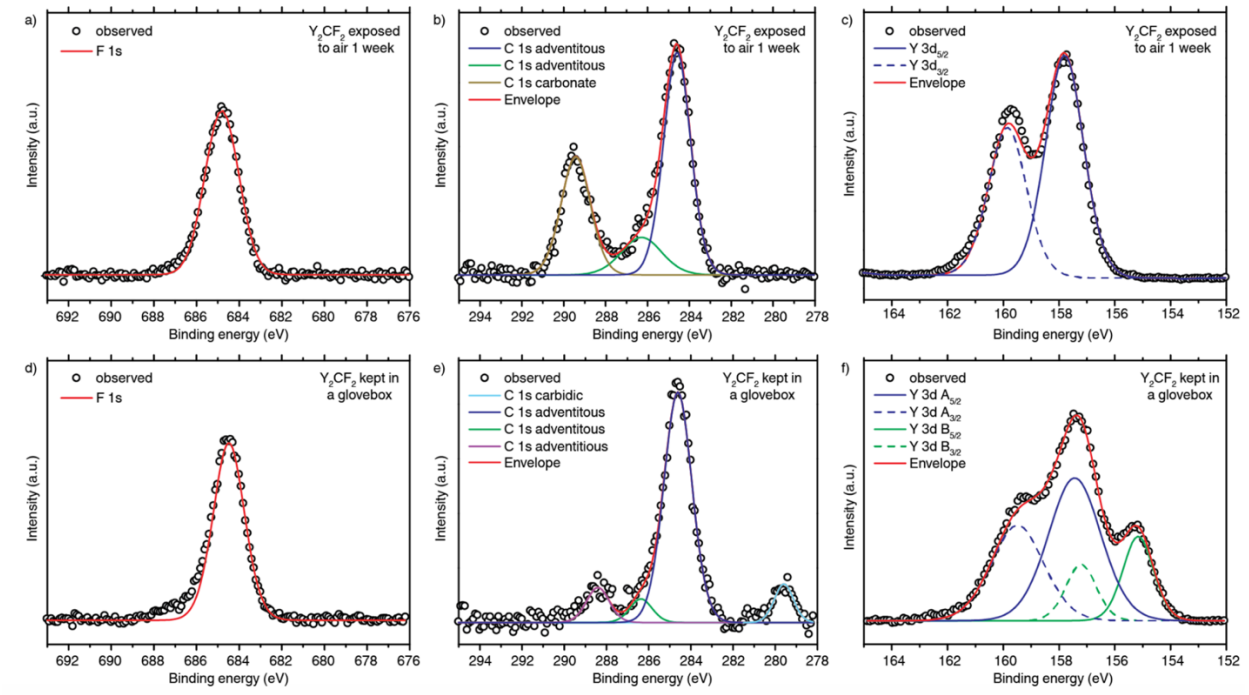


Figure 4.5: XPS of Y_2CF_2 samples. X-ray photoemission spectra from Y_2CF_2 exposed to air for 1 week for the (a) fluorine 1s, (b) carbon 1s, and (c) yttrium 3d core electron binding energies. X-ray photoemission spectra from Y_2CF_2 kept in a glovebox for the (d) fluorine 1s, (e) carbon 1s, and (f) yttrium 3d core electron binding energies.

Table 4.3: XPS binding energy data from Y_2CF_2 samples. X-ray photoemission spectra from Y_2CF_2 exposed to air for 1 week, after sputtering, and from Y_2CF_2 kept in an Ar-filled glovebox (oxygen < 0.01 ppm) for 1 week.*

sample	atom	core	binding energy[b]	fwhm	atomic %
air-exposed	Y	$3d^5/_2$	157.6	1.56	21.3
	C_{adv}	1s	284.6,[b] 286.3	1.33, 2.24	17.1
	$C_{carbonate}$	1s	289.4	1.63	7.9
	F	1s	684.8	1.81	10.5
	O	1s	531.2	1.88	43.2
air-exposed sputtered	Y	$3d^5/_2$	157.6	2.58	33.8
	C_{adv}	1s	284.6[b], 286.0	1.67, 1.76	5.3
	$C_{carbonate}$	1s	289.9	1.57	1.9
	F	1s	685.0	2.11	16.9
	O	1s	531.3	3.91	42.1
glovebox	Y	$3d^5/_2$	155.3	1.27	6.7
	Y	$3d^5/_2$	157.6	2.19	19.4
	$C_{carbide}$	1s	279.6	1.04	4.5
	C_{adv}	1s	284.6,[b] 286.3	1.25, 1.55	27.4
	F	1s	684.4	1.75	18.8
	O	1s	531.2	2.33	27.1

*All binding energies and full-width at half-maximum values given in eV. [b]All binding energies were referenced to adventitious carbon (284.6 eV).

We attempted to clean the surface of the air-exposed sample by argon ion sputtering. Both the oxygen 1s and carbon 1s signals decrease in intensity relative to the yttrium (Table 4.3). The Y:O ratio decreases to 1:1.2. This suggests that the oxidation is a surface effect. For additional support of that hypothesis, we performed XRD measurements on the samples exposed to air. We found the crystal structure remained intact after exposure to air for 1−4 weeks, which supports the conclusion that the oxidation affects the surface and not the bulk of the sample.

For the sample kept in a glovebox, the sample was briefly exposed to air during the transfer into the XPS instrument. We attempted this measurement multiple times and found that the sample is prone to charging. Here, we present the data from the experiment that showed the

least charging. The F 1s spectrum (Figure 4.5d) has a single peak at 684.4 eV similar to that of the air-exposed sample (Table 4.3). We attribute the small tail at higher binding energies in the F 1s spectrum to this charging. The carbon 1s spectrum (Figure 4.5e) shows one main peak, which we attribute to adventitious carbon (Table 4.3) and which we used to reference the data. Referencing to any other carbon peak yields unreasonable values for the peaks of other elements. In addition to the adventitious carbon, we observe a peak at a very low binding energy (279.6 eV). Carbidic carbon in similar materials, for example, Sc_2CCl_2 (281.8 eV),[13] TiC (281.5 eV),[39] ZrC (281.1 eV),[40] and HfC (280.8 eV),[40] gives rise to peaks at low binding energies, but none quite as low as what we observe here. Therefore, we considered that the signal could be due to other elements, which have signals at similar binding energies (Os 4d, Ru 3d, Sr 3p, Tb 4p, and Cl 2s). We rule out Os, Sr, Tb, and Cl because the XPS survey scan reveals that the most intense peaks for these elements are absent (Os 4f at 50 − 55 eV,[41] Sr 3d and 3s at 130 − 135 and 357 eV, respectively,[42] Tb 4d at 150 eV,[43] and Cl 2p at 198 − 208 eV[44]). The most intense peak for Ru is the 3d peak, so we cannot rule out Ru directly. However, we have no reason to suspect the incorporation of Ru into our sample and its weaker peaks are absent (Ru 4s at 75 eV, Ru 3p at 463 eV, and Ru 3s at 586 eV).[45] Therefore, we assign the peak at 279.6 eV as carbidic carbon in Y_2CF_2, consistent with a highly reduced form of carbon. We also note that we do not observe the signal at higher binding energies of a carbonate species for the sample kept in the glovebox.

Finally, in the Y 3d spectrum, we observe two distinct yttrium signals (Figure 4.5f). One contribution is from a reduced form of yttrium with a binding energy of 155.3 eV, and a second contribution is from an oxidized form of yttrium at 157.6 eV that matches that of the air-exposed sample. A reduced form of yttrium is consistent with our understanding of Y_2CF_2, in which we expect the Y adopts a 2+ oxidation state. The second contribution is broadened compared to the

air-exposed sample possibly due to the small amount of charging present during the collection of data. Therefore, we conclude that the surface of Y_2CF_2 oxidizes quickly during the brief transfer of the sample into the instrument and that the oxidation affects the reduced yttrium and carbidic carbon at the surface.

We return to the electronic structure to understand why Y_2CF_2 oxidizes in air. We combined several measurements and calculations to place the band edges of Y_2CF_2 on an absolute scale along with the reduction potentials of oxygen and water, which are likely redox couples.[34] DFT calculations gave the valence band edge (Figure 4.6a) and band gaps (Figure 4.6b), which are supported by our spectroscopic measurements (Figure 4.4a). The valence band edge is at a higher energy than the reduction potentials of oxygen and water, which explains why the material oxidizes. We gain further understanding of its reactivity through analysis of the partial density of states (PDOS), deconstructed into the elemental compositions and angular momentum (Figure 4.6c−e). The valence band consists of Y 4d and C 2p states. The C 2p states lie at high energies, and therefore the electrons occupying these states can be readily donated to oxygen and water, producing hydroxide. If this initial oxidation is not self-limiting, more highly oxidized products may form, such as yttrium carbonate. This mechanism is consistent with the XPS observations of fast partial oxidation to an oxide or hydroxide after a brief exposure to air and a subsequent slow oxidation to a more oxidized form.

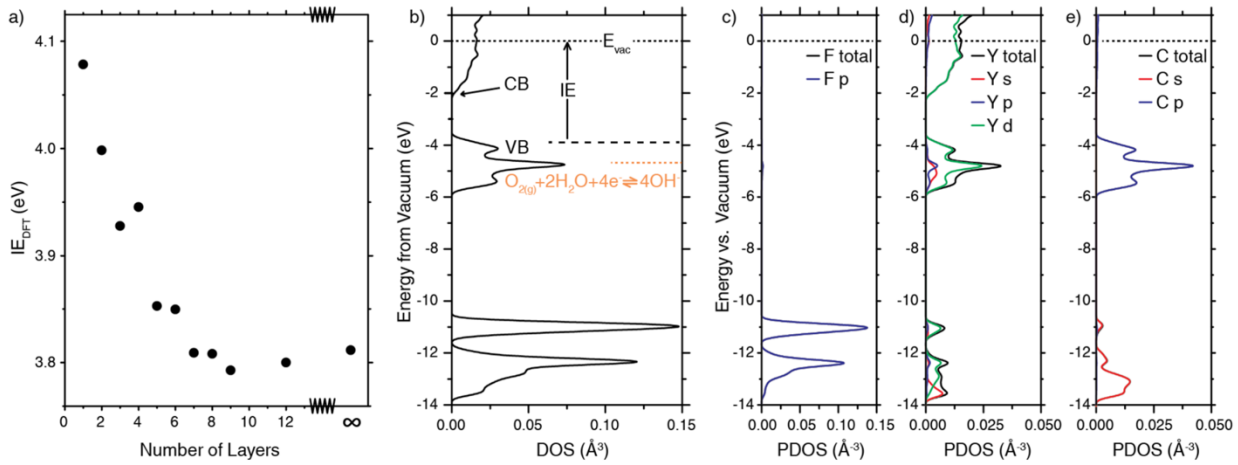


Figure 4.6: Band positions of Y_2CF_2 on an absolute scale. (a) Calculations of the ionization potential (IE) by DFT as described in the Methods for increasingly thick slabs of Y_2CF_2, which plateau at a value of ~3.8 eV for a 12-layer slab and for a bulk crystal. (b) Density of states (DOS) of bulk Y_2CF_2 calculated by DFT referenced to vacuum energy using the calculated ionization potential, showing the valence band (VB) and conduction band (CB). The partial density of states for (c) fluorine, (d) yttrium, and (e) carbon in Y_2CF_2.

In general, MXenes have been considered stable in air and water; however, growing evidence reveals that MXenes decompose over the course of a few days to a few weeks.[46-50] For example, Ti_3C_2 (−O, −OH, −F) decomposes to form TiO_2 in the presence of oxygen,[46,49] and water.[48,51] In fact, the etching synthetic method, which uses strong oxidants like HF,[11] H_2O_2,[52] or HCl/LiF[53] contributes to the oxidation, as evidenced by the formation of −O terminating moieties. The oxidation has consequences on the electronic structure.[54] For example, the work function of Ti_3C_2 (−O, −OH, −F) was predicted to vary from 1.9 to 6.2 eV depending on the surface terminations.[55] Moreover, the work function of MXenes with random surface moieties depends on the complex interplay between the different surface moieties and their local dipoles.[56]

In this context, Y_2CF_2 and crystalline stacked MXenes provide an opportunity. The uniform, single F− moiety of crystalline stacked MXenes could facilitate experiments to understand and control its surface oxidation. Although we have observed that Y_2CF_2 oxidizes in air, the material reported here is intrinsically oxygen-free, unlike the 2D MXenes synthesized by etching in aqueous HF. It therefore provides a reference for detecting changes in surface composition and surface properties. If this pristine 3D crystal can be exfoliated in water-free or oxygen-free conditions, it may also yield an unoxidized, pristine 2D MXene. In addition, the 3D crystalline form eliminates both the turbostratic disorder and the incorporation of solvent, ions, and other species between sheets found in restacked films of MXene sheets, which likely gives superior optoelectronic properties.

4.3 Conclusion

We have synthesized Y_2CF_2, a crystalline, 3D stack of MXene-like sheets capped exclusively by fluorine. Instead of the etching approach, we introduce a new synthetic method to directly synthesize the 3D crystal through a high-temperature solid-state reaction that ensures that only fluorine terminates the layers. Unlike MXenes, ionic bonds hold layers together. Interestingly, because the fluorine orbitals contribute to neither the valence band nor the conduction band, the fluorine layers electrically isolate the yttrium carbide layers from each other. This imparts to the 3D crystal 2D-like electronic transport and supports an understanding of these materials as a crystalline stack of MXene-like sheets. The valence band edge, made of Y 4d and C 2p states, sits at a high energy, affording reducing character, which makes the crystal sensitive to air but also suggests that the crystal could be useful in applications in electronics, sensing, and energy storage.

REFERENCES

(1) Druffel, D. L.; Lanetti, M. G.; Sundberg, J. D.; Pawlik, J. T.; Stark, M. S.; Donley, C. L.; McRae, L. M.; Scott, K. M.; Warren, S. C. Synthesis and Electronic Structure of a 3D Crystalline Stack of MXene-Like Sheets. Chem. Mater. 2019, 31 (23), 9788–9796.

(2) Naguib, M.; Mochalin, V. N.; Barsoum, M. W.; Gogotsi, Y. 25th anniversary article: MXenes: a new family of two-dimensional materials. *Adv. Mater. Weinheim* **2014**, *26* (7), 992–1005.

(3) Zhao, M.-Q.; Ren, C. E.; Ling, Z.; Lukatskaya, M. R.; Zhang, C.; Van Aken, K. L.; Barsoum, M. W.; Gogotsi, Y. Flexible MXene/carbon nanotube composite paper with high volumetric capacitance. *Adv. Mater. Weinheim* **2015**, *27* (2), 339–345.

(4) Li, R.; Zhang, L.; Shi, L.; Wang, P. MXene Ti3C2: An Effective 2D Light-to-Heat Conversion Material. *ACS Nano* **2017**, *11* (4), 3752–3759.

(5) Kim, S. J.; Koh, H.-J.; Ren, C. E.; Kwon, O.; Maleski, K.; Cho, S.-Y.; Anasori, B.; Kim, C.-K.; Choi, Y.-K.; Kim, J.; et al. Metallic $Ti_3C_2T_x$ MXene Gas Sensors with Ultrahigh Signal-to-Noise Ratio. *ACS Nano* **2018**, *12* (2), 986–993.

(6) Yu, X.; Li, Y.; Cheng, J.; Liu, Z.; Li, Q.; Li, W.; Yang, X.; Xiao, B. Monolayer Ti_2CO_2: A Promising Candidate for NH_3 Sensor or Capturer with High Sensitivity and Selectivity. *ACS Appl. Mater. Interfaces* **2015**, *7* (24), 13707–13713.

(7) Naguib, M.; Come, J.; Dyatkin, B.; Presser, V.; Taberna, P.-L.; Simon, P.; Barsoum, M. W.; Gogotsi, Y. MXene: a promising transition metal carbide anode for lithium-ion batteries. *Electrochem. commun.* **2012**, *16* (1), 61–64.

(8) Liang, X.; Garsuch, A.; Nazar, L. F. Sulfur cathodes based on conductive MXene nanosheets for high-performance lithium-sulfur batteries. *Angew. Chem. Int. Ed. Engl.* **2015**, *54* (13), 3907–3911.

(9) Ghidiu, M.; Barsoum, M. W. The {110} reflection in X-ray diffraction of MXene films: Misinterpretation and measurement via non-standard orientation. *J. Am. Ceram. Soc.* **2017**, *100* (12), 5395–5399.

(10) Ren, C. E.; Hatzell, K. B.; Alhabeb, M.; Ling, Z.; Mahmoud, K. A.; Gogotsi, Y. Charge- and Size-Selective Ion Sieving Through $Ti_3C_2T_x$ MXene Membranes. *J. Phys. Chem. Lett.* **2015**, *6* (20), 4026–4031.

(11) Naguib, M.; Kurtoglu, M.; Presser, V.; Lu, J.; Niu, J.; Heon, M.; Hultman, L.; Gogotsi, Y.; Barsoum, M. W. Two-dimensional nanocrystals produced by exfoliation of Ti_3AlC_2. *Adv. Mater. Weinheim* **2011**, *23* (37), 4248–4253.

(12) Lu, J.; Persson, I.; Lind, H.; Palisaitis, J.; Li, M.; Li, Y.; Chen, K.; Zhou, J.; Du, S.; Chai, Z.; et al. $Ti_{n+1}C_n$ MXenes with fully saturated and thermally stable Cl terminations. *Nanoscale Adv.* **2019**, *1* (9), 3680–3685.

(13) Hwu, S.-J.; Ziebarth, R. P.; Von Winbush, S.; Ford, J. E.; Corbett, J. D. Synthesis and Structure of Double-Metal-Layered Scandium, Yttrium, and Zirconium Chloride Carbides and Nitrides, M_2Cl_2C and M_2Cl_2N. *Inorg. Chem* **1986**, *25*, 283–287.

(14) Henn, R. W.; Schnelle, W.; Kremer, R. K.; Simon, A. Bulk superconductivity at 10 K in the layered compounds $Y_2C_2I_2$ and $Y_2C_2Br_2$. *Phys. Rev. Lett.* **1996**, *77* (2), 374–377.

(15) Ahn, K.; Kremer, R. K.; Simon, A.; Marshall, W. G.; Puschnig, P.; Ambrosch-Draxl, C. Influence of pressure on the structure and electronic properties of the layered superconductor $Y_2C_2I_2$. *J. Phys. Condens. Matter* **2005**, *17* (40), S3121–S3130.

(16) Kauzlarich, S. M.; Hughbanks, T.; Corbett, J. D.; Klavins, P.; Shelton, R. N. Two extended metal chain compounds, yttrium iodide carbides (Y_4I_5C and $Y_6I_7C_2$). Synthesis, structure, properties, and bonding. *Inorg. Chem.* **1988**, *27* (10), 1791–1797.

(17) Simon, A.; Backer, M.; Henn, R. W.; Felser, C.; Kremer, R. K.; Mattausch, H.; Yoshiasa, A. Supraleitung in Seltenerdmetall-Carbidhalogeniden des Typs $SE_2X_2C_2$. *Z. anorg. allg. Chem.* **1996**, *622* (1), 123–137.

(18) Jongen, L.; Mudring, A.-V.; Meyer, G. The molecular solid $Sc_{24}C_{10}I_{30}$: a truncated, hollow T4 supertetrahedron of iodine filled with a T3 supertetrahedron of scandium that encapsulates the adamantoid cluster Sc_4C_{10}. *Angew. Chem. Int. Ed. Engl.* **2006**, *45* (12), 1886–1889.

(19) Dudis, D. S.; Corbett, J. D.; Hwu, S. J. Synthesis, characterization, and crystal structures of two scandium cluster carbides and a boride, $Sc_7X_{12}C$ (X = I, Br) and $Sc_7I_{12}B$. *Inorg. Chem.* **1986**, *25* (19), 3434–3438.

(20) Hwu, S.-J.; Corbett, J. D. Metal-metal-bonded scandium cluster ($Sc_7Cl_{12}Z$) and infinite chain (Sc_4Cl_6Z) phases stabilized by interstitial boron or nitrogen (Z). *J. Solid State Chem.* **1986**, *64* (3), 331–346.

(21) Hwu, S.-J.; Corbett, J. D.; Poeppelmeier, K. R. Interstitial atoms in metal-metal bonded arrays: The synthesis and characterization of heptascandium decachlorodicarbide, $Sc_7Cl_{10}C_2$, and comparison with the interstitial-free Sc_7Cl_{10}. *J. Solid State Chem.* **1985**, *57* (1), 43–58.

(22) Smith, J. D.; Corbett, J. D. Four zirconium iodide cluster phases centered by boron, aluminum, or silicon. *J. Am. Chem. Soc.* **1986**, *108* (8), 1927–1934.

(23) Smith, J. D.; Corbett, J. D. Stabilization of clusters by interstitial atoms. Three carbon-centered zirconium iodide clusters, $Zr_6I_{12}C$, $Zr_6I_{14}C$, and $MZr_6I_{14}C$ (M = K, Rb, or Cs). *J. Am. Chem. Soc.* **1985**, *107* (20), 5704–5711.

(24) Ströbele, M.; Meyer, H.-J. The new binary tungsten iodide $W_{15}I_{47}$. *Z. anorg. allg. Chem.* **2010**, *636* (1), 62–66.

(25) Rietveld, H. M. The Rietveld method. *Phys. Scr.* **2014**, *89* (9), 098002.

(26) Glass, C. W.; Oganov, A. R.; Hansen, N. USPEX—Evolutionary crystal structure prediction. *Comput Phys Commun* **2006**, *175* (11-12), 713–720.

(27) Perdew, J. P.; Ruzsinszky, A.; Csonka, G. I.; Vydrov, O. A.; Scuseria, G. E.; Constantin, L. A.; Zhou, X.; Burke, K. Restoring the density-gradient expansion for exchange in solids and surfaces. *Phys. Rev. Lett.* **2008**, *100* (13), 136406.

(28) Shannon, R. D.; Prewitt, C. T. Revised values of effective ionic radii. *Acta Crystallogr. B Struct. Crystallogr. Cryst. Chem.* **1970**, *26* (7), 1046–1048.

(29) Mattausch, H.; Eger, R.; Simon, A. Das erste Gadoliniumcarbidfluorid: Gd_2CF_2. *Z. anorg. allg. Chem.* **1991**, *597* (1), 145–150.

(30) Cockcroft, J. K.; Kremer, R. K.; Mattausch, H.; Raju, N. P.; Simon, A. Structure and magnetic ordering of holmium carbide fluoride, Ho_2CF_2. *J. Alloys Compd.* **1992**, *183*, 241–251.

(31) Come, J.; Naguib, M.; Rozier, P.; Barsoum, M. W.; Gogotsi, Y.; Taberna, P. L.; Morcrette, M.; Simon, P. A Non-Aqueous Asymmetric Cell with a Ti_2C-Based Two-Dimensional Negative Electrode. *J. Electrochem. Soc.* **2012**, *159* (8), A1368–A1373.

(32) Spanu, L.; Sorella, S.; Galli, G. Nature and strength of interlayer binding in graphite. *Phys. Rev. Lett.* **2009**, *103* (19), 196401.

(33) Druffel, D. L.; Kuntz, K. L.; Woomer, A. H.; Alcorn, F. M.; Hu, J.; Donley, C. L.; Warren, S. C. Experimental demonstration of an electride as a 2D material. *J. Am. Chem. Soc.* **2016**, *138* (49), 16089–16094.

(34) Kuntz, K. L.; Wells, R. A.; Hu, J.; Yang, T.; Dong, B.; Guo, H.; Woomer, A. H.; Druffel, D. L.; Alabanza, A.; Tománek, D.; et al. Control of surface and edge oxidation on phosphorene. *ACS Appl. Mater. Interfaces* **2017**, *9* (10), 9126–9135.

(35) Poole, R. T.; Szajman, J.; Leckey, R. C. G.; Jenkin, J. G.; Liesegang, J. Electronic structure of the alkaline-earth fluorides studied by photoelectron spectroscopy. *Phys. Rev. B* **1975**, *12* (12), 5872–5877.

(36) Vasquez, R. P. XPS Core level spectra of some Y compounds. *J. Electron Spectros. Relat. Phenomena* **1990**, *50* (2), 167–170.

(37) Mongstad, T.; Thøgersen, A.; Subrahmanyam, A.; Karazhanov, S. The electronic state of thin films of yttrium, yttrium hydrides and yttrium oxide. *Solar Energy Materials and Solar Cells* **2014**, *128*, 270–274.

(38) Agarwal, M.; DeGuire, M. R.; Heuer, A. H. Synthesis of yttrium oxide thin films with and without the use of organic self-assembled monolayers. *Appl. Phys. Lett.* **1997**, *71* (7), 891–893.

(39) Ihara, H.; Kumashiro, Y.; Itoh, A. X-ray photoelectron spectrum and band structure of TiC. *Phys. Rev. B* **1975**, *12* (12), 5465–5471.

(40) Ihara, H.; Hirabayashi, M.; Nakagawa, H. Electronic band structures and x-ray photoelectron spectra of ZrC, HfC, and TaC. *Phys. Rev. B* **1976**, *14* (4), 1707–1714.

(41) Nyholm, R.; Berndtsson, A.; Martensson, N. Core level binding energies for the elements Hf to Bi (Z=72-83). *J. Phys. C: Solid State Phys.* **1980**, *13* (36), L1091–L1096.

(42) Vasquez, R. P. SrF_2 by XPS. *Surf. Sci. Spectra* **1992**, *1* (1), 24–30.

(43) Padalia, B. D.; Gimzewski, J. K.; Affrossman, S.; Lang, W. C.; Watson, L. M.; Fabian, D. J. The reactions of oxygen and water with the rare-earth metals terbium to lutetium studied by x-ray photoelectron spectroscopy. *Surf Sci* **1976**, *61* (2), 468–482.

(44) Vasquez, R. P.; Foote, M. C.; Hunt, B. D. Reaction of nonaqueous halogen solutions with $YBa_2Cu_3O_{7-x}$. *J. Appl. Phys.* **1989**, *66* (10), 4866–4877.

(45) Nyholm, R.; Martensson, N. Core level binding energies for the elements Zr-Te (Z=40-52). *J. Phys. C: Solid State Phys.* **1980**, *13* (11), L279–L284.

(46) Zhang, C. J.; Pinilla, S.; McEvoy, N.; Cullen, C. P.; Anasori, B.; Long, E.; Park, S.-H.; Seral-Ascaso, A.; Shmeliov, A.; Krishnan, D.; et al. Oxidation Stability of Colloidal Two-Dimensional Titanium Carbides (MXenes). *Chem. Mater.* **2017**, *29* (11), 4848–4856.

(47) Li, G.; Jiang, K.; Zaman, S.; Xuan, J.; Wang, Z.; Geng, F. Ti_3C_2 Sheets with an Adjustable Surface and Feature Sizes to Regulate the Chemical Stability. *Inorg. Chem.* **2019**, *58* (14), 9397–9403.

(48) Wang, X.; Garnero, C.; Rochard, G.; Magne, D.; Morisset, S.; Hurand, S.; Chartier, P.; Rousseau, J.; Cabioc'h, T.; Coutanceau, C.; et al. A new etching environment (FeF_3 /HCl) for the synthesis of two-dimensional titanium carbide MXenes: a route towards selective reactivity vs. water. *J. Mater. Chem. A* **2017**, *5* (41), 22012–22023.

(49) Chae, Y.; Kim, S. J.; Cho, S.-Y.; Choi, J.; Maleski, K.; Lee, B.-J.; Jung, H.-T.; Gogotsi, Y.; Lee, Y.; Ahn, C. W. An investigation into the factors governing the oxidation of two-dimensional Ti_3C_2 MXene. *Nanoscale* **2019**, *11* (17), 8387–8393.

(50) Lotfi, R.; Naguib, M.; Yilmaz, D. E.; Nanda, J.; van Duin, A. C. T. A comparative study on the oxidation of two-dimensional Ti_3C_2 MXene structures in different environments. *J. Mater. Chem. A* **2018**, *6* (26), 12733–12743.

(51) Huang, S.; Mochalin, V. N. Hydrolysis of 2D Transition-Metal Carbides (MXenes) in Colloidal Solutions. *Inorg. Chem.* **2019**, *58* (3), 1958–1966.

(52) Alhabeb, M.; Maleski, K.; Mathis, T. S.; Sarycheva, A.; Hatter, C. B.; Uzun, S.; Levitt, A.; Gogotsi, Y. Selective Etching of Silicon from Ti_3SiC_2 (MAX) To Obtain 2D Titanium Carbide (MXene). *Angew. Chem. Int. Ed. Engl.* **2018**, *57* (19), 5444–5448.

(53) Ghidiu, M.; Lukatskaya, M. R.; Zhao, M.-Q.; Gogotsi, Y.; Barsoum, M. W. Conductive two-dimensional titanium carbide "clay" with high volumetric capacitance. *Nature* **2014**, *516* (7529), 78–81.

(54) Zhang, W. L.; Deng, L.; Liu, J.; Liu, Y.; Yin, J.; Zeng, H.; Zheng, W.; Zhang, A. Unveiling the Critical Role of Surface Oxidation of Electroresponsive Behaviors in Two-Dimensional $Ti_3C_2T_x$ MXenes. *J. Phys. Chem. C* **2019**, *123* (9), 5479–5487.

(55) Khazaei, M.; Arai, M.; Sasaki, T.; Ranjbar, A.; Liang, Y.; Yunoki, S. OH-terminated two-dimensional transition metal carbides and nitrides as ultralow work function materials. *Phys. Rev. B* **2015**, *92* (7), 075411.

(56) Schultz, T.; Frey, N. C.; Hantanasirisakul, K.; Park, S.; May, S. J.; Shenoy, V. B.; Gogotsi, Y.; Koch, N. Surface termination dependent work function and electronic properties of $Ti_3C_2T_x$ MXene. *Chem. Mater.* **2019**.

CHAPTER 5: EXPERIMENTAL ELECTRON-ANION EXCHANGE: AN ION EXCHANGE MECHANISM FOR LOW-TEMPERATURE ELECTRIDE SYNTHESIS

5.1 Introduction

Electrides are ionic materials in which negative charge compensation is provided by electrons instead of anions, where the electride electrons are found in lattice sites separate from atomic nuclei.[1] The exotic nature of electrides can afford interesting properties, including metallic conductivity,[2–5] magnetism,[6–10] low workfunction,[11,12] and high reactivity,[13–16] useful for a variety of applications (e.g. catalysis,[17–21] batteries,[22,23] electron emitters[24]). Traditionally, electrides have been produced through high-temperature synthetic methods such as sintering,[5,25] arc-melting,[26] or vapor deposition.[27,28] However, the discovery of new electrides with limited stability is hampered by the lack of low-temperature synthetic techniques for electrides. The exploration of new electride compositions with useful properties will require alternate strategies for electride synthesis under milder conditions.

Recently, it was demonstrated that electrides might undergo exchange between electride electrons and anions of similar size, such as F^-, in materials systems like Y_2CF_2/Y_2C with low energetic barriers for fluoride diffusion (< 300 meV).[29] Druffel, et. al. hypothesized that F^- might be extracted or inserted into the electride Y_2C when given a suitable thermodynamic driving force, such as a chemical reducing/oxidizing agent or application of electrochemical potential. While the concept of electron-anion exchange has been used to synthesize electrides previously, as in $[Ca_{24}Al_{28}O_{64}]^{4+}(4e^-)$ from $[Ca_{24}Al_{28}O_{64}]^{4+}(4O^{2-})$ or M_2NX (M = Ca, Sr; X = F, Cl, Br) from M_2N (M = Ca, Sr),[3,30–32] the temperatures employed were rather high (> 750°C), likely due to

low mobility of anions within the electride materials. In systems such as Y_2CF_2/Y_2C, however, the diffusion barrier for F^- is small, possibly allowing for electron-anion exchange at much lower temperatures. Therefore, we explore the dehalogenation of Y_2CF_2 with chemical reducing agents to synthesize the electride Y_2C at low temperatures, introducing a new synthetic technique for electride synthesis.

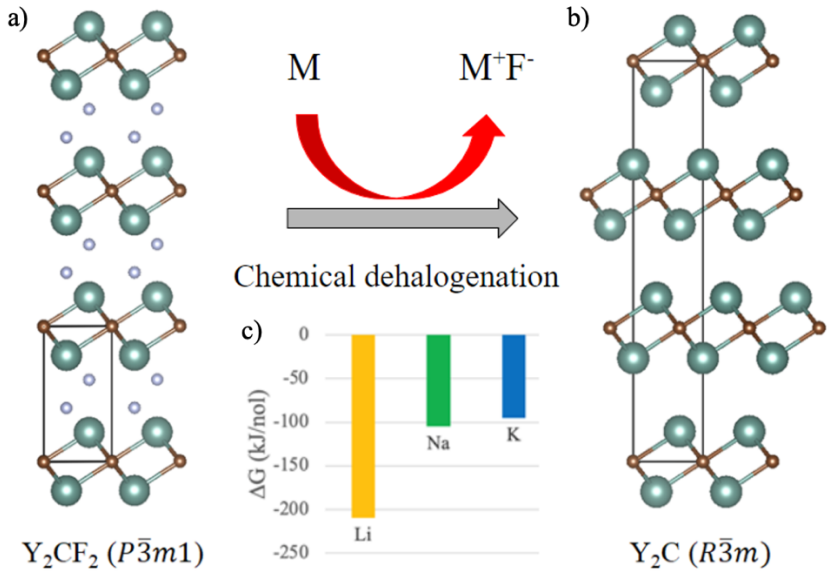


Figure 5.1: Electron-anion exchange via chemical defluorination with alkali metal reducing agents (Li, Na, K). Structures for a) Y_2CF_2 and b) Y_2C electride with c) thermodynamic driving forces (ΔG) for each reagent.

Previously, strong reducing agents such as Na metal vapor or NaH have been used for the chemical dehalogenation of layered materials at low temperatures (300 - 500°C), including ZrN from ZrNCl[33] and La_2NiO_3F from $La_2NiO_3F_2$.[34] In addition, lithium metal has been employed as a low-temperature (> 180°C) molten matrix for reactions such as the reduction of graphite to LiC_6,[35] which may be a good medium for halide extraction given the substantial formation energy associated with LiF from Li.[36] Herein, the alkali metals Li, Na, or K will be explored as chemical reducing agents for the defluorination of Y_2CF_2 to Y_2C (Figure 5.1a,b).

5.2 Thermodynamic predictions

First, the thermodynamic driving force (ΔG) for alkali fluoride formation from Y_2C + Li, Na, or K was calculated using density-functional theory according to the following reaction:

$$Y_2CF_2 + 2\,M \rightarrow Y_2C + 2\,MF \qquad \text{M = Li, Na, K}$$

The strongest thermodynamic driving force (Figure 5.1c) is provided by the formation of LiF, likely related to the small workfunction of Li (2.9 eV)[37] and similar ionic radii of Li^+ (90 pm) and F^- (119 pm).[38] The formation of NaF or KF is associated with a lower ΔG of -100 kJ/mol, suggesting that Na and K might be able to extract F^- from Y_2CF_2 but might require longer reaction times or higher temperatures. Therefore, lithium metal was first explored as a chemical defluorination agent for Y_2CF_2.

5.3 Reaction between Y_2CF_2 and molten Li

The starting material, Y_2CF_2, was synthesized by the solid-state reaction of YF_3 with Y metal and graphite at 1240°C over 3 days in a sealed Ta ampoule.[39] To provide a reference compound for the expected reaction products from Y_2CF_2 + Li, layered Y_2C was also synthesized.[26] Lithium granules were melted in a Ta boat produced from Ta foil at a setting of 300°C on a hot plate in an argon-filled glovebox (Figure 5.2a,b). The actual temperature of the molten lithium was estimated to be between 250-300°C. Tantalum foil was utilized due to its low reactivity and absence of stable alloys with lithium metal.[40] Y_2CF_2 powder was slowly incorporated into the molten Li by folding the powder into the globule with a stainless-steel spatula (Figure 5.2c). Initially, the powder did not mix well with the molten Li. However, after ~10 minutes of stirring, the surface tension quickly dropped, and a pool of silvery lithium with a solid floating on the surface was produced (Figure 5.2d). The liquid pool was blended for an additional 30 minutes to ensure thorough incorporation of the Y_2CF_2 powder, then left to cool.

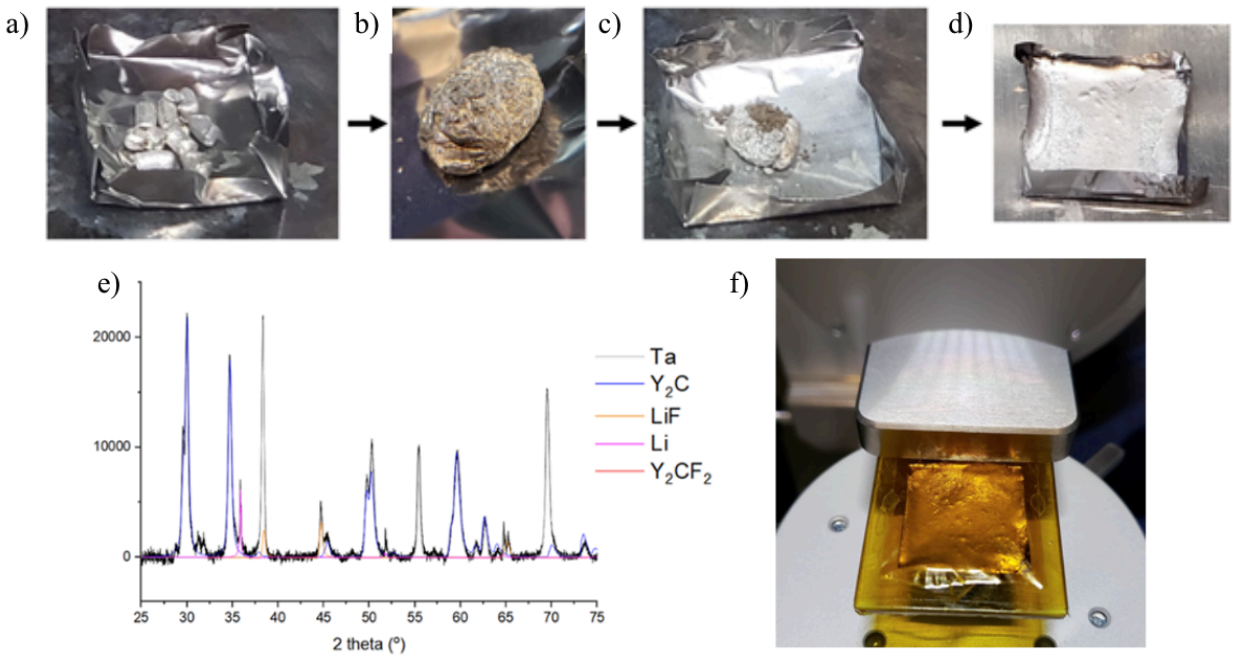


Figure 5.2: Reaction between Y_2CF_2 and molten lithium. Images of the a) lithium pellets in a folded tantalum boat, b) molten lithium at 300ºC hot-plate setting, c) adding Y_2CF_2 powder to molten lithium ball, and d) product of stirring Y_2CF_2 powder into molten lithium for ~30 minutes. e) X-ray diffraction pattern of the Y_2CF_2-Li products with refined patterns from tantalum (gray), Y_2C (blue), LiF (orange), and Li (pink). f) Image of the reaction products on an XRD slide under Kapton film for XRD measurement.

An X-ray diffractogram of the reaction products with molten Li is shown in Figure 5.2e. All peaks are accounted for by the phases Y_2C, LiF, Ta, and Li with no evidence of leftover Y_2CF_2, suggesting the reaction went to completion. While the signal from the tantalum substrate masks the peak from LiF at 38º, the expected peak at 45º is clearly observed. The reaction was repeated three more times, giving very similar results. In two of the reactions, a small amount of leftover Y_2CF_2 was observed in the X-ray diffractogram, likely a result of insufficient mixing in the Ta boat. To ensure proper mixing of the molten Li and Y_2CF_2, high-force ball-milling or mechanical stirring could be employed in future reactions. Observation of the layered Y_2C and

LiF phases by X-ray diffraction gives strong evidence for electron-anion exchange from Y_2CF_2 to layered Y_2C at temperatures < 300°C.

Hard X-ray absorption spectroscopy was performed at the Y K-edge to determine the electronic and structural similarity between Y_2C and the Y_2CF_2-Li product. Druffel, et. al. computationally determined the oxidation state of Y in Y_2C and Y_2CF_2 to be 1.9+,[29] different from the 3+ oxidation state typically observed in Y-containing compounds.[41,42] However, multiple other compounds have been studied where yttrium is in the 2+ oxidation state, including YCl, Y_2Cl_3, YBr, and Y_2Br_3.[43] In fact, $[YCl]^+e^-$ and $[Y_2Cl_3]^+e^-$ were recently found to be electrides.[44] The anomalous behavior of these materials is ascribed to d-level splitting of ligands in the crystal field, which is likely correlated to electride formation.[45] Even though neither of these electride materials were synthesized and used as a Y^{2+} reference, Y_2O_3 was experimentally analyzed to provide a Y^{3+} reference.

X-ray absorption spectra for Y_2C, Y_2CF_2, the Y_2CF_2-Li product, and Y_2O_3 are shown in Figure 5.3a. The X-ray absorption near-edge structure (XANES), or absorption edge, for Y_2C is shifted ~3 eV lower in energy than for Y_2O_3 (Figure 5.3b). The shift is indicative of a smaller oxidation state than 3+ for Y in Y_2C, however the oxidation state was not able to be verified as 1.9+. The absorption edge for Y_2CF_2 is very close to the edge for Y_2O_3, suggesting the average oxidation state of Y may be closer to 3+. Even though the Y_2C and Y_2CF_2 samples were packaged in a similar manner, decomposition of the Y_2CF_2 to YOF is still probable. An alternate explanation is that our computational predictions were incorrect, and yttrium is in a more oxidized state in Y_2CF_2 than in Y_2C.

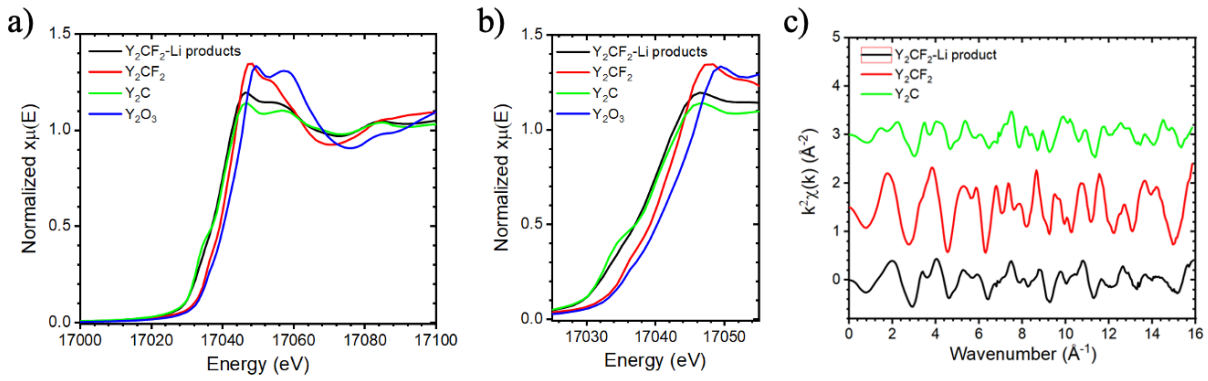


Figure 5.3: XAS on Y_2CF_2-Li products. a) X-ray absorption spectra for Y_2C (green), Y_2CF_2 (red), Y_2CF_2-Li products (black), and Y_2O_3 (blue). b) Zoomed in image of the XANES for each compound. c) Plots of the extended X-ray absorption fine structure (EXAFS) regions in k-space for Y_2C (green), Y_2CF_2 (red) and Y_2CF_2-Li (black).

The XANES spectrum for the Y_2CF_2-Li product closely resembles the absorption edge and for bulk Y_2C, corroborating the XRD results that show near 100% conversion of Y_2CF_2 to Y_2C. Aside from the pre-edge feature at 17034 eV in the bulk Y_2C sample, the spectrum for Y_2CF_2-Li overlaps precisely. Plotting the EXAFS signal in k-space (Figure 5.3c) maps the chemical environment of yttrium atoms in reciprocal space and provides additional structural information. The k-space EXAFS pattern for the Y_2CF_2-Li product does not resemble either Y_2C or Y_2CF_2, although general features of each phase are present. For example, the peak at 2 $Å^{-1}$ for Y_2CF_2-Li is similar to the peak for Y_2CF_2, but the doublet around 4 $Å^{-1}$ resembles the signal for Y_2C. A rough estimate of the composition from the EXAFS data is 85% Y_2C and 15% Y_2CF_2, suggesting the reaction may not have actually gone to completion. The leftover Y_2CF_2 could have low crystallinity, explaining the discrepancy between the EXAFS and XRD data. The majority of the Y_2CF_2-Li product is composed of Y_2C; the first experimental demonstration of electron-anion exchange at low temperatures.

5.4 Reaction between Y_2CF_2 and Na or K vapor

Although the thermodynamic driving force is smaller (-100 kJ/mol), Y_2CF_2 was exposed to K vapor to drive formation of Y_2C + KF. First, Y_2CF_2 powder was enclosed in a Ta packet inside a half-sealed quartz tube. Then, quartz wool was used to separate the Ta packet from a piece of K with a mass corresponding to 10x excess by mole. The quartz tube was sealed under 1 atm of Ar and heated to 300°C for 3 days, where the expected vapor pressure of K is approximately 0.4 mbar. After the reaction, the quartz tube appeared completely black, signifying that the K metal was sufficiently vaporized. The quartz tube was opened in the glovebox, and the powder inside the Ta packet analyzed by XRD (Figure 5.4).

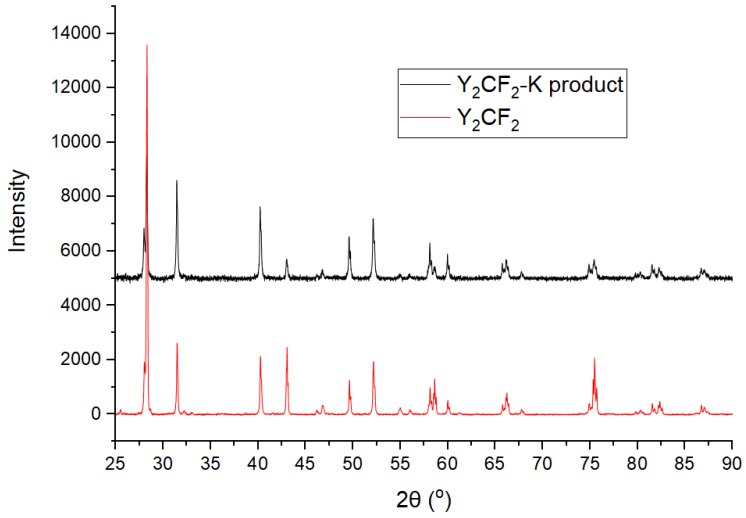


Figure 5.4: X-ray diffraction pattern of the products from the Y_2CF_2 + K vapor reaction (black) compared to the Y_2CF_2 starting material (red).

The products of the reaction are identical to the starting Y_2CF_2 powder, indicating no significant reaction between the K vapor and Y_2CF_2. The thermodynamic driving force for KF formation is weaker than LiF formation, which may explain the difference in outcome. There could also be large kinetic barriers to KF formation, requiring higher temperatures or longer reaction times. Since Na metal provides a similar thermodynamic force for defluorination and

has comparable vapor pressure to K, no further reactions with K or Na were employed. A future direction may be to employ molten Na, molten K, or liquid Na/K alloy to allow for enhanced alkali metal/Y_2CF_2 contact.

5.5 Conclusion

In this work, a new low-temperature method for electride synthesis was explored through defluorination of Y_2CF_2 to the electride Y_2C with alkali metal reducing agents. The most promising synthesis procedure involved using molten Li metal, where the synthesis of Y_2C was accomplished on a hot plate at ~300ºC with > 85% conversion. X-ray diffraction of the reaction products showed clear formation of the target Y_2C phase and strong peaks for LiF. X-ray absorption spectroscopy showed a close match between the absorption edge of the products with bulk Y_2C, although there were inconsistencies in the k-space EXAFS spectrum. The Y_2CF_2 + Li products may contain as much as 15% unreacted Y_2CF_2, or the structure of the Y_2C product is slightly different from bulk Y_2C. Future investigations will involve improving mixing during synthesis and verifying the 2+ oxidation state of Y in Y_2C and Y_2CF_2. Our new synthetic strategy based on low-temperature electron-anion exchange expands the synthetic toolkit for electrides and could allow for the synthesis of electrides that are unstable at high temperatures.

REFERENCES

(1) Dye, J. L. Electrides: ionic salts with electrons as the anions. *Science* **1990**, *247* (4943), 663–668.

(2) Dye, J. L. Electrides: From 1D Heisenberg Chains to 2D Pseudo-Metals. *Inorg. Chem.* **1997**, *36* (18), 3816–3826.

(3) Matsuishi, S.; Toda, Y.; Miyakawa, M.; Hayashi, K.; Kamiya, T.; Hirano, M.; Tanaka, I.; Hosono, H. High-density electron anions in a nanoporous single crystal: $[Ca_{24}Al_{28}O_{64}]^{4+}(4e^-)$. *Science* **2003**, *301* (5633), 626–629.

(4) Dale, S. G.; Johnson, E. R. The ionic versus metallic nature of 2D electrides: a density-functional description. *Phys. Chem. Chem. Phys.* **2017**, *19* (40), 27343–27352.

(5) Lee, K.; Kim, S. W.; Toda, Y.; Matsuishi, S.; Hosono, H. Dicalcium nitride as a two-dimensional electride with an anionic electron layer. *Nature* **2013**, *494* (7437), 336–340.

(6) Park, J.; Lee, K.; Lee, S. Y.; Nandadasa, C. N.; Kim, S.; Lee, K. H.; Lee, Y. H.; Hosono, H.; Kim, S.-G.; Kim, S. W. Strong Localization of Anionic Electrons at Interlayer for Electrical and Magnetic Anisotropy in Two-Dimensional Y_2C Electride. *J. Am. Chem. Soc.* **2017**, *139* (2), 615–618.

(7) Mudryk, Y.; Paudyal, D.; Pecharsky, V. K.; Gschneidner, K. A. Magnetic properties of Gd_2C: Experiment and first principles calculations. *J. Appl. Phys.* **2011**, *109* (7), 07A924.

(8) Lee, S. Y.; Hwang, J.-Y.; Park, J.; Nandadasa, C. N.; Kim, Y.; Bang, J.; Lee, K.; Lee, K. H.; Zhang, Y.; Ma, Y.; et al. Ferromagnetic quasi-atomic electrons in two-dimensional electride. *Nat. Commun.* **2020**, *11* (1), 1526.

(9) Badrtdinov, D.; Nikolaev, S. Localised magnetism in 2D electrides. *J. Mater. Chem. C* **2020**.

(10) Sui, X.; Wang, J.; Duan, W. Prediction of Stoner-Type Magnetism in Low-Dimensional Electrides. *J. Phys. Chem. C* **2019**, *123* (8), 5003–5009.

(11) Uijttewaal, M. A.; Wijs, G. A. de; Groot, R. A. de. Low work function of the (1000) Ca_2N surface. *J. Appl. Phys.* **2004**, *96* (3), 1751–1753.

(12) Toda, Y.; Yanagi, H.; Ikenaga, E.; Kim, J. J.; Kobata, M.; Ueda, S.; Kamiya, T.; Hirano, M.; Kobayashi, K.; Hosono, H. Work Function of a Room-Temperature, Stable Electride $[Ca_{24}Al_{28}O_{64}]^{4+}(e^-)_4$. *Adv. Mater. Weinheim* **2007**, *19* (21), 3564–3569.

(13) Wu, J.; Li, J.; Gong, Y.; Kitano, M.; Inoshita, T.; Hosono, H. Intermetallic electride catalyst as a platform for ammonia synthesis. *Angew. Chem. Int. Ed. Engl.* **2019**, *58* (3), 825–829.

(14) Toda, Y.; Hirayama, H.; Kuganathan, N.; Torrisi, A.; Sushko, P. V.; Hosono, H. Activation and splitting of carbon dioxide on the surface of an inorganic electride material. *Nat. Commun.* **2013**, *4*, 2378.

(15) Lu, Y.; Li, J.; Tada, T.; Toda, Y.; Ueda, S.; Yokoyama, T.; Kitano, M.; Hosono, H. Water durable electride Y_5Si_3: electronic structure and catalytic activity for ammonia synthesis. *J. Am. Chem. Soc.* **2016**, *138* (12), 3970–3973.

(16) Menamparambath, M. M.; Park, J.-H.; Yoo, H.-S.; Patole, S. P.; Yoo, J.-B.; Kim, S. W.; Baik, S. Large work function difference driven electron transfer from electrides to single-walled carbon nanotubes. *Nanoscale* **2014**, *6* (15), 8844–8851.

(17) Kitano, M.; Inoue, Y.; Yamazaki, Y.; Hayashi, F.; Kanbara, S.; Matsuishi, S.; Yokoyama, T.; Kim, S.-W.; Hara, M.; Hosono, H. Ammonia synthesis using a stable electride as an electron donor and reversible hydrogen. *Nature chemistry* **2012**, *4*, 934–940.

(18) Ye, T.-N.; Lu, Y.; Xiao, Z.; Li, J.; Nakao, T.; Abe, H.; Niwa, Y.; Kitano, M.; Tada, T.; Hosono, H. Palladium-bearing intermetallic electride as an efficient and stable catalyst for Suzuki cross-coupling reactions. *Nat. Commun.* **2019**, *10* (1), 5653.

(19) Yoo, B. I.; Kim, Y. J.; You, Y.; Yang, J. W.; Kim, S. W. Birch Reduction of Aromatic Compounds by Inorganic Electride $[Ca_2N]^+ \bullet e^-$ in an Alcoholic Solvent: An Analogue of Solvated Electrons. *J. Org. Chem.* **2018**, *83* (22), 13847–13853.

(20) Choi, S.; Kim, Y. J.; Kim, S. M.; Yang, J. W.; Kim, S. W.; Cho, E. J. Hydrotrifluoromethylation and iodotrifluoromethylation of alkenes and alkynes using an inorganic electride as a radical generator. *Nat. Commun.* **2014**, *5*, 4881.

(21) Kim, Y. J.; Kim, S. M.; Hosono, H.; Yang, J. W.; Kim, S. W. The scalable pinacol coupling reaction utilizing the inorganic electride $[Ca_2N]^+ \cdot e^-$ as an electron donor. *Chem. Commun.* **2014**, *50* (37), 4791–4794.

(22) Chen, G.; Bai, Y.; Li, H.; Li, Y.; Wang, Z.; Ni, Q.; Liu, L.; Wu, F.; Yao, Y.; Wu, C. Multilayered electride Ca_2N electrode via compression molding fabrication for sodium ion batteries. *ACS Appl. Mater. Interfaces* **2017**, *9* (8), 6666–6669.

(23) Hou, J.; Tu, K.; Chen, Z. Two-Dimensional Y_2C Electride: A Promising Anode Material for Na-Ion Batteries. *J. Phys. Chem. C* **2016**, *120* (33), 18473–18478.

(24) Kim, S. W.; Toda, Y.; Hayashi, K.; Hirano, M.; Hosono, H. Synthesis of a Room Temperature Stable $12CaO \cdot 7Al_2O_3$ Electride from the Melt and Its Application as an Electron Field Emitter. *Chem. Mater.* **2006**, *18* (7), 1938–1944.

(25) Chung, J. H.; Ryu, J. H.; Eun, J. W.; Choi, B. G.; Shim, K. B. One-Step Synthesis of a $12CaO \cdot 7Al_2O_3$ Electride via the Spark Plasma Sintering (SPS) Method. *Electrochem. Solid-State Lett.* **2011**, *14* (12), E41.

(26) Zhang, X.; Xiao, Z.; Lei, H.; Toda, Y.; Matsuishi, S.; Kamiya, T.; Ueda, S.; Hosono, H. Two-Dimensional Transition-Metal Electride Y_2C. *Chem. Mater.* **2014**, *26* (22), 6638–6643.

(27) Inumaru, K.; Kuroda, Y.; Sakamoto, K.; Murashima, M.; Yamanaka, S. Synthesis and high metallic conductivity of layer-structured Sr_2N thin film deposited onto MgO(001) substrate. *J. Alloys Compd.* **2004**, *372* (1-2), L1–L3.

(28) Weber, S.; Schäfer, S.; Saccoccio, M.; Seidel, K.; Kohlmann, H.; Gläser, R.; Schunk, S. A. Mayenite-based electride C12A7e$^-$: an innovative synthetic method *via* plasma arc melting. *Mater. Chem. Front.* **2021**.

(29) Druffel, D. L.; Pawlik, J. T.; Sundberg, J. D.; McRae, L. M.; Lanetti, M. G.; Warren, S. C. First-Principles Prediction of Electrochemical Electron-Anion Exchange: Ion Insertion without Redox. *J. Phys. Chem. Lett.* **2020**, 9210–9214.

(30) Bowman, A.; Smith, R. I.; Gregory, D. H. Ternary and quaternary layered nitride halides, $Ca_2N(X,X')$ (X,X′=Cl, Br, I): Evolution of structure with composition. *J. Solid State Chem.* **2005**, *178* (6), 1807–1817.

(31) Bowman, A.; Smith, R. I.; Gregory, D. H. Synthesis and structure of the ternary and quaternary strontium nitride halides, $Sr_2N(X, X')$ (X, X′=Cl, Br, I). *J. Solid State Chem.* **2006**, *179* (1), 130–139.

(32) Bowman, A.; Mason, P. V.; Gregory, D. H. Heteroanionic intercalation into positively charged inorganic hosts: the first nitride mixed halides. *Chem. Commun.* **2001**, No. 17, 1650–1651.

(33) Zhu, L.; Ohashi, M.; Yamanaka, S. Zirconium Nitride Derived from Layer-Structured β-ZrNCl by Deintercalation of Chlorine Layers. *Chem. Mater.* **2002**, *14* (11), 4517–4521.

(34) Wissel, K.; Malik, A. M.; Vasala, S.; Plana-Ruiz, S.; Kolb, U.; Slater, P. R.; da Silva, I.; Alff, L.; Rohrer, J.; Clemens, O. Topochemical Reduction of $La_2NiO_3F_2$: The First Ni-Based Ruddlesden–Popper $n = 1$ T′-Type Structure and the Impact of Reduction on Magnetic Ordering. *Chem. Mater.* **2020**, *32* (7), 3160–3179.

(35) Basu, S.; Zeller, C.; Flanders, P. J.; Fuerst, C. D.; Johnson, W. D.; Fischer, J. E. Synthesis and properties of lithium-graphite intercalation compounds. *Materials Science and Engineering* **1979**, *38* (3), 275–283.

(36) Kubaschewski, O.; Alcock, C.B.; Spencer, P. J. *Materials thermochemistry*, 6th ed.; Pergamon Press, 1993.

(37) Lang, N. D.; Kohn, W. Theory of Metal Surfaces: Work Function. *Phys. Rev. B* **1971**, *3* (4), 1215–1223.

(38) Ahrens, L. H. The use of ionization potentials Part 1. Ionic radii of the elements. *Geochim. Cosmochim. Acta* **1952**, *2* (3), 155–169.

(39) Druffel, D. L.; Lanetti, M. G.; Sundberg, J. D.; Pawlik, J. T.; Stark, M. S.; Donley, C. L.; McRae, L. M.; Scott, K. M.; Warren, S. C. Synthesis and Electronic Structure of a 3D Crystalline Stack of MXene-Like Sheets. *Chem. Mater.* **2019**, *31* (23), 9788–9796.

(40) Shabalin, I. L. Tantalum. In *Ultra-High Temperature Materials I*; Springer Netherlands: Dordrecht, 2014; pp 387–450.

(41) Jollet, F.; Noguera, C.; Thromat, N.; Gautier, M.; Duraud, J. P. Electronic structure of yttrium oxide. *Phys. Rev. B, Condens. Matter* **1990**, *42* (12), 7587–7595.

(42) Cloke, F. G. N. Zero oxidation state compounds of scandium, yttrium, and the lanthanides. *Chem. Soc. Rev.* **1993**, *22* (1), 17.

(43) Mattausch, H.; Hendricks, J. B.; Eger, R.; Corbett, J. D.; Simon, A. Reduced halides of yttrium with strong metal-metal bonding: yttrium monochloride, monobromide, sesquichloride, and sesquibromide. *Inorg. Chem.* **1980**, *19* (7), 2128–2132.

(44) Wan, B.; Lu, Y.; Xiao, Z.; Muraba, Y.; Kim, J.; Huang, D.; Wu, L.; Gou, H.; Zhang, J.; Gao, F.; et al. Identifying quasi-2D and 1D electrides in yttrium and scandium chlorides via geometrical identification. *npj Comput. Mater.* **2018**, *4* (1), 77.

(45) Mikheev, N. B.; Auerman, L. N.; Rumer, I. A.; Kamenskaya, A. N.; Kazakevich, M. Z. The anomalous stabilisation of the oxidation state 2+ of lanthanides and actinides. *Russ. Chem. Rev.* **1992**, *61* (10), 990–998.

CHAPTER 6: ELECTROCHEMICAL FLUORINATION OF ELECTRIDE Y_2C FOR ROOM-TEMPERATURE FLUORIDE-ION BATTERIES

6.1 Introduction

Among next-generation battery technologies such as Na-ion,[1] Mg-ion,[2] and Li-O_2,[3] fluoride-ion batteries are especially interesting due to their high theoretical voltages ($\leq$ 4 V) and electrode capacities (200 – 900 mAh/g).[4] The small size of fluoride ions and large formation energies of metal fluorides translate to dense ion packing and large electrochemical potentials for fluorination and defluorination. However, current fluoride-ion batteries exhibit significant capacity fading and require high temperatures to operate, arising from large volume changes in metal fluoride electrodes and low electrolyte conductivities.[5] For example, a recent configuration based on La | $La_{0.9}Ba_{0.1}F_{2.9}$ | CuF_2 displayed a promising first discharge capacity of 350 mAh/g at 2.9 V, but the capacity faded to 50 mAh/g over 24 cycles.[6] Therefore, new electrodes based on intercalation mechanisms with low volume changes and electrolytes with high ionic conductivities need to be developed.

While most fluoride-ion batteries have utilized solid-state electrolytes with low ionic conductivities,[7] liquid fluoride-ion electrolytes with higher ionic conductivities have recently been developed.[8–12] One liquid fluoride-ion electrolyte composed of 2.0 M neopentyltrimethylammonium fluoride (Np_1F) in bis(trifluoroethyl)ether (BTFE)[10] shows a room-temperature conductivity of 2.5 x 10^{-3} S/cm and a wide electrochemical stability window (~ 3 V), opening new possibilities for high voltage room-temperature fluoride-ion batteries. In addition, a new electrode material, Y_2C, was recently predicted to be a promising intercalation-

based anode for fluoride-ion batteries.[13] The Y_2C material (Figure 6.1a) and fluorinated material Y_2CF_2 (Figure 6.1b) have fluoride-ion diffusion barriers as low as 196 meV (Figure 6.1c), a small volume difference of 7%, and a maximum theoretical charge capacity of 262 mAh/g (Figure 6.1d). The largest charge capacity achieved previously for an intercalation-based fluoride-ion electrode was only 30 mAh/g, indicating that Y_2C electrodes could offer high energy density while maintaining high cyclability. Moreover, the Y_2CF_2/Y_2C couple has a predicted electrochemical potential of +0.97 V vs. Li/Li^+,[13] classifying the system as a good candidate anode material for fluoride-ion batteries (Figure 6.1e).

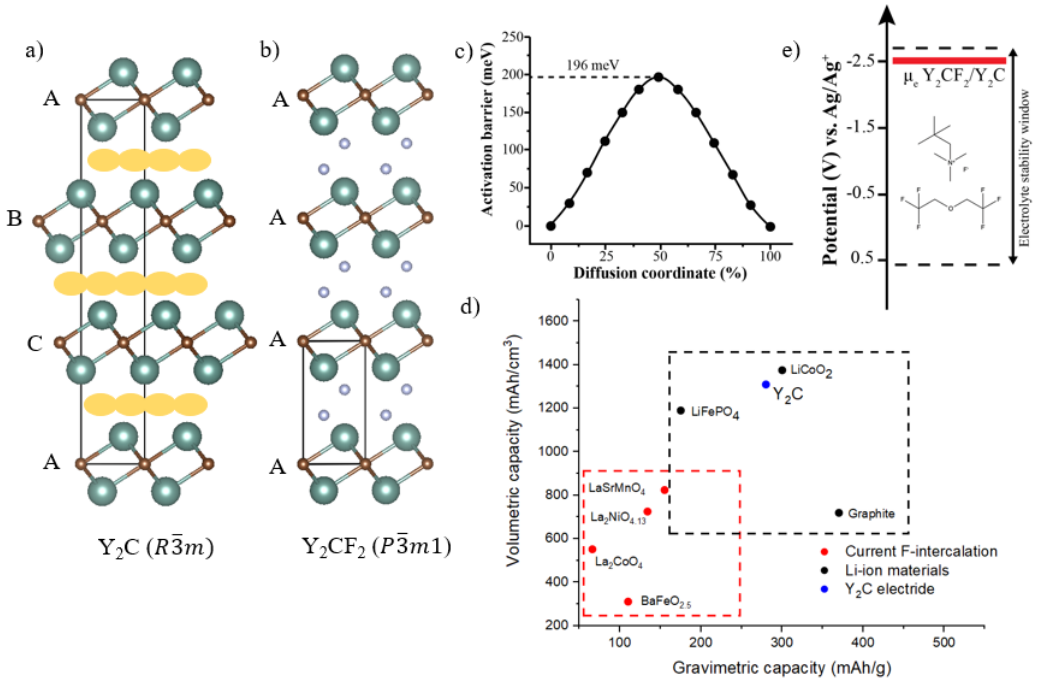


Figure 6.1: Y_2C/Y_2CF_2 as high energy density fluoride-ion electrodes. Crystal structures of a) electride $[Y_2C]^{2+}(2e^-)$ and b) the analogous structure, Y_2CF_2. c) Fluoride-ion diffusion barrier for Y_2C and Y_2CF_2. d) Comparison of the charge capacity of Y_2C to common fluoride-ion intercalation materials and Li-ion battery electrodes. e) Electrochemical potential of Y_2CF_2/Y_2C electron-anion exchange.

Y_2C belongs to a class of substances called electrides, which are ionic materials where electrons act as the charge balance instead of anions, and the electrons occupy distinct regions separate from atoms.[14] Therefore, electrides tend to have low workfunctions[15,16] and are good reducing agents,[17–19] suitable characteristics for anodes in batteries.[20–22] The structure of $[Y_2C]^{2+}(2e^-)$ with space group $R\bar{3}m$ is shown in Figure 6.1a, highlighting the electron density between the $[Y_2C]^{2+}$ atomic layers in yellow. The analogous fluorinated structure, Y_2CF_2, exhibits a stacking sequence change from ABC to AA, altering the space group to $P\bar{3}m1$ and expanding the lattice by 0.3 Å in the c-direction (Figure 6.1b). Interestingly, oxidation state analysis of yttrium atoms in Y_2C and Y_2CF_2 predicts that the Y remains in a 2+ oxidation state throughout F^- diffusion,[13] suggesting a non-redox mechanism for fluoride intercalation. We call this new mechanism "electron-anion exchange", whereby the insertion/deinsertion of anions into electrides is not accompanied by redox of the atomic lattice. The electron-anion exchange mechanism might afford fast halide-ion conducting materials suitable for high-capacity battery electrodes.

In this work, the electrochemical cycling behavior of Y_2C and Y_2CF_2 is evaluated in a room-temperature liquid fluoride-ion electrochemical cell based on the Np_1F/BTFE electrolyte. We predict that the small energetic barrier for fluoride-ion diffusion and high ionic conductivity of the electrolyte allows for experimental electron-anion exchange with high charge capacities at room temperature. A custom 3-electrode electrochemical cell is constructed to evaluate disk electrodes with incorporation of a reference electrode to isolate individual electrode behavior. The outcome of electrochemical cycling is analyzed by ex-situ X-ray diffraction (XRD) to determine structural changes and energy-dispersive X-ray spectroscopy (EDS) to confirm fluorine content throughout charging or discharging.

6.2 Results/Discussion

6.2.1 Fluoride-ion electrolyte characterization

First, the ionic conductivity of the Np_1F/BTFE electrolyte was evaluated using electrochemical impedance spectroscopy. High ionic conductivity in the electrolyte is essential for ensuring fast ions transport between electrodes during polarization. The frequency-dependent impedance (Z) of a 2-electrode cell (Pt | electrolyte | Ta) was determined by applying an oscillating potential of $\pm$10 mV and measuring the current output, where Z(t)=V(t)/I(t). The solution resistance and double layer capacitance of the electrode can be represented electrically by a resistor and capacitor in series, resulting in a vertical line in the Nyquist plot (Re(Z) vs. -Im(Z)). The x-intercept of the line corresponds to the solution resistance. The ionic conductivity (σ) of the electrolyte can then be determined by using the following equation, where d = electrode separation and A = electrode area:

$$\sigma = \frac{d}{R * A}$$

Nyquist plots from 100 kHz – 1 Hz for cells containing electrolytes 0.3 M and 0.6 M electrolytes are shown in Figure 6.2. The impedance appears as a slanted line instead of a vertical line, likely because the solution is behaving as a non-ideal capacitor, called a constant-phase element (CPE). The Nyquist plots were fit with equivalent circuits comprised of a resistor in series with a constant phase element, resulting in the fitting parameters reported in Table 6.1.

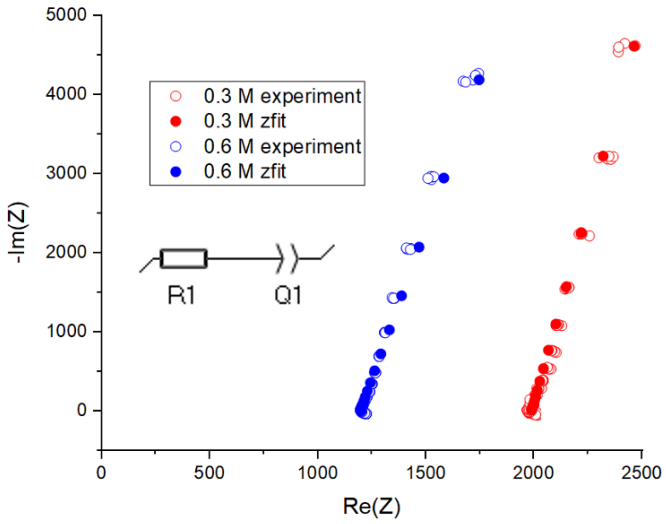


Figure 6.2: Electrochemical impedance spectroscopy on the F-electrolyte. Nyquist plots of the Re(Z) (Ω) and -Im(Z) (Ω) parts of the impedance for 0.3 M (red) and 0.6 M (blue) electrolyte solutions as a function of frequency from 100 kHz to 1 Hz. The lines were fit using an equivalent circuit of a resistor in series with a constant phase element.

Table 6.1: Equivalent circuit fitting of EIS data. Fitting parameters for the equivalent circuit in Figure 6.1 for 0.3 M and 0.6 M electrolytes.

Sample	Fitting parameter	Value	Ionic conductivity
0.3 M electrolyte	R1	1980 Ω	1.2 x 10^{-4} S/cm
	Q1	6.4 x 10^{-6} F·s$^{(A1-1)}$	
	A1	0.935	
0.6 M electrolyte	R1	1197 Ω	2.1 x 10^{-4} S/cm
	Q1	7.5 x 10^{-6} F·s$^{(A1-1)}$	
	A1	0.917	

With an electrode area (A) of 11.335 cm^2 and electrode separation (d) of 2.858 cm, the ionic conductivities of the 0.3 M and 0.6 M electrolytes were calculated to be 1.2 x 10^{-4} S/cm and 2.1 x 10^{-4} S/cm, respectively. The conductivity of the 0.6 M electrolyte was roughly double that of the 0.3 M electrolyte, consistent with the linear relationship between ion concentration

and ionic conductivity. However, the magnitude of the conductivity is lower than reported previously (2 x 10^{-3} S/cm for 0.7 M), and would generally be considered outside the range for an ideal electrolyte (> 1 x 10^{-3} S/cm).[7] Therefore, fluoride-ion transport may be limited to the electrode during electrochemical testing and could introduce added resistance to electrochemical fluorination/defluorination.

The stability of the Ag/Ag^+ reference electrode in the F-electrolyte was analyzed by constructing a Pt | electrolyte | Ta and monitoring the open circuit potential between the working and reference electrodes. The voltage approached a stable range after 2.5 hours with OCV oscillations < 300 mV, correlating to wetting of the reference frit. After sitting overnight, the OCV approached a steady value of around -1 V with a fluctuation < 50 mV. The steady voltage indicates that the electrochemical potential of the reference electrode is stable in the F-electrolyte.

The electrochemical stability window of the F-electrolyte was investigated by performing cyclic voltammetry on the Pt | electrolyte | Ta cell from -3 V to 1 V vs. Ag/Ag^+ at a scan speed of 100 mV/s (Figure 6.3). The magnitude of the current increased past 0.5 V on the anodic sweep and past -2.5 V on the cathodic sweep, similar to the electrochemical window observed by Davis, et. al.[10] The cyclic voltammetry results suggest that the Ag/Ag^+ reference electrode used is both stable in the F-electrolyte and has an accurate electrochemical potential compared to previous reports.

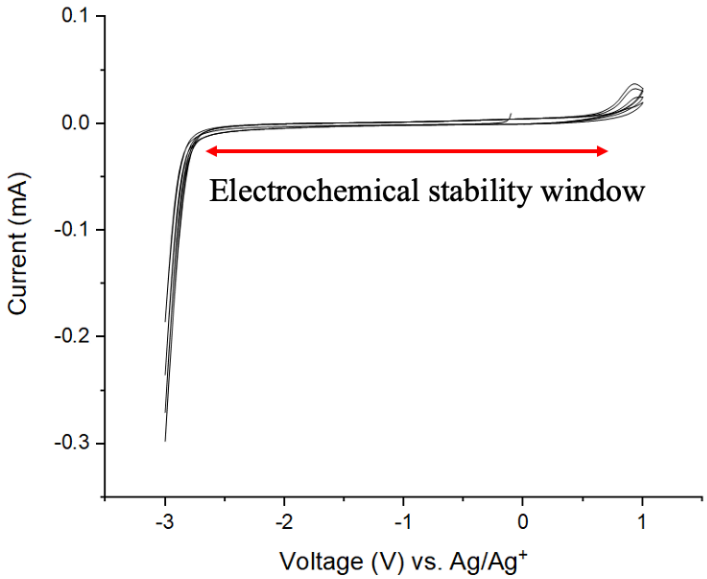


Figure 6.3: Determination of the F-electrolyte electrochemical window. Cyclic voltammetry on a Pt | electrolyte | Ta cell from -3 V to 1 V vs. Ag/Ag^+ at a sweep rate of 100 mV/s.

6.2.2 Electrode preparation and characterization

The Y_2C and Y_2CF_2 active materials were analyzed by X-ray diffraction to ensure successful synthesis of both phases (Figure 6.4). Comparison of each pattern to known crystal structures for Y_2C and Y_2CF_2 show an excellent match to the predicted diffractograms, where both materials appear to be moderately crystalline. A minor impurity phase of YOF was observed in the Y_2CF_2 pattern, likely sourced from the oxygen content in the starting yttrium powder. Rietveld refinements of each phase show good fitting ($R_{wp} < 10\%$) and similar lattice parameters to known phases (< 0.07% difference).

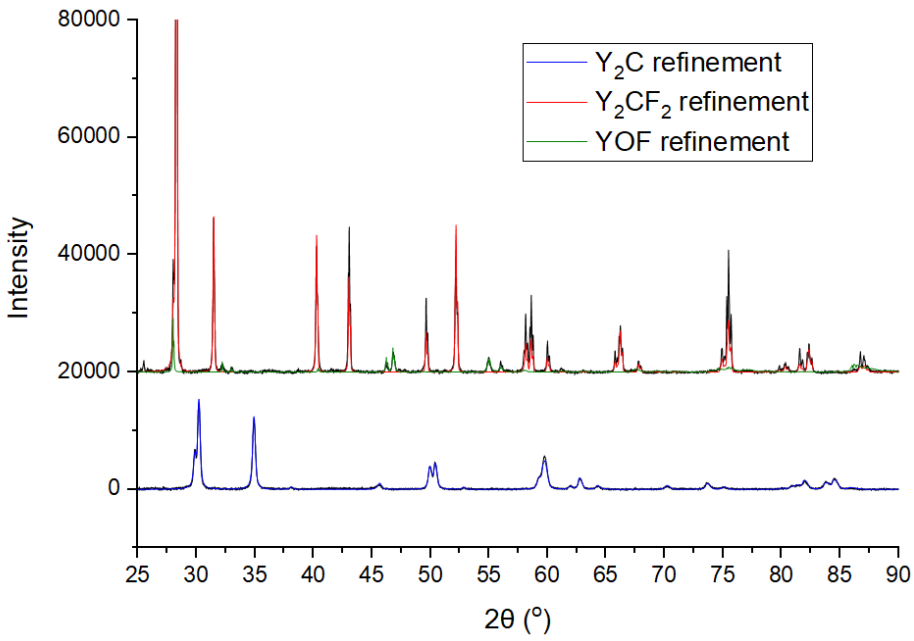


Figure 6.4: XRD of bulk Y_2C and Y_2CF_2. X-ray diffraction patterns with Rietveld refinements for bulk Y_2C (blue), Y_2CF_2 (red), and YOF (gray), showing differences in peak shifts and alignment with predicted peak positions. Y_2C refinement: R_{wp} = 7.23%; S = 7.556; a,b = 3.6189 Å, c = 17.968 Å. Y_2CF_2 refinement: R_{wp} = 4.05%; S = 5.906; a,b = 3.669 Å, c = 6.294 Å. Composition: 2.2% YOF, 97.8% Y_2CF_2 by mole.

Slurries of Y_2C and Y_2CF_2 were produced with solid contents of 80% active material, 10% PVDF binder, and 10% Super P suspended in propylene carbonate with a solid/liquid mass ratio of 40%. Similar compositions have been used for lithium-ion electrodes, showing optimal electronic conductivity and mechanical robustness.[23] The Y_2C or Y_2CF_2 powder was ball-milled for 15 minutes before use, reducing the particle to size to < 50 µm, as measured by SEM. A reduction in the particle size is important for ensuring fast transport of F^- in and out of the active material.[24] Each slurry appeared black from the dense carbon content (Figure 6.5a) and had an ink-like consistency. The slurries were spread evenly onto tantalum foil and doctor bladed using a glass pipet until uniform (Figure 6.5b,c). For each layer of 4 Mil Scotch tape, the expected film

thickness before drying was ≤ 100 μm. When films were placed under vacuum at 120°C overnight, the solvent evaporated, and film uniformity was retained (Figure 6.5d). Each film was then cut into 19 mm disks using a precision disk cutter and used directly in the electrochemical cell (Figure 6.5e).

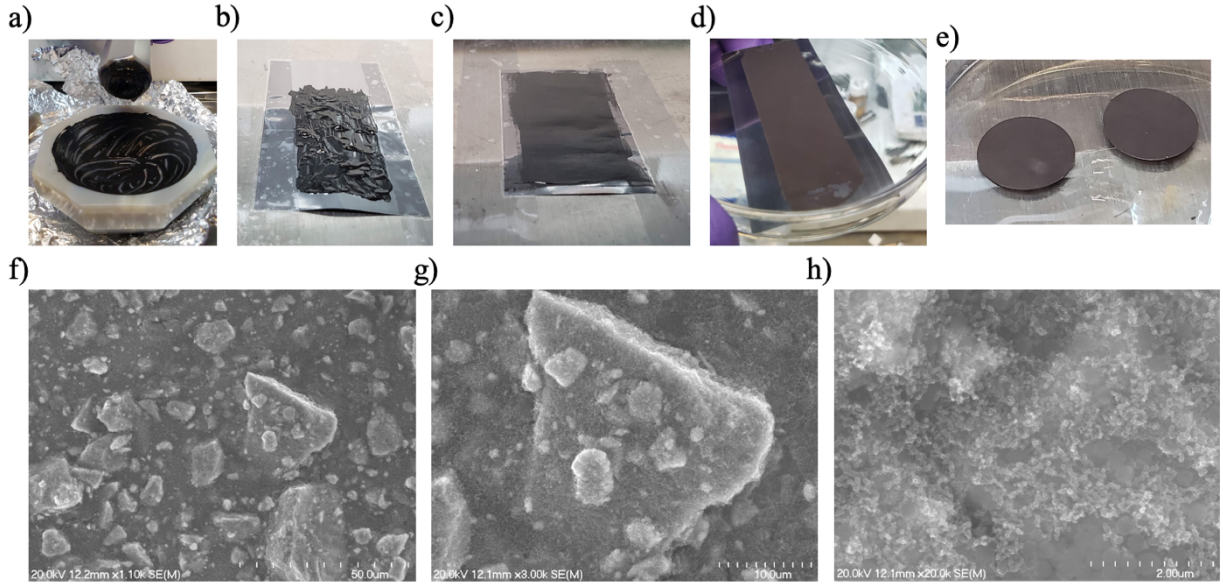


Figure 6.5: Preparation of electrode films for electrochemical testing. a) Slurry mixture with 80/10/10 wt% of active material/PVDF/Super P respectively in 40 wt% propylene carbonate. b) Slurry painted onto tantalum foil with 4 Mil Scotch tape lining. c) After doctor-blading with a glass pipet. d) Film dried at 120°C under vacuum overnight. e) Final disk electrodes after cutting with 19 mm precision disk cutter. SEM images of films at magnifications of f) 1100X, g) 3000X, h) 20,000X to observe particle size and PVDF/Super P coverage

The coverage of Super P and PVDF on active material particles was then analyzed by SEM (Figure 6.5f,g,h). A continuous matrix of binder and the conductive material is essential for ensuring fast electron transport throughout active material particles.[25] Also, a well-established matrix allows for mechanical robustness and resistance to electrode cracking.[26] The SEM image shown in Figure 6.5f is representative of most regions in the Y_2C and Y_2CF_2 film samples. The

particle sizes were generally < 50 μm, and a thick matrix of PVDF (white material) and Super P (spherical particles) were observed on the surface of active material particles (Figure 6.5g,h). Visually, these characteristics indicate that the electrode films were produced with good carbon coverage and particle sizes of active material.

X-ray diffraction patterns of Y_2C and Y_2CF_2 electrode films were captured to verify retention of the Y_2C and Y_2CF_2 structures after film processing (Figure 6.6a,b). The tantalum substrate displayed intense peaks in the diffraction patterns while the peaks from Y_2C and Y_2CF_2 are much weaker due to small electrode masses (~ 4 mg). A Rietveld refinement of each pattern using the known crystal structures of Y_2C and Y_2CF_2 shows a close match between the experimental pattern and predicted peaks. However, there was a small peak in the Y_2CF_2 film pattern at 35° that has yet to be identified, and is not associated with Ta, PVDF, or Super P. Interestingly, the XRD pattern for Y_2C contains a sharp peak at 35°, suggesting that fluorine defects may be formed during the Y_2CF_2 electrode fabrication. Regardless, the majority of the sample retains the Y_2CF_2 crystal structure.

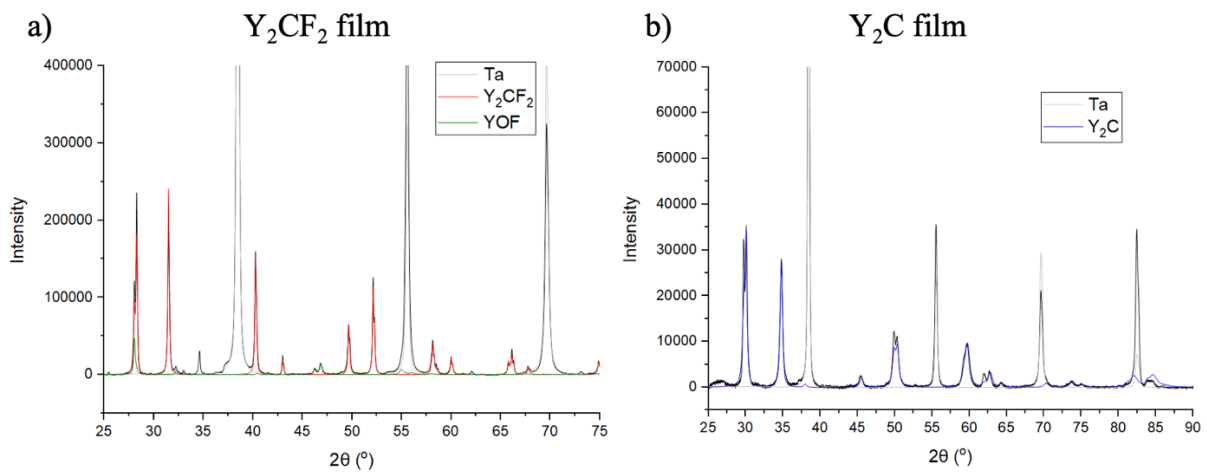


Figure 6.6: XRD of Y_2CF_2 and Y_2C films. X-ray diffraction patterns with Rietveld refinements for the a) Y_2CF_2 film and b) Y_2C film. Refined patterns for Ta, Y_2CF_2, Y_2C, and YOF are shown in gray, red, blue, and green respectively. Y_2CF_2 refinement: R_{wp} = 24.23%; S = 31.934; a,b = 3.671 Å, c = 6.295 Å. Y_2C refinement: R_{wp} = 6.60%; S = 10.467; a,b = 3.618 Å, c = 17.95 Å.

The composition of each film was analyzed by energy-dispersive X-ray spectroscopy (EDS) to confirm the stoichiometry of the Y_2C and Y_2CF_2 phases. EDS was performed in a transmission electron microscope (TEM) to isolate the composition of individual active material particles. The films were sonicated in diethyl carbonate to suspend the active material and decouple the PVDF from the particles. The PVDF needed to be separated since the polymer contains significant amounts of fluorine that could convolute the results. Aliquots of 3 µL from ~1 mg/mL suspensions of the films were dropped onto TEM grids and quickly loaded into the instrument. Diethyl carbonate was chosen as the solvent due to its low boiling point and similar properties to propylene carbonate, which was used to produce the slurry.

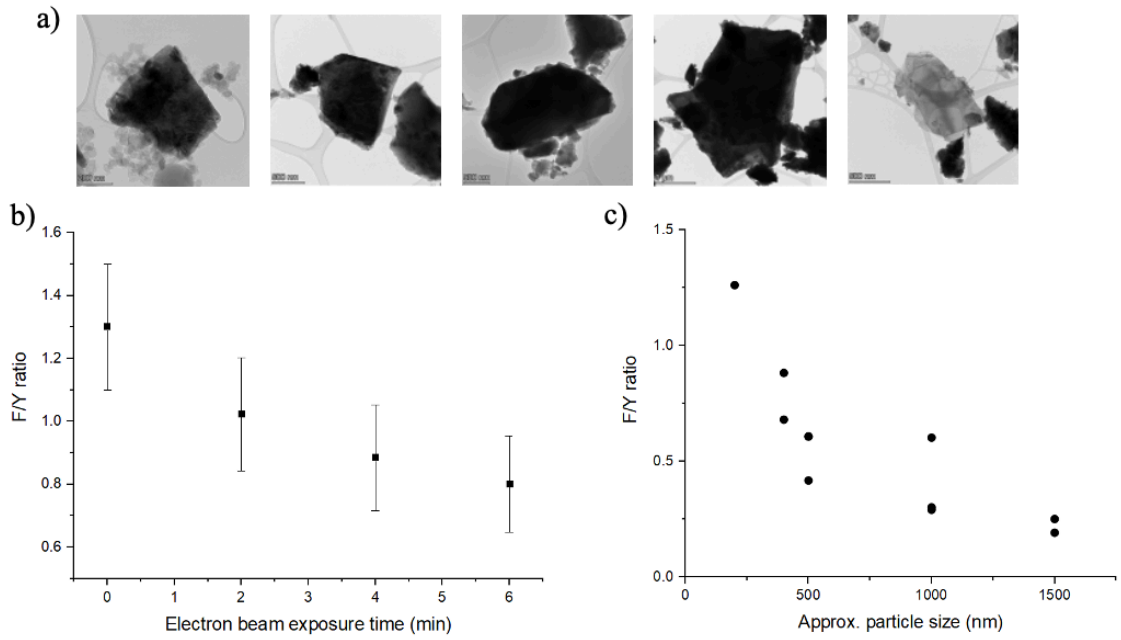


Figure 6.7: TEM-EDS of a Y_2CF_2 film. a) TEM images of Y_2CF_2 particles, b) Effect of electron beam exposure time on F/Y ratio among 13 particles, c) Composition of Y_2CF_2 particles in relation to approximate particle width.

As expected, there was no fluorine signal detected from the active material particles in the Y_2C film. The lack of fluorine signal also confirms that the PVDF binder was well separated from the Y_2C particles. The F/Y ratios for particles in the Y_2CF_2 film sample varied widely and were dependent on the amount of time the particles were exposed to the electron beam (Figure 6.7b,c). If the particles were immediately analyzed, the average F/Y ratio was close to 1.3, slightly larger than the expected 1:1 ratio. After 6 minutes of electron beam exposure, the F/Y ratio decreased to an average of 0.9. The reduction in F/Y ratio with beam exposure time may suggest radiation damage to Y_2CF_2 by the high-energy electron beam, knocking F^- out of the material. Radiolysis, or ionization damage, is a common occurrence in semiconductors and correlates to the bond strength between atoms in the material.[27]

Another interesting observation is that the F/Y ratio varied significantly with particle size. Particles larger than 1000 μm exhibited F/Y ratios < 0.5, much lower than expected for Y_2CF_2. Given that the structure of the Y-C-F material is close to Y_2CF_2 by XRD, compositions with less fluorine than Y_2CF are unlikely since there is a significant structural change in Y_2CF_x ($x < 1.0$). Characterization of lighter elements ($Z < 11$) by EDS often requires an absorption correction since low energy X-rays are easily absorbed by the sample and detector.[28] If unaccounted for, the composition can vary with thickness due to differences in penetration depth. Since the thickness of particles was not able to be determined, the F composition may be inaccurate for thick particles. The F/Y ratio of small particles averaged 1.1, similar to the expected 1:1 ratio for Y_2CF_2. Therefore, the composition of particles was evaluated through both the F/Y distribution and F/Y ratio of small particles to capture effects of X-ray absorption.

6.2.3 Soaking films in the F-electrolyte

Before performing electrochemistry, the films were soaked in the F-electrolyte to determine whether the electrodes change in structure or composition. Y_2C and Y_2CF_2 electrodes were left to sit in 1 mL of F-electrolyte overnight, then the electrolyte was decanted off and washed away with acetonitrile. After decanting the acetonitrile, either the sample was left to dry under vacuum for XRD analysis or was suspended in 1 mL of diethyl carbonate for TEM-EDS analysis.

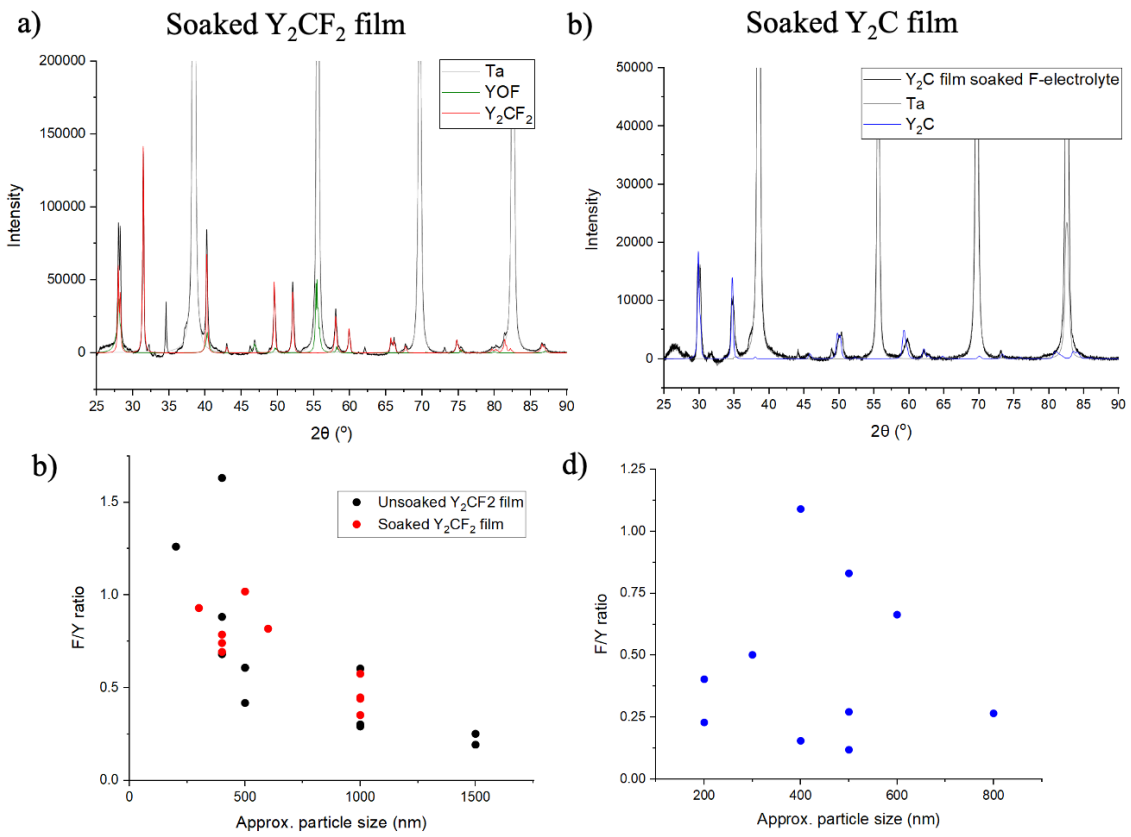


Figure 6.8: Effect of film soaking in F-electrolyte on structure and composition. XRD patterns and F/Y ratios from EDS for a,b) Y_2CF_2 and c,d) Y_2C films after soaking. Y_2CF_2 refinement: R_{wp} = 1.81%; S = 5.9978; a,b = 3.674 Å, c = 6.294 Å. Refinement of the Y_2C pattern was not able to be completed accurately.

The XRD pattern for the soaked Y_2CF_2 film is very similar to the film before soaking (Figure 6.8a). By EDS, the average F-content of the Y_2CF_2 particles decreased slightly to F/Y = 0.7 $\pm$ 0.2, however the fluorine distribution among particles appeared very similar (Figure 6.8b). The soaking process is not changing the fluorine content of the Y_2CF_2 particles significantly.

Soaking the Y_2C film in F-electrolyte results in the emergence of two small peaks in the XRD pattern at 28° and 32°, which may correspond to peaks for Y_2CF_2 (Figure 6.8b). The peaks for Y_2CF_2 at higher angles were not observed, although they may be too low in intensity to

detect. There was also an increase in F-content by EDS to 0.5 $\pm$ 0.3 with a random distribution of fluorine content among different sized particles (Figure 6.8d). The large increase in F-content by EDS may suggest the surface formation of Y_2CF_2 or the appearance of a F-rich solid-electrolyte interphase (SEI). By XRD, the amount of Y_2CF_2 formed appears to be low in concentration, corresponding to < 10% fluorine. Since the F/Y ratio was ~0.5 by EDS, the majority of fluorine content is probably coming from amorphous fluorine species on the surface.

6.2.4 Theoretical voltage profile

Cluster expansion calculations of the Y-C-F phase space were used to obtain a theoretical voltage profile for Y_2C fluorination. Analysis of the Y_2CF_{2-x} ($0 < x < 2$) phase space (Figure 6.9a) shows multiple thermodynamically stable phases with O3 stacking from $0 < x < 0.25$. Thereafter, compositions from $0.25 < x < 2$ are predicted to be mixtures of $Y_2CF_{0.25}$ and Y_2CF_2. The corresponding voltage profile (Figure 6.9b) shows an initial electrochemical potential of -2.875 V vs. Ag/Ag^+ for Y_2C, increasing by 0.25 V to -2.625 V for $Y_2CF_{0.25}$, then remaining flat until Y_2CF_2. These predictions show that the voltage is expected to remain fairly consistent during electrochemical charging or discharging, assuming that cell impedances are low and fluoride-ion transport is fast.

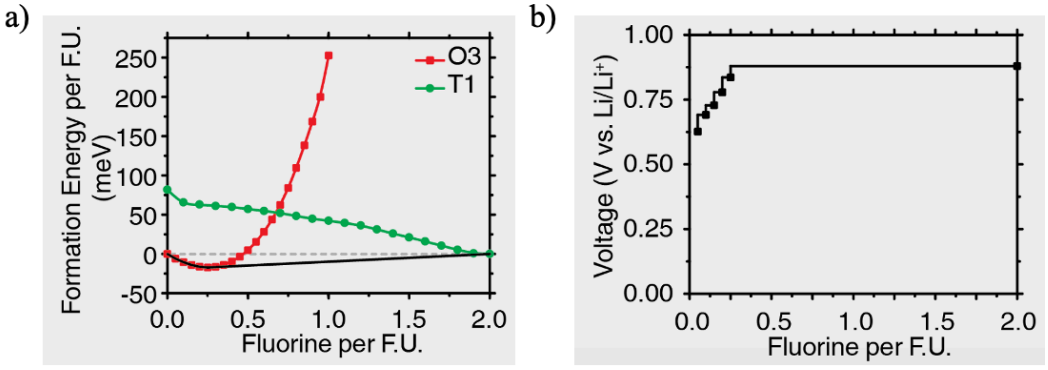


Figure 6.9: Expected voltage profile for Y_2C/Y_2CF_2 fluorination/defluorination. a) Cluster expansion analysis results of the Y-C-F phase space, showing the formation energy of structures from Y_2CF_{2-x} ($0 < x < 2$). Y-C-F structures with an O3 stacking are shown in red while those with T1 stacking are shown in green. b) Theoretical voltage profile for Y_2C fluorination derived from cluster expansion analysis. Voltage vs/ Li/Li^+ can be converted to Ag/Ag^+ by subtracting 3.5 V.

6.2.5 Electrochemistry on Y_2CF_2 films

A Y_2CF_2 film was loaded into the electrochemical cell and left soaking overnight with the reference electrode in place. The open circuit potential of the cell was tracked throughout the soaking and approached values between -2.5 V and -2.6 V, similar to the expected electrochemical potential for Y_2CF_2 (-2.625 V vs. Ag/Ag^+). Next, a negative current of -150 µA was applied to the Y_2CF_2 film working electrode. With a predicted charge capacity for Y_2CF_2 of 282 mAh/g, a mass loading of ~4 mg active material, and a current of -150 µA, the calculated C-rate was ~ 0.1 C, signifying the theoretical charging time should be 6 hours. The voltage quickly dropped to -4 V vs/ Ag/Ag^+ (Figure 6.10a), a value 1 V below the edge of the observed electrochemical stability window in Figure 6.3 and far from the expected discharge potential of -2.5 V. The voltage of electrochemical processes can shift when there are large resistances in the cell, giving rise to an overpotential according to Ohm's law V = IR. Two common sources of

resistance are the electrolyte and electrode films. With an electrolyte conductivity of 1 x 10^{-4} S/cm, the ohmic drop between the working and reference electrode should only be ~150 mV. Therefore, the electrode may introduce significant impedance into the electrochemical cell.

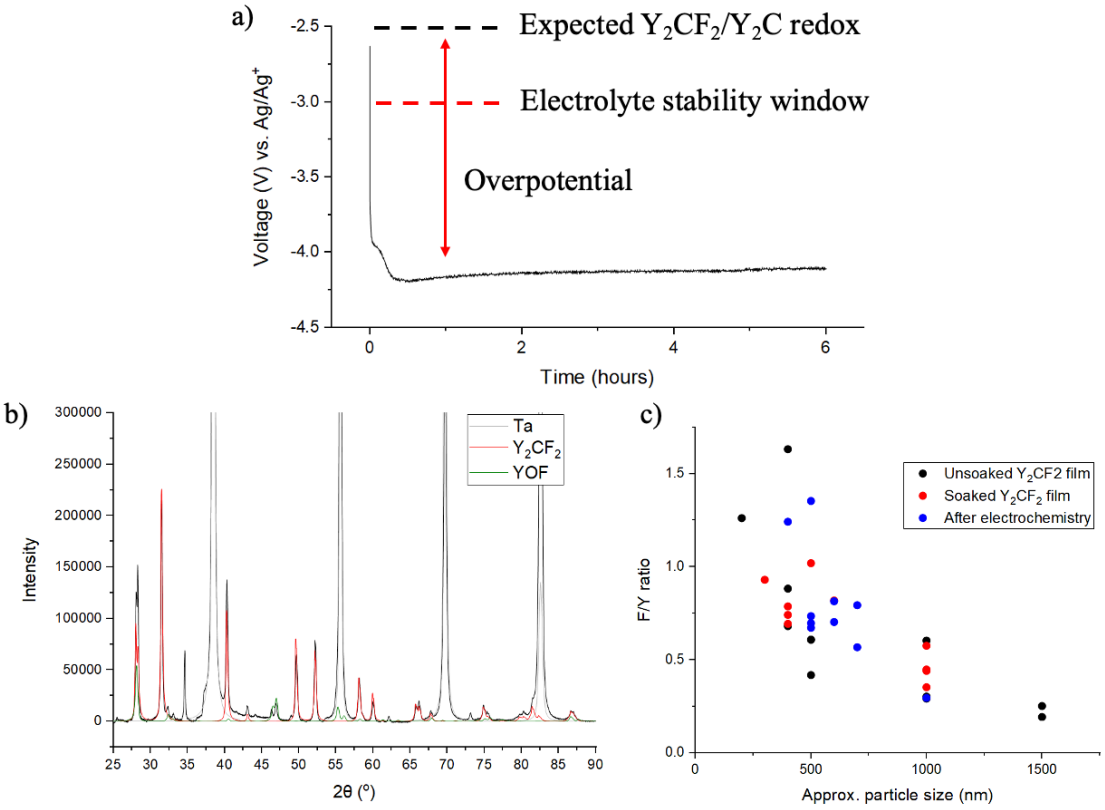


Figure 6.10: Electrochemistry on a Y_2CF_2 film. a) Chronopotentiometry on Y_2CF_2 film, -150 µA for 6 hours. b) XRD pattern of the Y_2CF_2 film after application of current. Y_2CF_2 refinement: R_{wp} = 10.13%; S = 44.65; a,b = 3.672 Å, c = 6.292 Å. c) Distribution of F/Y ratio in active material particles by EDS

An XRD pattern of the Y_2CF_2 film after chronopotentiometry and washing with ~1 mL of BTFE is shown in Figure 6.10b. No significant changes in crystal structure are observed, indicating that no crystalline Y_2C was produced. A compositional analysis by EDS (Figure 6.10c) confirmed that the average F/Y content did not change (0.8 $\pm$ 0.3) when compared to the soaked Y_2CF_2 film (0.7 $\pm$ 0.2), and the particle distribution of fluorine content remains

consistent. The overpotential for the reaction appears to be too large to conduct significant defluorination of Y_2CF_2.

6.2.6 Electrochemistry on Y_2C films

Next, a Y_2C film was placed in the electrochemical cell and left to soak overnight. The open circuit potential approached -2.5 V vs. Ag/Ag^+, slightly higher than the expected potential (-2.875 V). When a current of +150 μA was applied to the Y_2C film, the voltage began to linearly increase from -2.0 V to -0.4 V, then approached a plateau (Figure 6.11a). The shape of the voltage curve is very similar to the theoretical profile (Figure 6.9b), though it is shifted to much higher potentials. Moreover, the plateau extends past the theoretical capacity for the electrode (0.9 mAh), suggesting the flat region may actually correspond to electrolyte decomposition. There appears to be significant overpotential for Y_2C fluorination, similar to the Y_2CF_2 experiments. The film composition and thickness will need to be optimized to improve cell resistance. Remarkably, X-ray diffraction of the products after electrochemistry shows the emergence of peaks that match well with the Y_2CF_2 phase (Figure 6.11b). By Rietveld refinement, the molar ratio of Y_2CF_2 to Y_2C was approximately 2.3, meaning ~70% of the crystalline film contained Y_2CF_2. Excitingly, the application of current drives the electrochemical fluorination of Y_2C to Y_2CF_2.

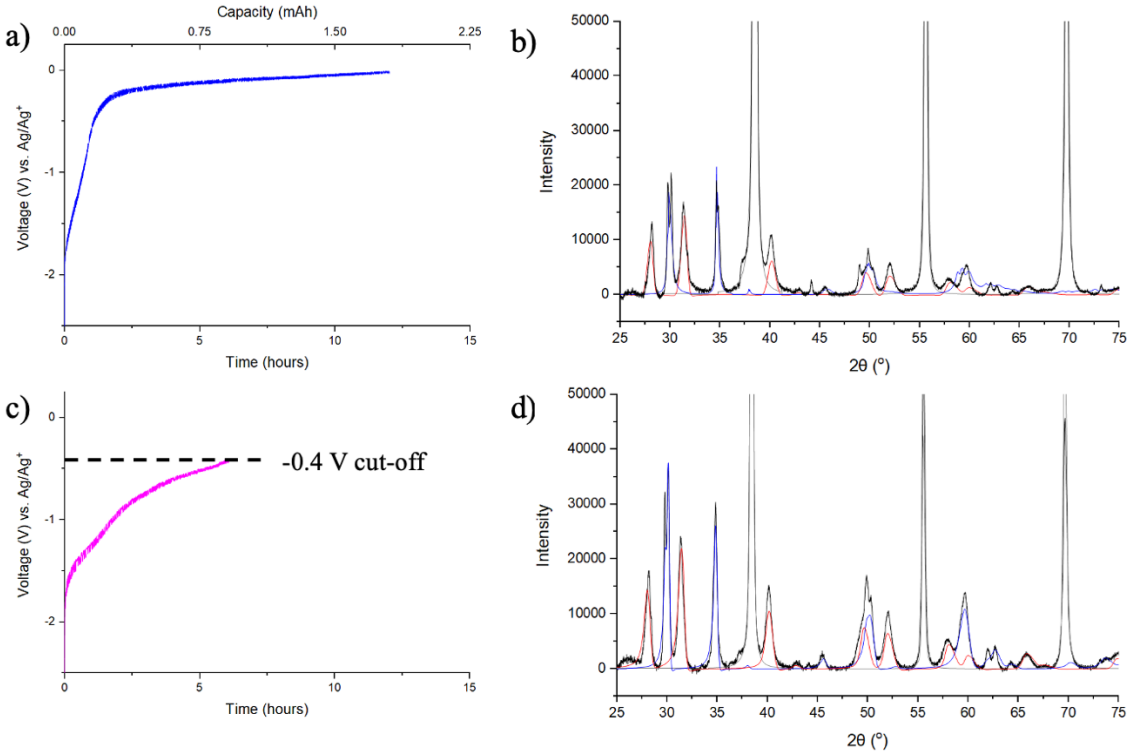


Figure 6.11: Electrochemistry on a Y_2C film. a) Chronopotentiometry on Y_2C film, 150 µA for 18 hours. b) XRD pattern of the Y_2C film after application of current. Y_2C refinement: R_{wp} = 9.49%; S = 20.6604; a,b = 3.651 Å, c = 17.86 Å; Y_2CF_2 refinement: a,b = 3.671 Å, c = 6.30 Å; Composition: 17% Y_2C, 83% Y_2CF_2 c) 150 µA on Y_2C film, -0.4 V cut-off. d) XRD pattern of Y_2C film after electrochemistry with -0.4 V cut-off. Y_2C refinement: R_{wp} = 5.21%; S = 13.0577; a,b = 3.62 Å, c = 17.81 Å; Y_2CF_2 refinement: a,b = 3.654 Å, c = 6.36 Å; Composition: 55% Y_2C, 45% Y_2CF_2.

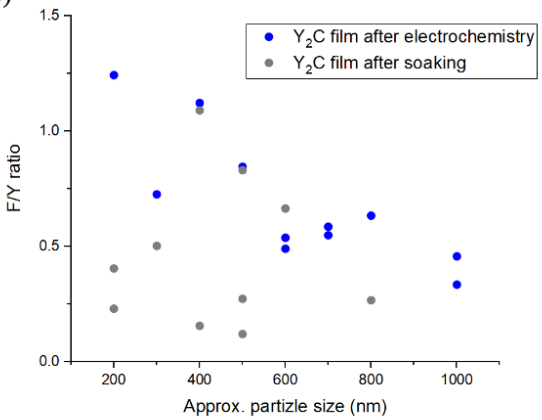
A second Y_2C film was subjected to +150 µA with a cut-off voltage of -0.4 V to see whether the initial region of the voltage profile correlates to Y_2C fluorination (Figure 6.11c). The slope of the profile was much smaller than before (~0.5 V/hr), suggesting variability in the quality of Y_2C films produced. An XRD pattern of the products (Figure 6.11d) shows similar results to the first experiment, where the proportion of Y_2CF_2 produced was also ~60-70%. The majority of Y_2C conversion to Y_2CF_2 occurs in the sloping region of the voltage profile while the

flat region correlates to electrolyte decomposition. Therefore, the gravimetric capacity of the Y_2C electrode may be as high as 225 mAh/g if the entire first region is due to Y_2C fluorination, a significant improvement to current intercalation-based electrodes.[29,30] Interestingly, the anodic stability limit (-0.5 V) is lower than the window observed in Figure 6.3 (0.5 V), suggesting the surface of the Y_2C may act to catalyze the decomposition of electrolyte and constrict the electrochemical stability window.

a)

	F/Y ratio
Initial Y_2C film	No fluorine
After soaking	0.5 ± 0.3
After 150 μA, 14 hrs	0.7 ± 0.3

b)



c)

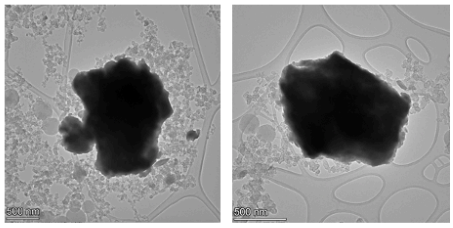


Figure 6.12: Elemental analysis of a Y_2C film after electrochemistry. a) Table summarizing EDS data on Y_2C films b) Distribution of particle sizes with different F/Y ratios. c) Images of Y_2C film particles after electrochemistry

Analysis by TEM-EDS shows a slight increase in fluorine content in the film after electrochemistry was performed (Figure 6.12a). The F/Y ratio increased from 0.5 ± 0.3 in the soaked film to 0.7 ± 0.3 in the film after current was applied. The fluorine content by EDS directly correlates to the proportion of Y_2CF_2 in the sample deduced by XRD, where 70% of Y_2CF_2 in the sample would give rise to a F/Y ratio of 0.7. The particle size distribution in Figure 6.12b shows a similar relationship between particle width and the F/Y ratio as the Y_2CF_2 samples, but with a smaller average F/Y content. The average F/Y ratio of small particles is ~

1.0, larger than expected for 70% fluorination of Y_2C. Therefore, the fluorine content is likely a combination of the fluorine from the SEI layer developed during soaking and from the formation of Y_2CF_2. Though not quantitative, the TEM-EDS results show that additional fluorine is being introduced into Y_2C particles through application of current.

6.2.7 Electrochemical cycling of Y_2C films

Lastly, a Y_2C electrode was subjected to electrochemical cycling to see if fluoride could be reversibly inserted and removed. A Y_2C film was subjected to +150 μA with a cut-off voltage of -0.4 V, then the current was switched to -150 μA to drive defluorination. The voltage profile (Figure 6.13a) shows similar behavior to previous experiments during electrochemical charging, then the potential quickly decreases to -3.8 V during discharging. The plateau under negative current has a potential +0.4 V higher than the cathodic stability limit observed in the Y_2CF_2 defluorination experiment but is still 1 V more negative than the -2.875 V expected for Y_2CF_x defluorination. There is still significant overpotential associated with Y_2CF_x defluorination. X-ray diffraction of the film after washing (Figure 6.13b) shows the composition to be 16% Y_2C and 84% Y_2CF_2 by mole, a larger degree of fluorination than observed in the Y_2C charging experiments. Therefore, application of negative current to partially fluorinated Y_2CF_x after electrochemical charging does not result in significant defluorination to Y_2C. The overpotential for fluoride deintercalation is too large, hindering reversible cycling of the Y_2C electrode.

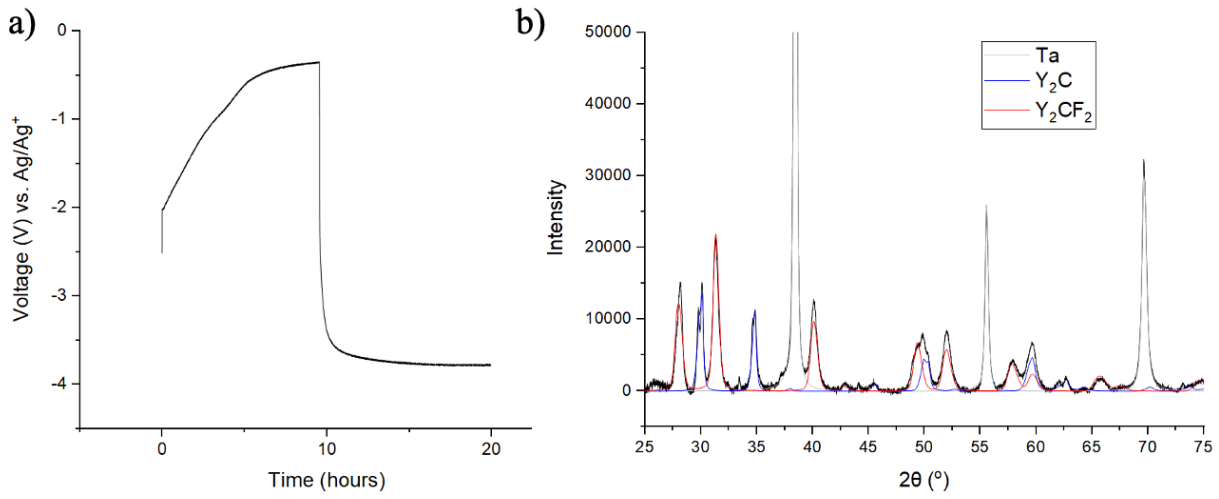


Figure 6.13: Electrochemical cycling of a Y_2C film. a) Voltage profile from application of +150 µA to -0.4 V cut-off, then -150 µA to -4 V cut-off. b) X-ray diffraction pattern of Y_2C film after fluorination then attempted defluorination. Y_2C refinement: R_{wp} = 1.33%; S = 2.9406; a,b = 3.61 Å, c = 17.96 Å; Y_2CF_2 refinement: a,b = 3.673 Å, c = 6.32 Å; 16% Y_2C, 84% Y_2CF_2.

6.3 Conclusions

Excitingly, results from electrochemical charging of the Y_2C films show that high charge capacities (70-200 mAh/g, 30-70% conversion) can be achieved through the exchange of electride electrons for fluoride in Y_2C. X-ray diffraction of the film after electrochemical charging showed new peaks for Y_2CF_2, and TEM-EDS showed an overall increase in the fluorine content. However, large overpotentials were observed in the charging and discharging curves, hindering the defluorination of Y_2CF_2 or partially fluorinated Y_2CF_x. The presence of overpotential is a major roadblock for harnessing the full charge capacity of Y_2C and performing reversible cycling experiments on the battery electrode. Mitigation of significant cell resistance may be accomplished by improving the electrical conductivity of Y_2C or Y_2CF_2 films and optimizing the cell geometry to accommodate smaller volumes of electrolyte.

Furthermore, significant surface decomposition occurs while soaking Y_2C in the F-electrolyte, suggesting the need for an artificial SEI to stabilize the interface. Davis, et. al. employed a LaF_3 artificial SEI on the surface of active material particles to act as a chemically robust layer between the electrode and electrolyte,[10] and a similar strategy might be used to engineer the Y_2C surface. A detailed understanding of the interface between the electride and F-electrolyte will be important for controlling efficient electron-anion exchange in Y_2C. Overall, electrides such as Y_2C offer new high-capacity electrodes for fluoride-ion batteries with low volume changes, potentially offering high energy density batteries with long cycle lifetime.

REFERENCES

(1) Slater, M. D.; Kim, D.; Lee, E.; Johnson, C. S. Sodium-Ion Batteries. *Adv. Funct. Mater.* **2013**, *23* (8), 947–958.

(2) Massé, R. C.; Uchaker, E.; Cao, G. Beyond Li-ion: electrode materials for sodium- and magnesium-ion batteries. *Sci. China Mater.* **2015**, *58* (9), 715–766.

(3) Zhou, H. New energy storage devices for post lithium-ion batteries. *Energy Environ. Sci.* **2013**, *6* (8), 2256.

(4) Anji Reddy, M.; Fichtner, M. Batteries based on fluoride shuttle. *J. Mater. Chem.* **2011**, *21* (43), 17059.

(5) Nowroozi, M. A.; Mohammad, I.; Molaiyan, P.; Wissel, K.; Munnangi, A. R.; Clemens, O. Fluoride ion batteries – past, present, and future. *J. Mater. Chem. A* **2021**.

(6) Thieu, D. T.; Fawey, M. H.; Bhatia, H.; Diemant, T.; Chakravadhanula, V. S. K.; Behm, R. J.; Kübel, C.; Fichtner, M. CuF_2 as reversible cathode for fluoride ion batteries. *Adv. Funct. Mater.* **2017**, *27* (31), 1701051.

(7) Patro, L. N.; Hariharan, K. Fast fluoride ion conducting materials in solid state ionics: An overview. *Solid State Ionics* **2013**, *239*, 41–49.

(8) Gschwind, F.; Zao-Karger, Z.; Fichtner, M. A fluoride-doped PEG matrix as an electrolyte for anion transportation in a room-temperature fluoride ion battery. *J. Mater. Chem. A* **2014**, *2* (5), 1214–1218.

(9) Okazaki, K.; Uchimoto, Y.; Abe, T.; Ogumi, Z. Charge–discharge behavior of bismuth in a liquid electrolyte for rechargeable batteries based on a fluoride shuttle. *ACS Energy Lett.* **2017**, *2* (6), 1460–1464.

(10) Davis, V. K.; Bates, C. M.; Omichi, K.; Savoie, B. M.; Momčilović, N.; Xu, Q.; Wolf, W. J.; Webb, M. A.; Billings, K. J.; Chou, N. H.; et al. Room-temperature cycling of metal fluoride electrodes: Liquid electrolytes for high-energy fluoride ion cells. *Science* **2018**, *362* (6419), 1144–1148.

(11) Davis, V. K.; Munoz, S.; Kim, J.; Bates, C. M.; Momčilović, N.; Billings, K. J.; Miller, T. F.; Grubbs, R. H.; Jones, S. C. Fluoride-ion solvation in non-aqueous electrolyte solutions. *Mater. Chem. Front.* **2019**, *3* (12), 2721–2727.

(12) Konishi, H.; Minato, T.; Abe, T.; Ogumi, Z. Electrochemical Performance of a Bismuth Fluoride Electrode in a Reserve-Type Fluoride Shuttle Battery. *J. Electrochem. Soc.* **2017**, *164* (14), A3702–A3708.

(13) Druffel, D. L.; Pawlik, J. T.; Sundberg, J. D.; McRae, L. M.; Lanetti, M. G.; Warren, S. C. First-Principles Prediction of Electrochemical Electron-Anion Exchange: Ion Insertion without Redox. *J. Phys. Chem. Lett.* **2020**, 9210–9214.

(14) Dye, J. L. Electrides: ionic salts with electrons as the anions. *Science* **1990**, *247* (4943), 663–668.

(15) Uijttewaal, M. A.; Wijs, G. A. de; Groot, R. A. de. Low work function of the (1000) Ca_2N surface. *J. Appl. Phys.* **2004**, *96* (3), 1751–1753.

(16) Toda, Y.; Yanagi, H.; Ikenaga, E.; Kim, J. J.; Kobata, M.; Ueda, S.; Kamiya, T.; Hirano, M.; Kobayashi, K.; Hosono, H. Work Function of a Room-Temperature, Stable Electride $[Ca_{24}Al_{28}O_{64}]^{4+}(e^-)_4$. *Adv. Mater. Weinheim* **2007**, *19* (21), 3564–3569.

(17) Menamparambath, M. M.; Park, J.-H.; Yoo, H.-S.; Patole, S. P.; Yoo, J.-B.; Kim, S. W.; Baik, S. Large work function difference driven electron transfer from electrides to single-walled carbon nanotubes. *Nanoscale* **2014**, *6* (15), 8844–8851.

(18) Kim, S.; Song, S.; Park, J.; Yu, H. S.; Cho, S.; Kim, D.; Baik, J.; Choe, D.-H.; Chang, K. J.; Lee, Y. H.; et al. Long-Range Lattice Engineering of $MoTe_2$ by a 2D Electride. *Nano Lett.* **2017**, *17* (6), 3363–3368.

(19) Toda, Y.; Hirayama, H.; Kuganathan, N.; Torrisi, A.; Sushko, P. V.; Hosono, H. Activation and splitting of carbon dioxide on the surface of an inorganic electride material. *Nat. Commun.* **2013**, *4*, 2378.

(20) Chen, G.; Bai, Y.; Li, H.; Li, Y.; Wang, Z.; Ni, Q.; Liu, L.; Wu, F.; Yao, Y.; Wu, C. Multilayered electride Ca_2N electrode via compression molding fabrication for sodium ion batteries. *ACS Appl. Mater. Interfaces* **2017**, *9* (8), 6666–6669.

(21) Hu, J.; Xu, B.; Yang, S. A.; Guan, S.; Ouyang, C.; Yao, Y. 2D Electrides as Promising Anode Materials for Na-Ion Batteries from First-Principles Study. *ACS Appl. Mater. Interfaces* **2015**, *7* (43), 24016–24022.

(22) Hou, J.; Tu, K.; Chen, Z. Two-Dimensional Y_2C Electride: A Promising Anode Material for Na-Ion Batteries. *J. Phys. Chem. C* **2016**, *120* (33), 18473–18478.

(23) Kraytsberg, A.; Ein-Eli, Y. Conveying Advanced Li-ion Battery Materials into Practice The Impact of Electrode Slurry Preparation Skills. *Adv. Energy Mater.* **2016**, *6* (21), 1600655.

(24) Lee, G.-W.; Ryu, J. H.; Han, W.; Ahn, K. H.; Oh, S. M. Effect of slurry preparation process on electrochemical performances of $LiCoO_2$ composite electrode. *J. Power Sources* **2010**, *195* (18), 6049–6054.

(25) Burdette-Trofimov, M. K.; Armstrong, B. L.; Nelson Weker, J.; Rogers, A. M.; Yang, G.; Self, E. C.; Armstrong, R. R.; Nanda, J.; Veith, G. M. Direct measure of electrode spatial heterogeneity: influence of processing conditions on anode architecture and performance. *ACS Appl. Mater. Interfaces* **2020**, *12* (50), 55954–55970.

(26) Kumberg, J.; Müller, M.; Diehm, R.; Spiegel, S.; Wachsmann, C.; Bauer, W.; Scharfer, P.; Schabel, W. Drying of lithium-ion battery anodes for use in high-energy cells: influence of electrode thickness on drying time, adhesion, and crack formation. *Energy Technology* **2019**, *7* (11), 1900722.

(27) Egerton, R. F. Radiation damage to organic and inorganic specimens in the TEM. *Micron* **2019**, *119*, 72–87.

(28) Burdet, P.; Saghi, Z.; Filippin, A. N.; Borrás, A.; Midgley, P. A. A novel 3D absorption correction method for quantitative EDX-STEM tomography. *Ultramicroscopy* **2016**, *160*, 118–129.

(29) Nowroozi, M. A.; Wissel, K.; Donzelli, M.; Hosseinpourkahvaz, N.; Plana-Ruiz, S.; Kolb, U.; Schoch, R.; Bauer, M.; Malik, A. M.; Rohrer, J.; et al. High cycle life all-solid-state fluoride ion battery with La2NiO4+d high voltage cathode. *Commun. Mater.* **2020**, *1* (1), 27.

(30) Nowroozi, M. A.; Ivlev, S.; Rohrer, J.; Clemens, O. La_2CoO_4 : a new intercalation based cathode material for fluoride ion batteries with improved cycling stability. *J. Mater. Chem. A* **2018**.